Solid state transformations during pharmaceutical processes

Dissertation with the aim of achieving a doctoral degree at the Faculty of Mathematics, Informatics and Natural Sciences Department of Chemistry of Universität Hamburg submitted by Andreas Beyer 2018 in Hamburg

Reviewer of the thesis

Prof. Claudia Leopold

Universität Hamburg

Prof. Hans-Ulrich Moritz

Universität Hamburg

Disputation date

17.05.2019

The experimental work of the dissertation was carried out between October 2012 until December 2015 at the Department of Chemistry, division of Pharmaceutical Technology, University of Hamburg, on the initiative and supervision of Professor Dr. Claudia S. Leopold.

I.

List of Publications

Beyer, A.; Grohganz, H.; Löbmann, K.; Rades, T; Leopold, C. S. Multivariate Quantification of the Solid State Phase Composition of Co-Amorphous Naproxen-Indomethacin, Molecules 10 (2015) 19571–19587.

Beyer, A.; Radi, L.; Grohganz, H.; Löbmann, K.; Rades, T; Leopold, C. S. Preparation and recrystallization behavior of spray-dried co-amorphous naproxen–indomethacin, European Journal of Pharmaceutics and Biopharmaceutics (2016) 72–81.

Beyer, A.; Grohganz, H.; Löbmann, K.; Rades, T; Leopold, C. S. Influence of the cooling rate and the blend ratio on the physical stability of co-amorphous naproxen/indomethacin, European Journal of Pharmaceutics and Biopharmaceutics (2016) 140–148.

Beyer, A.; Grohganz, H.; Löbmann, K.; Rades, T.Leopold, C. S. Improvement of the physicochemical properties of Co-amorphous naproxen-indomethacin by naproxen-sodium, International Journal of Pharmaceutics 1 (2017) 88–94.

Contents

III.

Abbreviation List

API	Active pharmaceutical ingredient
BCS	Biopharmaceutics Classification System
C_{IND}	Concentration of indomethacin
cNAP	Crystalline naproxen
C_{NAP}	Concentration of naproxen
cNS	Crystalline naproxen-sodium
cp	Heat capacity
DSC	Differential scanning calorimetry
Fam	Total amorphous fraction
F_{am}	Fraction of the amorphous phase
F_{amIND}	Fraction of amorphous indomethacin
F_{amNAP}	Fraction of amorphous naproxen
FC	Fast cooling
F_{cNAP}	Fraction of crystalline naproxen
FTIR	Fourier transformed infrared spectroscopy
$F_{\gamma\text{-}IND}$	Fraction of crystalline γ-indomethacin
I	Indomethacin
I_{Bragg}	Intensities resulting from the crystalline phase (Bragg peaks)
IC	Intermediate cooling
I_{Halo}	Intensities resulting from the amorphous phase
IND	Indomethacin
N	Naproxen
N_2	Nitrogen
NAP	Naproxen
NAP/IND	Co-amorphous naproxen-indomethacin
NCE	New chemical entities
NI	Naproxen-indomethacin
NMF	Naproxen molar fraction
$NMF_{Initial}$	Initial naproxen molar fraction in the amorphous phase
$NMF_{Residual}$	Residual naproxen molar fraction in the amorphous phase
NS	Naproxen-sodium
NSI	Naproxen-sodium-indomethacin

NSNI	Naproxen-sodium-naproxen-indomethacin
P_2O_5	Phosphorous pentoxide
PC-	Principal component
PCA	Principal component analysis
PFR	Pump feed rate
PLS	Partial least squares
REF	Reference sample
RIR	Relative intensity ratio
RIR_{Halo}	Relative intensity ratio of the halo
SC	Slow cooling
Tg	Glass transition temperature
TGA	Thermogravimetric analysis
T_m	Melting point
ver	Version
XRPD	X-ray powder diffractometry
α-IND	α-indomethacin
γ-IND	γ-Indomethacin

1 Zusammenfassung

Die meisten der neu entwickelten Arzneistoffe sind nur schlecht wasserlösliche Feststoffe. Durch diese Eigenschaft können diese zum Teil nicht oral verabreicht werden, da sie keine ausreichend hohe Konzentration im Verdauungstrakt erreichen, um aus dem Darmlumen in das Blut zu diffundieren. Viele dieser schlecht löslichen Arzneistoffe gehören zur Klasse 2 des biopharmazeutischen Klassifizierungssystems, was bedeutet, dass ihre schlechte Wasserlöslichkeit geschwindigkeitslimitierend für ihre orale Bioverfügbarkeit ist. Entsprechend groß ist das Interesse der Forschung an Methoden, um die Löslichkeit dieser Arzneistoffe zu verbessern ohne dabei die chemische Struktur des Zielmoleküls zu verändern.

Einer der vielversprechendsten Ansätze, um dieses Ziel zu erreichen, ist das Prinzip der Amorphisierung. Durch Amorphisierung wird das Kristallgitter des festen Arzneistoffs zerstört, was dazu führt, dass die Moleküle in einem ungeordneten Zustand vorliegen, wodurch die Stärke der Interaktion zwischen ihnen vermindert ist und ihr Auflösungsprozess in Wasser vereinfacht wird.

Obwohl Arzneistoffe auch einzeln, also ohne Zusatz anderer Stoffe, amorphisiert werden können, zeigen diese in der Regel nur eine begrenzte physikalische Stabilität, weshalb Stabilisatoren zugesetzt werden. Einer der aktuellsten Ansätze ist die Verwendung niedermolekularer anstatt hochmolekularer, polymerer Hilfsstoffe. Systeme, die aus mindestens zwei nebeneinander amorph vorliegenden niedermolekularen Verbindungen bestehen und eine Phase bilden, werden co-amorph genannt. Beispielsweise kann co-amorphes Naproxen/Indomethacin für ca. 30 Tage physikalisch stabilisiert werden, bevor es erste Rekristallisationserscheinungen zeigt. Im Gegensatz dazu würde Naproxen allein sofort nach Amorphisierung rekristallisieren, während dies bei Indomethacin wenige Tage dauert.

Die Herstellung co-amorpher Systeme mittels pharmazeutischer Fertigungsprozesse und ihre physikalischen Eigenschaften in Abhängigkeit von den Prozessparametern wurde bisher noch nicht untersucht. Deshalb wurde im ersten Kapitel dieser Arbeit co-amorphes Naproxen/Indomethacin als Modellsystem ausgewählt, um beispielhaft die Herstellbarkeit co-amorpher Systeme mittels Sprühtrocknung zu untersuchen. Die Studie zeigt, dass die initiale Amorphizität der Proben und ihre physikalische Stabilität abhängig waren von den Prozessparametern Sprührate und Inlet-Temperatur, und dass die besten Ergebnisse bei mittleren Centerpoint-Bedingungen erreicht werden konnten. Die durch Sprühtrocknung hergestellten Proben waren jedoch weniger stabil als Proben, die mittels Melt-quenching hergestellt wurden.

In der zweiten Studie dieser Arbeit wurde untersucht, ob die physikalische Stabilität des Modellsystems Naproxen/Indomethacin optimierbar ist, da das mittels Melt-quenching hergestellte System bereits nach etwa 30 Tagen zu rekristallisieren begann. Es konnte gezeigt werden, dass die Kühlgeschwindigkeit während des Melt-Quenchings einen erheblichen Einfluss auf die resultierende physikalische Stabilität des Systems hat und dass die mittlere und nicht die maximale Kühlrate die besten Ergebnisse lieferte. Des Weiteren wurde die Abhängigkeit der physikalischen Stabilität vom Naproxen/Indomethacin-Verhältnis untersucht, wobei sich herausstellte, dass das optimale Verhältnis der eutektischen und nicht der äquimolaren Mischung entspricht. Darüber hinaus wurde gezeigt, dass der Großteil der Systeme, welche nicht der eutektischen Zusammensetzung entsprachen, solange rekristallisierten bis die eutektische Mischung in der verbleibenden co-amorphen Phase erreicht wurde.

Obwohl die physikalische Stabilität von co-amorphem Naproxen/Indomethacin in der zweiten Studie verbessert werden konnte, wurden nach spätestens 112 Tagen Rekristallisationspeaks gefunden. Deshalb wurde in einer dritten Studie Naproxen durch Naproxen-Natrium ausgetauscht, um die Glasübergangstemperatur des Systems zu steigern und gleichzeitig das pharmakologische Profil nicht zu verändern. Die Proben wurden circa 270 Tage lang untersucht und für die Proben, die direkt nach der Herstellung amorph waren, konnte keinerlei Rekristallisation nachgewiesen werden. Darüber hinaus wurde die intrinsische Lösungsgeschwindigkeit untersucht und festgestellt, dass diese um den Faktor zwei verbessert, also die physikochemischen Eigenschaften des Systems optimiert werden konnten.

In der vierten Studie wurde ein multivariates Quantifizierungsmodell basierend auf PLS-Regression aufgestellt, um die Festphasenzusammensetzung von co-amorphem Naproxen/Indomethacin zu bestimmen. Die Studie lieferte gute PLS-Modelle für jede der vier Komponenten Naproxen, γ-Indomethacin, α-Indomethacin und die co-amorphe Phase.

2 Abstract

Most of the new chemical entities that are developed as active pharmaceutical ingredients are only poorly water soluble solid materials. Therefore, administration via the preferred oral route may not be possible because these APIs do not dissolve fast enough in the digestive media. However, dissolution is a prerequisite to allow a sufficient transport from the gastrointestinal tract into the blood stream. Many of these poorly soluble APIs belong to class 2 of the Biopharmaceutics Classification System, which means that their poor solubility represents the

rate limiting step upon oral administration. Thus, there is an increasing interest in methods to improve the solubility of these APIs without chemically modifying the structure of the API molecules.

One of the most promising approaches to reach this goal is the concept of amorphisation. Upon amorphisation, the crystal lattice of solid APIs is destroyed, i.e. the strength of intermolecular interactions between the molecules is minimized, which facilitates their dissolution in water. Although amorphisation of single APIs can be realized, they usually show only limited physical stability and thus stabilizing agents must be added. One of the most recent concepts involves small molecule compounds instead of polymers as stabilizing agents to form so-called co-amorphous systems. In these systems, at least two small molecule compounds are dissolved in each other, thus being present in the glassy state. For example, co-amorphous naproxen/indomethacin can be kept amorphous for some weeks, while naproxen and indomethacin separately would recrystallize instantly or days after amorphisation, respectively.

However, preparation of co-amorphous systems by pharmaceutical processes and the dependence of the resulting physical stability on the applied process conditions has not been investigated so far. Therefore, in the first chapter of this work, co-amorphous naproxen/indomethacin was selected as model system to investigate the manufacturability of such systems by spray-drying. This study revealed that the initial amorphicity of the obtained samples was dependent on the process parameters pump feed rate and inlet temperature, while the best results were obtained at centerpoint conditions. However, spray-drying led to samples that were less stable compared to those that were prepared by melt-quenching.

In a second study, it was investigated whether the physical stability of naproxen/indomethacin could be further improved, as recrystallization could only be prevented for about 30 days when prepared by melt-quenching. It was shown that the cooling rate had a significant effect on the resulting physical stability of the system with intermediate cooling leading to the optimal result. Moreover, the dependency of the physical stability on the naproxen/indomethacin ratio was investigated and revealed that the optimal composition was at the eutectic and not at the equimolar ratio. Furthermore, it was shown that naproxen/indomethacin systems at other ratios recrystallized until the eutectic ratio in the residual amorphous material was reached.

Although the physical stability of co-amorphous naproxen/indomethacin could be improved based on the second study, recrystallization occurred after 112 days latest. To optimize this stability, a third study was carried out. Here, naproxen was exchanged by its sodium salt to increase the glass transition temperature of the system, while preserving the pharmacological profile. The samples were investigated for about 270 days and recrystallization could be

completely prevented for most compositions. Furthermore, the intrinsic dissolution rate could be increased by a factor of 2 and thus an optimization of the physicochemical properties was achieved.

In a fourth study, a multivariate quantification model based on a partial least squares regression was established to determine the solid-state composition of co-amorphous naproxen/indomethacin during recrystallization. The study revealed good PLS models for either of the four components: naproxen, γ-indomethacin, α-indomethacin and the co-amorphous phase.

3 Introduction

3.1 The Biopharmaceutics Classification System

The number of new chemical entities (NCEs) that are poorly soluble has increased significantly and today about 70 % of all NCEs belong to this group [1,2]. As the drug solubility also influences the resulting dissolution rate, the solubility is a crucial factor for the bioavailability of orally administered drugs [3]. To classify the biopharmaceutical and physicochemical properties of active pharmaceutical ingredients (APIs) with regard to their successful development, the biopharmaceutics classification system (BCS) has been introduced [4] (Table 1). It distinguishes between four categories of drug substances based on their solubility and permeability, which are: class 1: high water solubility and high permeability, class 2: low water solubility and high permeability, class 3: high water solubility and low permeability and class 4: low water solubility and low permeability.

If the BCS is combined with the in vitro dissolution characteristics of an API, the system takes three main factors into account: solubility, permeability and the dissolution rate, which all together determine how fast and to what extent the respective API will become available in the blood stream after oral administration. The solubility and permeability are parameters of an API, which are affected by its chemical structure. However, the dissolution rate of an API is dependent on several factors according to the equation by Noyes and Whitney [5]:

$$\frac{dM}{dt} = \frac{D \cdot A \cdot (Cs - C)}{d} \qquad \text{Equation 1}$$

dM/dt = API mass that dissolves per time unit

D = Diffusion coefficient of the API

A = Particle contact area of the API particles in the dissolution medium

Cs = API solubility

C = Actual API concentration in the dissolution medium

d = Thickness of the diffusion layer

Table 1: The biopharmaceutics classification system (modified from [3])

Class 1: High solubility/high permeability	Class 2: Low solubility/high permeability
1) Immediate release dosage forms	1) Crystal modifications metastable polymorphs salt formation cocrystal formation 2) Immediate release oral dosage forms with surfactant 3) Particle size reduction micronization nanocrystals 4) Amorphisation 5) pH modification
Class 3: High solubility/low permeability	Class 4: Low solubility/low permeability
1) Immediate release dosage forms with absorption enhancer 2) Immediate release solid dosage forms	1) Combination of approaches for BCS class 2 and adsorption enhancer 2) Same approaches as BCS class 2

The diffusion coefficient describes the inherent mobility of a drug molecule in a selected medium and cannot be changed without an alteration of the chemical structure of the API. In contrast, the thickness of the diffusion layer, the API particle contact area as well as the API solubility may be adjusted by application of different strategies. However, most of the strategies described as follows influence the last two dissolution parameters.

For BCS class 1 drugs, which are defined as highly soluble and highly permeable, there is no a rate-limiting step for the drug to become orally available, because the drug dissolves very fast in the aqueous digestive media before a fast transport through the intestinal membrane. The respective APIs can thus be formulated as conventional solid oral dosage forms such as tablets or capsules [3].

In contrast, BCS class II drugs, to which most of the NCEs belong nowadays, are poorly soluble but still highly permeable. This means, that a certain amount of undissolved drug being present in the digestive tract is absorbed very fast, if a fraction of the undissolved drug dissolves in the digestive medium. Concepts to increase the bioavailability of such APIs by technological strategies aim at reaching an API concentration of the dissolved drug in the digestive medium as high and as fast as possible. On the one hand, an increase in API concentration may be

achieved by enhancing the dissolution rate of the API to reach its solubility as fast as possible, e.g. by micronization, which may already have a notable effect on the bioavailability [6].

On the other hand, it is possible to increase the bioavailability of an API by maximizing its solubility through nano-crystallization, cocrystallisation, metastable polymorphism, salt formation or amorphisation [3]. An increase in saturation solubility simultaneously results in a higher dissolution rate according to Noyes and Whitney (Equation 1).

3.2 Dissolution enhancement strategies

3.2.1 Micronization

Taking Equation 1 into account, micronization represents the most obvious approach to increase the dissolution rate of an API, because the dissolution rate increases proportionally to the contact area of the API particles [5]. Besides the increase of the contact area, micronization will also result in a decrease of the diffusion layer thickness [7]. Typical processes to accomplish micronization down to a particle size of 2-3 µm involve jet milling, ball milling or pin milling. However, aggregation may be induced by micronization, which again decreases the particle contact area. This problem may be solved by wetting or peptization.

3.2.2 Nanocrystallisation

Reduction of the particle size below the typical micronization level to less than 1-2 µm results in an increase of the API solubility as well as the particle the contact area and a decrease of the diffusion layer thickness [8]. Commonly, nanocrystal formulations are prepared by wet bead-milling, controlled precipitation or high-pressure homogenization [9]. After a subsequent drying process, the nanocrystals can be stabilized with suitable carriers to form a crystalline solid dispersion. A comparison of nanocrystal with microcrystal formulations showed that increased bioavailability's with c_{max} values of up to the factor of 60 could be achieved.

3.2.3 Cocrystallisation

Cocrystals are crystalline materials that consist of at least two different chemical compounds in a defined stoichiometry [10]. In pharmaceutical environments they typically involve an API plus an excipient molecule, which is called cocrystal former. In contrast to salt formation, no proton transfer occurs from one compound to the other and therefore the components remain uncharged. However, hydrogen bonding is often required to reach the formation of stable cocrystals. The improved dissolution behavior of cocrystals has been confirmed in vitro and in vivo [11,12].

3.2.4 **Metastable polymorphism**

If one compound can crystallize in more than one crystal lattice structure, which is the case with most solids, it shows polymorphism [13] and each of the respective polymorphs shows different physicochemical properties such as melting point, density, solubility and physical stability [14]. However, the maximum solubility increase that can be reached by change of the polymorphic form has been reported to be less than 2-fold [15]. Furthermore, the most stable polymorph will be formed upon dissolution, which also limits the application of this concept.

3.2.5 **Salt formation**

Generally, salts of basic or acidic drugs show higher solubilities compared to their respective free acid or free base counterparts, which also results in higher dissolution rates. Kramer and Flynn [16] showed the dependence of the base drug solubility on the pH (Fig. 1).

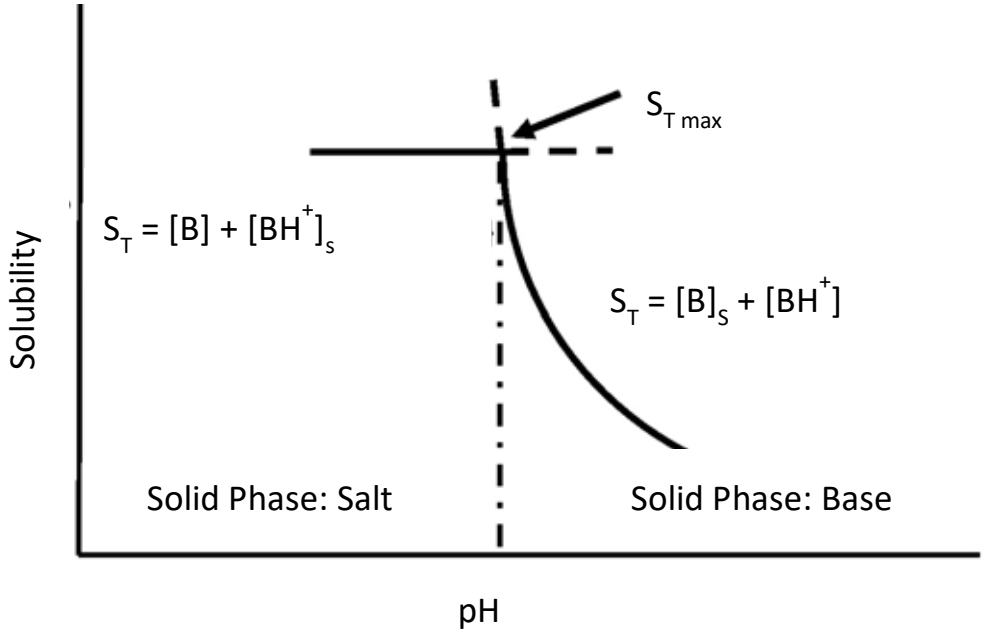

Fig. 1: Solubility of a base in dependence of the pH (modified from [3])

S_T = Total solubility of a base
$[B]_s$ = Solubility of the free base
[B] = Concentration of the free base
$[BH^+]_s$ = Solubility of the protonated form of a base
$[BH^+]$ = Concentration of the protonated form of a base

If the pH is high, the concentration of hydronium ions is low and the free base is predominantly present at its constant solubility $[B]_s$. In contrast, if the pH is low i.e., the hydronium ion concentration is high, the base is predominantly present in the protonated form at its constant

solubility $[BH^+]_s$. Therefore, the total solubility of a base in solution S_T, that is reached in dependence of the pH, is determined by the concentration of its non-protonated form [B] plus the concentration of the protonated form $[BH^+]$.

$$S_T=[B]+[BH^+] \quad \text{Equation 2}$$

However, in some cases, it may not be possible to prepare a salt, that leads to the desired increase of the solubility and bioavailability. Furthermore, salt formation involves the insertion of a counterion, for example Cl^- if the hydrochloride salt of a basic drug is prepared. However, these counterions may also present a problem for the resulting solubility of the drug. Supposed that a significant number of excess counterions is exposed to the protonated drug in solution, precipitation and thus a pronounced decrease in the solubility may occur if the solubility product of the protonated drug and the counterion is exceeded (common ion-effect).

3.2.6 **Amorphisation**

3.2.6.1 **Preparation of amorphous solids**

Preparation of amorphous solids can be carried out by application of three different technical approaches. The first approach is kinetic disordering, a process that can be achieved via a direct disruption of the crystalline lattice through mechanical activation, for example by milling [17,18]. The other two options involve the transformation of the crystalline solid into a non-crystalline form that is thermodynamically stable and can be obtained by either dissolving the solid in an appropriate solvent or by melting. Subsequently, the solvent must be rapidly evaporated while the melt has to be rapidly cooled down [17–20] to transform the solid material into its amorphous form and prevent recrystallization.

If the molten API is cooled down, it normally recrystallizes below its melting temperature, resulting in an abrupt decrease of the system's enthalpy and specific volume, unless the system is cooled down fast enough. If recrystallisation below the melting temperature can be avoided, the melt is present in the so-called supercooled liquid state. With a further decrease of the temperature, the molecular motion becomes more and more limited and at the glass transition temperature (Tg) the molecules freeze [17,18]. An explanation for this phenomenon is that the time needed by the molecules to arrange themselves appropriately, i.e. in the form of crystals, is not sufficient. At the Tg, a discontinuity in enthalpy and specific volume occurs, which both will decrease slower below the Tg as a function of the temperature. At this stage, the system is present in the glassy, amorphous state.

3.2.6.2 **Increased solubility of amorphous solids**

Amorphous solids show altered physicochemical properties compared to the crystalline counterpart, such as an increased solubility or chemical reactivity, which results from to the higher enthalpy of the amorphous system and from the absence of a long range order [3]. However, as the amorphous state is no equilibrium state with respect to the crystalline form, amorphous solids may spontaneously recrystallize to their crystalline counterparts. Parks and co-workers [21] have tried to correlate the relative solubility of the amorphous form in comparison to the crystalline form according to the difference in free energy of the two forms applying the following equation:

$$\frac{S_{am}}{S_{cr}} = e^{\left(\frac{\Delta G}{-R \cdot T}\right)} \qquad \text{Equation 3}$$

ΔG can be calculated based on ΔH and ΔS:

$$\Delta G = \Delta H - T \cdot \Delta S \qquad \text{Equation 4}$$

ΔH may be calculated according to:

$$\Delta H_{am\text{-}cr} = \Delta H_{fus} - \Delta cp \cdot \Delta T \qquad \text{Equation 5}$$

ΔS may be calculated according to:

$$\Delta S_{am\text{-}cr} = \frac{\Delta H_{fus}}{T_m} - \Delta cp \cdot \ln \cdot \Delta T \qquad \text{Equation 6}$$

$S_{am\text{-}cr}$ = Solubility difference between the amorphous and crystalline form
ΔG = Gibbs free energy difference (G_{final} - $G_{initial}$)
R = Universal gas constant
T = Absolute temperature
ΔH = Enthalpy difference (H_{final} - $H_{initial}$)
ΔS = Entropy difference (S_{final} - $S_{initial}$)
$\Delta H_{am\text{-}cr}$ = Enthalpy difference between the amorphous and crystalline form
ΔH_{fus} = Enthalpy of fusion
ΔT = Temperature difference (T_m - T_{actual})
Δcp = Heat capacity difference (cp_{cr} - cp_{am})

Equation 5 describes that the enthalpy difference between the amorphous and the crystalline state can maximally be equal to the enthalpy of fusion, which applies if the system is present in the molten state at T_m. In this case, the term '$\Delta cp * \Delta T$' may be deleted from the equation.

However, if the temperature is decreased below the melting temperature and the material is transformed into its amorphous state, it loses enthalpy by $'\Delta cp * \Delta T'$. The physical quantities $\Delta H_{fus,}$ T_m and Δcp may be determined by differential scanning calorimetry (DSC).

3.2.6.3 **Physical Stability of amorphous solids**

Crystallization of amorphous solids is driven by two mechanisms, first by nucleation of the molecules as the initial step to form stable nuclei and second by the subsequent growing process of these nuclei until the solid is fully crystallized. From a thermokinetic point of view, the nucleation process is favored at higher temperatures, because higher molecular mobilities increase the probability for an appropriate rearrangement of the molecules to to form the crystalline phase. However, thermodynamically the nucleation process is favored at low temperatures, because of the exothermal character of the recrystallization process. The maximum recrystallization rate will therefore be reached at temperature between T_m and Tg [17,18,22].

Storage of amorphous solids at least 50 °C below their Tg to decrease the molecular motion is considered sufficient to reduce the recrystallization tendency significantly [20]. Nevertheless, the residual molecular motion in amorphous solids below their Tg is still sufficient to trigger recrystallization being relevant for storage time periods of pharmaceutical products [23–25]. If looking for the optimal storage temperature for a maximum stable amorphous solid, the Kautzmann temperature T_k as well as the fictive temperature T_f have been discussed (Fig. 2). If an API, present in the supercooled liquid state, would be further cooled down at an (theoretically) extremely slow cooling rate until its enthalpy or specific volume approaches the value of the crystalline state of the API, the Kautzmann temperature is reached.

At this temperature, molecular motions are considered negligible and the physical stability should be maximal. Therefore, if T_K is reached, the system enthalpy is so small that molecular motions do not play an important role for the physical stability of the hypothetical supercooled liquid anymore [26]. However, this approach considers the enthalpy of the (hypothetical) supercooled liquid state but not the real glass state. If the enthalpy of the real glass state ("a" at T_a in Fig. 2) equals the enthalpy of the hypothetical supercooled liquid, T_f is reached and the real glass state should be considered physically stable. However, typical T_f values are in the area of refrigerator temperatures and therefore costly with regard to the logistical effort [20].

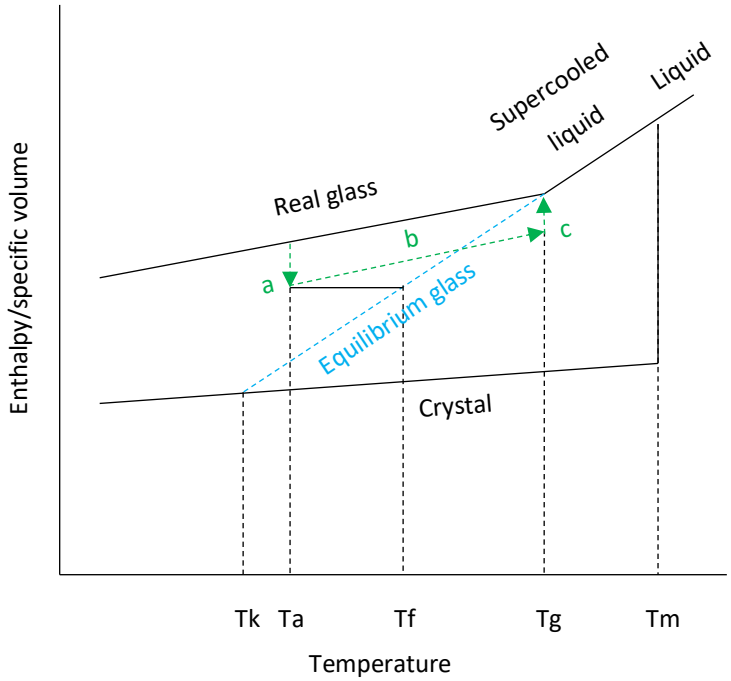

Fig. 2: Enthalpy in dependence of the temperature modified from [21]

T_f = Fictive temperature

T_a = Aging temperature

T_K = Kautzmann temperature

a = Enthalpy loss upon aging

b = Enthalpy increase upon heating below the Tg

c = Enthalpy increase upon heating at the Tg

Generally, recrystallization of amorphous solids is influenced by various factors including thermokinetics, thermodynamics, molecular interactions, preparation methods and process parameters. However, molecular mobility represents the main factor that affects the resulting physical stability of an amorphous solid. A maximum stability of amorphous solids is expected for those that have high Tgs, low molecular mobilities and high Kautzmann temperatures [27].

In the field of amorphous pharmaceuticals the term „pseudo-polyamorphism“ is important and means that one amorphous state is not necessarily identical with another amorphous state. This phenomenon is observed as different amorphous states will result if the same material is prepared at different process conditions, with different preparation techniques or at different storage settings. These procedures may lead to different molecular environments in the amorphous material and may result in altered physical properties such as thermal behavior

[28]. For instance, if an amorphous solid is prepared at rather high cooling temperatures, a correspondingly high Tg is usually observed.

3.2.6.4 **Polymer glass solutions**

APIs can be transferred into their amorphous form by embedding them within a polymer matrix, such as PVP [29]. The resulting systems are called polymer glass solutions, because the API is molecularly dispersed in the polymer matrix and the system is present in the glassy state [30]. The resulting physical stability of such a system is usually increased because of the higher glass transition temperature of polymers, which leads to an increase the Tg of the whole system and lowers its molecular motion in comparison to the respective plain amorphous drug [23,31]. Furthermore, interactions between the APIs and the polymers are considered important to provide a sufficient stabilization [31,32].

In comparison to conventional tablet formulations, the preparation of polymer glass solutions has many practical limitations which arise from problems during manufacturing, formulation into dosage forms and the variability of their physicochemical properties and their stability [33–35,23].

Dosage form development of solid glass solutions involves the transformation of the initial polymer glass solution into administrable units such as tablets or capsules. After a melt or solution was initially prepared, a hardening or solvent removal process usually follows. Subsequently, pulverization of the amorphous bulk materials has to be performed. Standard problems that occur during the pulverization step are caused by the sticky [36] and soft character of solid polymer solutions and may result in poor mixability, flowability and compressibility [37]. In this context, wet granulation cannot overcome the above mentioned limitations, because water usually acts as plasticizer, decreases the glass transition temperature and induces crystallization in the respective glassy material [18,38]. However, in-situ dry granulation may be an alternative to enable pulverization [39]. Another problem that arises during pulverization is the induction of high energy sites in the amorphous material that can trigger recrystallization [22]. However, once the final dosage form is prepared, its disintegration may be problematic, even though disintegrants are part of the formulation. The waxy character of the polymers may lead to plasticization upon compaction finally resulting in polymer-coated disintegrant molecules, making them useless [40].

In addition to the challenging formulation development of polymer glass solutions, the physical stability of the incorporated APIs is often limited and thus recrystallization may proceed accompanied by a loss of the improved physicochemical properties [30,41]. To obtain stable

polymer glass solutions and to avoid API recrystallization, a sufficient solubility of the drug within the polymer is required. If the required dose of an API does not dissolve in the polymer matrix, the polymer amount has to be increased to achieve a stable glass solution [42]. This addition of polymer decreases the drug to polymer ratio and increases the mass of the final dosage form while reducing the convenience of application. Thus, to ensure a sufficient physical stability of the polymer glass solutions, polymer screening is necessary to find a suitable candidate [43]. Ultimately, these problems have led to only a limited number of marketed products that are currently available as polymer glass solutions.

3.2.6.5 **Mesoporous Systems**

As mentioned in the previous chapter, the formation of polymer glass solutions requires the formation of a single amorphous phase and therefore, a certain miscibility of the used compounds. As a different approach, which does not require miscibility, porous materials or adsorbents such as silicon dioxide or silicates can be applied [44]. These materials are called mesoporous systems, i.e. materials that have pore volumes of about 1 cm^3/g with correspondingly large surface areas of > 500 m^2/g [45]. The rather high surface areas result in high free surface energies that may be reduced by adsorption of molecules such as APIs. Upon adsorption, the API molecules loose their crystalline structure and are present in their amorphous form [44]. Besides the thermodynamical aspect, the size of the involved pores in the mesoporous materials limits the possibility of the API molecules to rearrange to a critical nucleation size.

APIs may be incorporated into mesoporous materials by different techniques: solvent deposition, mechanical activation or vapor phase mediation [44].

With solvent deposition, the respective drug must be dissolved in a suitable organic solvent before the mesoporous material is added to the solution to allow the API to adsorb to the mesoporous material. Subsequently, the solvent is removed e.g. by filtration, centrifugation or heating. However, only a monolayer of the API can be adsorbed to the carrier material and API and residual solvent are competing for adsorption. Therefore, a high drug load is preferred to increase the amount of API in the monolayer.

Another approach to adsorb APIs to mesoporous systems (under exclusion of organic solvents) is mechanical activation [46–48]. Here, different mechanisms are discussed: A) the increase of shear forces by milling resulting from the added mesoporous material and B) the reduction of the activation energy for the amorphisation of the crystalline to the adsorbed amorphous state. Another non-solvent approach is the vapor phase-mediated amorphisation

as a spontaneous mechanism, that may be observed if a physical mixture consisting of only an API and a mesoporous carrier material is prepared. For this mechanism, it was suggested that the API spontaneously diffuses into the pores of the mesoporous materials [49], while the rate of amorphisation correlated with the vapor pressure of the respective guest compounds [50]. With this mechanism, only simple processing is necessary to allow manufacturing in a scaled up manner [51,52].

3.2.6.6 **Co-amorphous systems**

With polymer-based glass solutions, the API is molecularly dispersed in the polymer matrix and both components are present in the amorphous state while they form one single amorphous phase. However, drugs often show only a limited solubility in polymeric carriers of < 20 % [53]. If the concentration of the API in the carrier exceeds its solubility, phase separation and subsequent API recrystallization will result. Thus, to incorporate a defined amount of drug into a polymer, a high amount of polymer will be necessary and can result in bulky dosage forms, which may reduce the patient compliance. To reduce the size of the dosage form, the molecular weight of the carriers may be decreased leading to the concept of co-amorphous systems. In these systems small molecule APIs are molecularly mixed with a small molecule stabilizer, both present in their amorphous form [54–56].

- **The influence of Tg**

In contrast to polymers, amorphous small molecule compounds usually show relatively low Tgs and the resulting Tg of a respective binary mixture will be located between the Tg of the two individual compounds (Gordon Taylor equation):

$$T_{g12} = \frac{w_1 \cdot T_{g1} + K \cdot w_2 \cdot T_{g2}}{w_1 \cdot K \cdot w_2} \qquad \text{Equation 7}$$

$$K = \frac{T_{g1} \cdot \rho_1}{T_{g2} \cdot \rho_2} \qquad \text{Equation 8}$$

Tg_{12} = Glass transition temperature of the binary mixture
Tg_1 = Glass transition temperature of the amorphous component 1
Tg_2 = Glass transition temperature of the amorphous component 2
K = Constant according to Equation 8
w_1 = Weight fraction of component 1
w_2 = Weight fraction of component 2
ρ_1 = Powder density of component 1
ρ_2 = Powder density of component 2

Thus, the Tg of co-amorphous systems is usually lower compared to the Tg of glass solutions that include a polymer [17]. Once the Tg of an amorphous phase is reached, the material undergoes a transformation from its glassy to its supercooled liquid state [17,18] and the molecular mobility strongly increases. Thus, crystallization proceeds much faster with materials that show Tgs close to the temperature of the environment and limits their physical stability if the difference between the Tg and the environmental temperature does not exceed about 50 °C [18,20,57–59]. Therefore, the ability to maintain the amorphous character of co-amorphous systems with low Tgs may appear limited in comparison to polymer-based solid solutions with high Tgs. However, while the antiplasticizing effect in polymer based glass solutions represents the key factor for their improved physical stability, antiplasticizing is of minor relevance for the stability of co-amorphous systems.

Regardless of the usually low Tgs of small molecules, several small molecule excipients show Tgs far above room temperature such as the amino acid tryptophan with its Tg of 140 °C [60]. Also, ionic components may increase the Tg of co-amorphous systems [61–64] and thus further improve their physical stability.

- **The influence of intermolecular interactions**

Regarding the only slightly pronounced antiplasticizing effect in most small molecule co-amorphous systems, a different mechanism, i.e. intermolecular interactions between the involved components, play the more important role for the physical stability [63]. For example, the analgesic API naproxen cannot be maintained in its amorphous form at room temperature (Tg of about 5°C, [65]). Instead, equimolar co-amorphous naproxen/indomethacin shows no recrystallization for 56 days despite its low Tg of about 25 °C [66].

Although no molecular long range order is present in amorphous solids, it has been reported that short range order interactions take place in single amorphous as well as in co-amorphous systems [56,60,65,67–73]. These interactions include hydrogen bonding or π-π interactions that can take place between equal as well as unequal molecules. In co-amorphous systems, these interactions between unequal molecules may result in the formation of heterodimers [65,74,75], as has been reported for naproxen/indomethacin, and present an energetical barrier that has to be overcome before the molecules can rearrange to form homodimers [71,76] and finally crystallize. Co-amorphous systems may also be prepared under ionization of the two components by proton transfer, which has been described for co-amorphous cimetidine-indomethacin where the carboxyl group of indomethacin causes the protonation of the imidazole ring of cimetidine [71,76]. Besides co-amorphous systems consisting of two pharmacologically combinable APIs such as naproxen and indomethacin, APIs may also be

mixed with one or more pharmacologically inactive excipient molecules such as amino acids to form binary or ternary co-amorphous systems [77–80].

- **The relation between the Tg and molecular interactions**

In the case of co-amorphous naproxen/indomethacin, the experimental Tgs of different blend ratios showed deviations from the calculated values according to the Gordon-Taylor equation (Equation 7). It was assumed that intermolecular interactions take place between the components [58,81–83], because the Gordon-Taylor equation does not consider such interactions and assumes the presence of ideal blends. The biggest Tg difference between the theoretical and the experimental values was observed at the equimolar ratio, i.e. the ratio with the maximum of molecular interactions between naproxen and indomethacin. Therefore, Löbmann et al. recalculated the Tg according to Gordon and Tayler, considering equimolar co-amorphous naproxen/indomethacin to be one single phase in the equation, while the excess amount of either naproxen or indomethacin was defined as the second phase. The recalculated Tgs were found to fit the experimental data, which supports the assumption that naproxen and indomethacin form a special single amorphous phase at the equimolar ratio.

- **Co-amorphous systems without interactions**

Interestingly, co-amorphous systems with a low Tg such as simvastatin-glipizide were reported to be physically stable but do not show intermolecular interactions. However, they both still form a single co-amorphous phase as suggested by the single Tg that was found by DSC, being a prerequisite for co-amorphous systems. Therefore, it is assumed that the two components are molecularly dispersed in each other accompanied by spatial separation of equal molecules. This stabilization mechanism was proposed not only for simvastatin-glipizide [84] but also for ritonavir-indomethacin [85] and their observed high physical stabilities were attributed to the slow phase separation process of the components. However, in contrast to co-amorphous systems with stabilizing intermolecular interactions, phase separation is assumed to proceed faster if no such interactions take place.

- **Dissolution enhancement**

As already discussed, intermolecular interactions between the same molecules in amorphous phases are less pronounced compared to their crystalline counterparts because of the presence of only short range instead of long range molecular interactions. Therefore, amorphous materials show a higher apparent solubility and dissolution rate compared to their crystalline forms [18,54,86,87]. With co-amorphous systems, it is possible to further increase

the dissolution rate of the involved compounds in comparison to their respective single-amorphous phases [65,85,80,84,60,61,88,89].

Besides this improved dissolution rate, it was reported that recrystalliatzion of cimetidine in co-amorphous naproxen/cimetidine and lurasidone-HCl in lurasidone-HCl/saccharin could be prevented during the dissolution experiments, which was not the case with the respective pure amorphous solids [80,89].

Additionally, with co-amorphous naproxen/indomethacin and naproxen-cimetidine even a synchronized release of both compounds was observed. this observation was attributed to the strong intermolecular interactions that resulted in the formation of heterodimers [65,89]. This finding led to the hypothesis that a readily water soluble coformer may facilitate the dissolution process of a second, poorly soluble API [60,64,61]. This concept was tested and confirmed by Jensen et al., who showed that the addition of the highly water soluble amino acid proline further improved the dissolution rate of two naproxen-amino acid co-amorphous systems [61]. However, if the strength of the intermolecular interactions between the API and the coformer is not sufficient or/and the water solubilities of both compounds are too different, the API may separate from the coformer upon dissolution leading to a loss of the dissolution enhancement effect [64].

Besides the possibility of modifying dissolution rates and circumvent recrystallization in water, it was also shown that co-amorphous systems may lead to supersaturation during dissolution experiments in a more distinct way compared to the respective single amorphous APIs [90,88].

Studies regarding the in-vivo performance of co-amorphous systems are limited [91,75,92] and none of them has been carried out involving a control group for the respective single-amorphous API. Therefore, the effect of co-amorphous systems on the bioavailability is still unknown.

- **Methods for characterization of co-amorphous systems**

– **Differential scanning calorimetry**

Differential scanning calorimetry is a technique that involves the investigation of the thermal behavior of a given material upon heating. DSC is based on the measurement of the temperature difference between two furnaces that are both present in a single oven, which is heated up linearly. Right below the two furnaces, temperature sensors are located to measure the temperature of the furnaces upon a given temperature program.

If one of the furnaces contains a material without phase transition occurring during heating (e.g. melting of the material), a small temperature difference will be detectable upon heating which will result in a temperature offset, because of the materials' heat capacity. The heat capacity is the energy that is needed to achieve a certain temperature change of the material. The temperature offset that will be detected is proportional to the mass and heat capacity of the material.

If the empty reference furnace and the material-containing sample furnace are linearly heated and a phase transition occurs, the temperature of the sample furnace does not further increase until the phase transition is completed. Thus, a temperature difference between the two furnaces results, which is proportional to the heating rate. The difference between $T_{Reference}$ and T_{Sample} may be integrated during the melting process and results in an area, which is proportional to the heat of fusion of the sample and may be quantified by calibration with a standard. The Heat Flux DSC is based on this concept.

In contrast, the Heat Flow DSC is not based on a temperature measurement – it directly measures the heat flow of heat in and out of a sample. In a Heat Flow DSC the energy, that is necessary to keep both temperatures constant, is measured. The resulting energy that is transferred to the sample during a certain time period can directly be used to determine the heat of fusion.

If the glass transition temperature of an amorphous solid is determined by DSC, an endothermal event will be detected. At the Tg the heat capacity of the material increases and corresponds to the distance of the extrapolated heat curves before and after the Tg event. However, the Tg may be overlapped with an enthalpy recovery event. In this case, the heat curve before the Tg event (endothermic direction down) falls below the heat curve level after the Tg. This energy difference results from relaxation of the amorphous phase, which means that the material falls below the energy level of the initial glass state. Upon heating, the temperature of the material increases until the Tg is reached. In this case, the material needs more energy to undergo the glass transition, which is proportional to the relaxation enthalpy [57].

- **Fourier-transformed infrared spectroscopy**

Fourier-transformed infrared spectroscopy is a vibrational spectroscopic technique that uses electromagnetic light with wavenumbers between 10 cm^{-1} and 12500 cm^{-1} to identify the chemical structure or chemical interactions between chemical structures and is based on electron excitation. The advantage of the Fourier-transformed version of infrared spectroscopy

is the better signal to noise ratio. Infrared light is distinguishable into three ranges: near infrared (12500 cm^{-1} - 4000 cm^{-1}), mid infrared (4000 cm^{-1} - 400 cm^{-1}) and far infrared (400 cm^{-1} - 10 cm^{-1}), in which different chemical phenomena are detectable. In the presented studies, the mid-infrared spectra were investigated, because in this range the relevant functional groups and hydrogen bonding interactions can be detected.

If IR radiation interacts with a molecule, certain light wavelengths are absorbed and result in molecular motions, which may be rotations of small molecules or vibrations of molecular bondings. The respective wavelengths of the IR spectrum are representative for the molecule and allows its identification by MIR spectroscopy. However, the interaction of the molecule with the light can only take place if the molecule has an inducible or variable dipole moment. Two possible vibrational modes may occur: vibration under deformation of the bonding angle and vibration alongside the bonding axis.

In an FTIR spectrometer, the IR light source emits polychromatic IR light, i.e. overlapping IR waves at several different wavelengths. Overlapping waves at different wavelengths result in certain amplitude signal, which in a first step must be detected by the FTIR spectrometer. In a second step, this amplitude has to be Fourier-transformed to extract the different wavelengths that are present in the detected amplitude signal.

The first step is realized by an interferometer. The polychromatic IR light is splitted into two beams, while the travel distance of beam 2 in comparison to beam 1 will be stepwise increased. Once the two beams are parallelized again, interference of the two IR beams results in constructive or destructive amplitude signals in dependence of the extended travel distance of beam 2. The detector, which is located behind the parallelized two beams, only measures the intensity of the resulting single IR beam after parallelization. The intensity is recorded in dependence as a function of the extended travel distance of beam 2. Because of the interference of the two beams the resulting power signal that is obtained by the detector, corresponds to the shape of the waveform of the emitted overlapping IR waves. Therefore, the overlapping waves signal of the continuous IR beam is transformed into a discontinuous power signal.

As the waveform of the overlapping IR waves is known, Fourier transformation may be performed, which is a mathematical procedure, that can decompose those overlapping waves signals into the involved wavelenghts and their respective intensities.

- **X-Ray powder diffractometry**

XRPD is an analytical method that can determine periodicities within powders, that result in constructive interferences in dependence of the X-ray angle of incidence. X-ray is an electromagnetic radiation with wavelengths between 1 and 10000 pm and is located next to the gamma radiation and the UV light in the electromagnetic spectrum. Diffraction generally occurs if the distance between lattice planes in a crystal structure is within the same order of magnitude as the wavelength of the respective incoming radiation. The concept of XRPD basically results from a scattering phenomenon that occurs if an X-ray beam at a constant wavelength interacts with crystalline, i.e. periodic, structures. Constructive interference will only occur, if the Bragg equation is applicable.

$$n \cdot \lambda = 2 \cdot d \cdot \sin(\Theta) \qquad \text{Equation 9}$$

λ = Wavelength of the X-rays

d = Distance between the lattice planes

Θ = Angle of incidence of the X-rays

n = integer

The Bragg equation describes that constructive interference results, if the difference in travel distance of two X-rays is equal to an integer of the incoming wavelength of the X-rays ($n\lambda$). The difference in the travel distance between two X-ray beams is dependent on the distance of the lattice planes (d) and the angle of incidence of the incoming radiation (Θ). The deflection angle of the radiation that results from the constructive interference is 2Θ. Therefore, XRP-diffractograms display diffraction peaks relative to 2Θ. The different lattice planes can be detected by changing the angle of incidence of the incoming radiation.

XRPD can be used for quantitative as well as qualitative investigations of solid blends and the measurements are based on X-ray diffraction patterns, which are unique for each crystalline material. XRPD is a very useful technique because it is usually non-destructive and no or only little sample pretreatment is necessary. However, XRP-diffractograms do not provide any chemical information on the investigated substance and the technique is time-consuming, which are the disadvantages of this technology in comparison to spectroscopic methods such as FTIR.

X-ray powder diffractometry (XRPD) also offers the opportunity to analyze the phase composition of solids in a quantitative manner. The classical evaluation methods to quantify multicomponent samples based on XRPD data are the relative intensity ratio (RIR) method and the Rietveld method [30]. The RIR method takes the intensities of the XRPD signals of the

involved crystalline and amorphous components into account, as these are proportional to the fractions of the respective phases [31]. The RIR method is easy to use but may be limited regarding its accuracy [32,33] or if the peaks present in the diffractograms are not well separated [34].

Compared to the RIR method, the Rietveld method [35] presents the more accurate approach [33], which is based on a crystal structure model that is varied until a maximal fit of the hereby calculated theoretical and the recorded diffractogram is achieved [30]. Therefore, the quantification of an amorphous fraction using the Rietveld method is only indirectly possible [33] and it generally requires knowledge of the crystal structures of the crystalline components [36].

As an alternative method that provides determination accuracies comparable to those of the Rietveld method [37] but does not require knowledge of the crystal structure, multivariate partial least squares (PLS) regression may be used to quantify the multiphase composition of a given sample.

Rumondor et al. [32] showed that this approach was successful to quantify the crystalline felodipine fraction in blends of felodipine and its solid glass solution with polyvinylpyrrolidone and led to accurate predictions with significantly lower root mean square errors compared to results obtained by application of the RIR method. Furthermore, Caliandro et al. [37] reported that the combination of XRPD and PLS can deliver accurate results even for the quantification of mixtures that comprised four crystalline phases at the same time with accuracies comparable to those of the Rietveld method.

- **Data analysis**

Spectroscopic or diffractometric analytical techniques such as FTIR or XRPD are standard methods in the pharmaceutical field to extract physicochemical information from samples. However, the resulting spectra contain plenty data points, e.g. absorption values for several wavenumbers or constructive interference intensities for several angles of incidence. To correlate this data with the respective physicochemical sample properties, while eliminating biases that are not caused by the samples but by instrument-related or experimental phenomena, preprocessing of the spectra has to be performed. Upon offset correction, baseline shifts of spectra and diffractograms are removed by subtracting a value x from each single spectrum or diffractogram [93]. A normalization to unit area is another transformation method that allows the elimination of dataset biases that are mainly based on sample

concentration [94,95]. This is performed by dividing each data point of a spectrum or diffractogram by the sum of the variables of each dataset.

To extract information from a preprocessed dataset, it might be sufficient to take only one variable into account, e.g. a peak intensity, which may be correlated with a concentration of a certain material (univariate analysis). However, it must be ensured that the single-peak information is directly related to a specific sample property without interference resulting from other components of the sample. By multivariate analytical methods, many variables are analyzed at the same time. Basically, with multivariate analytical methods the reduction of variables within a dataset without deletion of the essential information is achieved.

PCA represents one of the multivariate analytical methods and is an exploratory mathematical procedure that reduces the complexity of each dataset. This method is conducted by orthogonal transformation of the initial variables into new uncorrelated principal components, which are linear combinations of these untreated variables [96,97]. Typically, a dataset in the present thesis has N samples (e.g. spectra or diffractograms) and each of the samples has M data points (e.g. number of absorbance or intensity values), which results in an N x M matrix. PCA will reduce the M-dimensionality to an A-dimensionality, resulting in an N x A matrix, which is called the PC space with N samples and A principal components. Throughout the experiments performed in this thesis, two or three principal components were sufficient to describe the majority of the differences in the sample information, i.e. PCA resulted in N x A matrices with A representing two or three columns. Each of the principal components is accompanied by one loading vector, while the loadings matrices have the same size M as the initial dataset. Based on the PCA, each sample in the presented studies could be described by two or three scores in addition to the two or three loadings matrices.

Partial least squares regression is a multivariate quantification procedure, which correlates a known numeric information of the samples with multidimensional data of these samples, e.g. FTIR spectra or diffractograms. After a calibration step, the numeric information of interest may be predicted based on the multidimensional calibration data for the unknown samples. Basically, a regression model is constructed with the variables of the multidimensional data X (N x M; spectral or diffractometric data), which are used as predictors for the response variables Y (N x K; e.g. concentration). During PLS regression, the X and Y matrices are both decomposed to obtain latent variables, that explain most of the variance of the X matrix while a maximum correlation with the Y matrix is maintained [98,99].

4 Objective of this work

Because of the promising potential of co-amorphous systems to stabilize the amorphous form of APIs to enhance their oral bioavailability, co-amorphous naproxen/indomethacin was chosen as a model system to further characterize these systems. This work covers the manufacturability of co-amorphous naproxen/indomethacin by spray-drying as well as the influence of the applied process parameters on the resulting sample properties. Furthermore, the effect of the cooling rate during the preparation by melt-quenching as well as that of the naproxen/indomethacin ratio on the resulting physical stability was investigated to further optimize the physical stability of this system. In a further study of this work, the system was finally optimized with regard to its long-term physical stability and its dissolution properties. Finally, four PLS regression models were developed to allow a simultaneous, diffractogram-based, multivariate quantification of co-amorphous naproxen/indomethacin, γ-indomethacin, α-indomethacin, and crystalline naproxen.

5 Results and Discussion

5.1 Preparation by spray-drying[1]

The process parameters pump feed level and inlet temperature were identified as the most critical parameters, as they would significantly impact the evaporation rate of acetone, which is important to prevent recrystallization during the drying process and to achieve a preferably amorphous product. The two process parameters were varied over the full possible technical range of the spray-dryer and the peristaltic pump to identify the optimal process conditions to obtain a maximally amorphous, dry and stable co-amorphous product. Each of the five process conditions was investigated in triplicate to evaluate the reproducibility of the resulting sample properties as a function of the process conditions. Acetone was used as solvent as in a preliminary study the highest solubility of NAP and IND was found with respect to other common organic solvents such as methanol, ethanol, isopropanol, n-hexane and diethyl ether.

[1] Parts of this chapter have been published as shown under 8.2 in the appendix.

5.1.1 **Characterization of the fresh samples**

XRPD analysis was performed to investigate the solid-state characteristics of the freshly spray-dried samples. In Fig. 3, one exemplary X-ray powder diffractogram for each combination of the process conditions and the diffractogram of REF are shown.

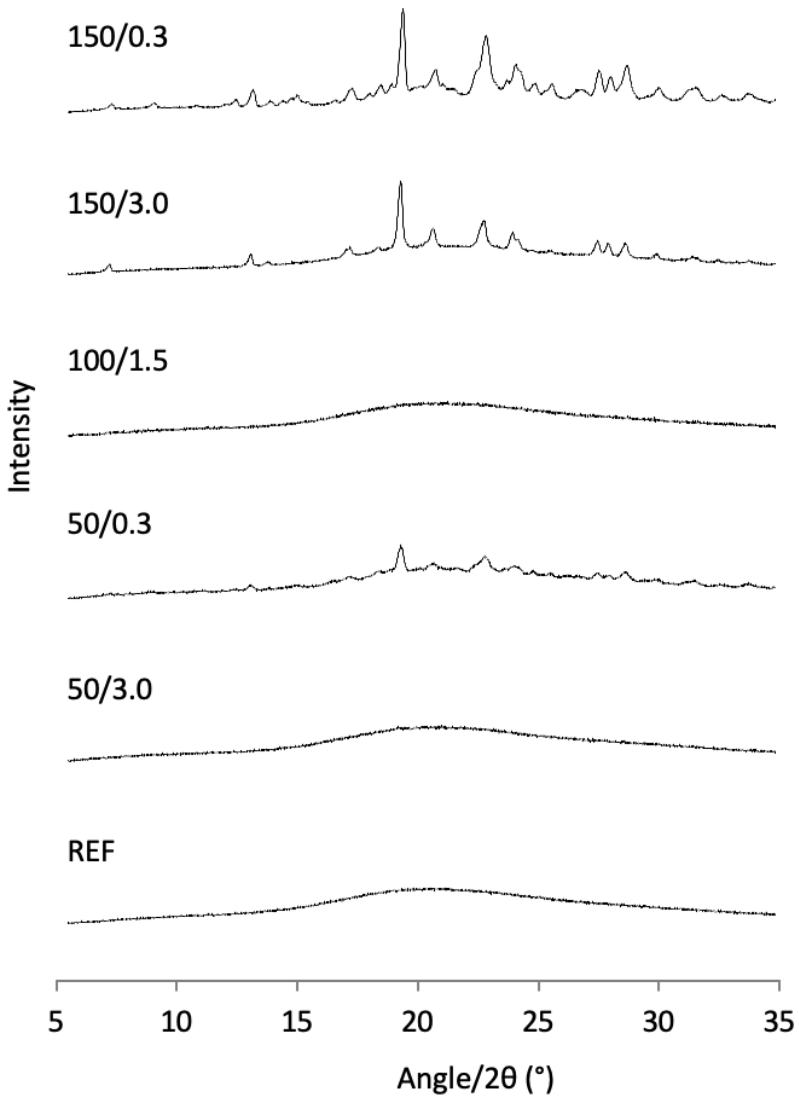

Fig. 3: Exemplary X-ray powder diffractograms of the unstored spray-dried samples for each combination of the process conditions and of REF.

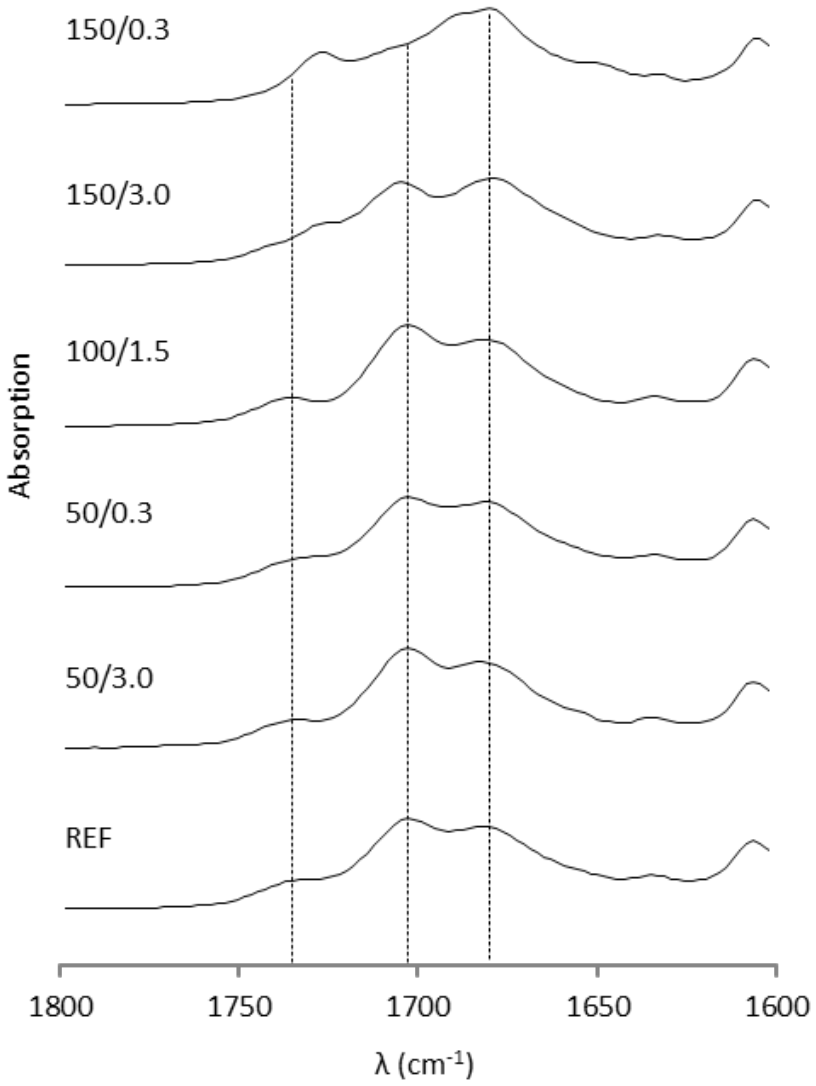

Fig. 4: Exemplary mean FTIR spectra of the unstored spray-dried samples for each combination of the process conditions and of REF.

The diffractograms for the 100/1.5 and 50/3.0 samples predominantly contain halo patterns, indicating the formation of an amorphous phase. In contrast, the diffractograms of the 150/0.3 and 150/3.0 samples show distinct peaks that indicate the presence of a crystalline fraction. In the 50/0.3 samples, the same diffractions were visible, albeit to a lower extent, indicating a largely but not completely amorphous product for this process conditions.

To further investigate the fresh samples in terms of their chemical information, FTIR analysis was performed. In Fig. 4, one exemplary spectrum for each combination of the process conditions and the spectrum of REF, which is in good agreement with the literature [65], are shown. The small peak at 1735 cm^{-1} represents the free carboxylic acid functions of naproxen and indomethacin being present in the co-amorphous phase. The band at 1703 cm^{-1} indicates

the interaction between NAP and IND within the formed heterodimers in the co-amorphous phase while the peak at 1680 cm^{-1} represents the benzoyl group of amorphous indomethacin [89,76]. The FTIR spectra of the 100/1.5, 50/3.0 and 50/0.3 samples are almost identical to that of REF indicating the formation of the desired co-amorphous phase. In contrast, the 150/0.3 and 150/3.0 samples showed deviations from the REF spectrum, especially regarding the smaller heterodimer peak at 1703 cm^{-1}, suggesting that these samples are not fully co-amorphous.

In summary, the FTIR data correlates with the results of the XRPD analysis. Samples with distinct recrystallization peaks in the diffractograms also showed deviations in the FTIR spectra compared to the fully co-amorphous REF sample.

To compare all freshly prepared, unstored samples in terms of their solid-state characteristics as a function of the applied process conditions, principal component analysis (PCA) was performed for the whole XRPD dataset. In the PCA scores plot (Fig. 5), PC-1 separates the diffractograms of the samples according to the applied process conditions and four clusters along the PC-1 axis can be identified.

To interpret the different locations of the diffractograms along PC-1, the respective PC-1 loadings plot is shown (Fig. 6). The diffraction signals in the positive part of the PC-1 loading can be assigned to peaks in the reference diffractograms of cNAP while the smaller peaks can be assigned to α-IND. The negative part of the PC-1 loading does not show any X-ray diffraction peaks, but a halo-like shape that is interrupted by the peaks in the positive part of PC-1. Therefore, PC-1 distinguishes the samples according to their amorphicity (negative PC-1 values, applicable to the 100 °C and 50 °C samples) or crystallinity (positive PC-1 values, applicable to the 150 °C samples), respectively. Interestingly, one of the diffractograms of the 150/3.0 samples is located in the negative part of the PC-1 scores plot and is therefore rather amorphous compared to the other two 150/3.0 samples. This observation suggests that this process condition, in contrast to the other four, is not suitable to obtain a reproducible outcome when co-spray drying NAP and IND. The PC-2 loadings plot reveals peak shifts along the °2θ axis, which do not seem to be related to processing conditions but result from variations in the sample positions during the XRPD measurements [105].

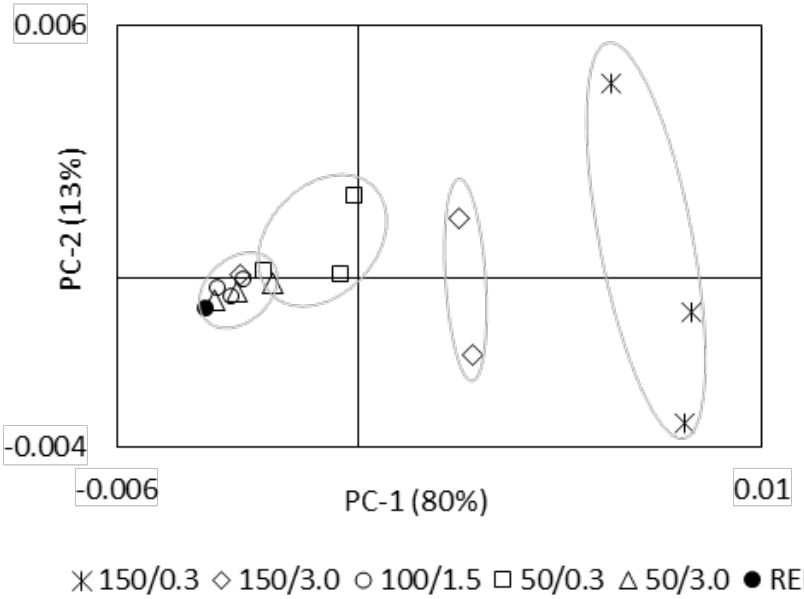

Fig. 5: PCA scores plot for the XRPD data set of the unstored spray-dried samples and REF. The different symbols represent the samples resulting from each combination of the process conditions.

PCA was also applied to the FTIR dataset as described before for the XRPD dataset [108]. In the FTIR PCA scores plot (Fig. 7), PC-1 separates the spectra according to the applied process conditions. In the positive part of the PC-1 loading (Fig. 7), four signals at 1727 cm^{-1}, 1687 cm^{-1}, 1679 cm^{-1} and 1648 cm^{-1} are identified. The distinct signal at 1727 cm^{-1} is assigned to the free carboxylic acid function in crystalline naproxen [65] while the other bands represent the benzoyl group (1687 cm^{-1}) and the two different hydrogen bonding patterns of the carboxylic acid functions (1679 cm^{-1} and 1648 m^{-1}) in crystalline α-IND, respectively [109].

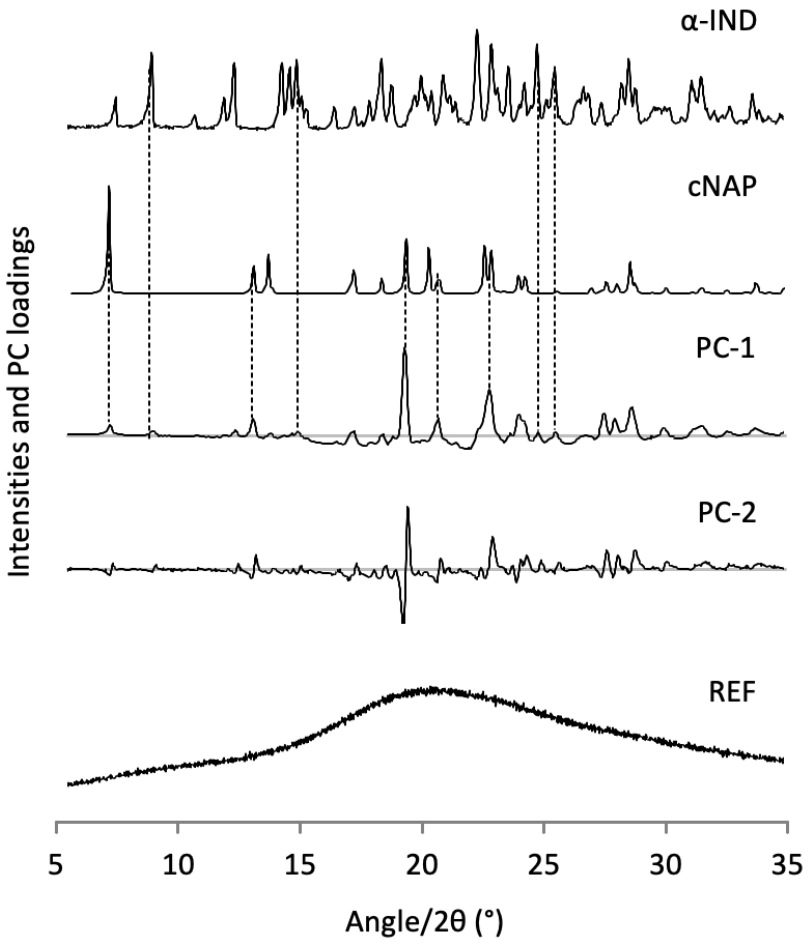

Fig. 6: PC-1 and PC-2 loadings plots for the XRPD dataset as well as reference diffractograms of α-IND, cNAP and REF. The different symbols represent the samples resulting from each combination of the process conditions.

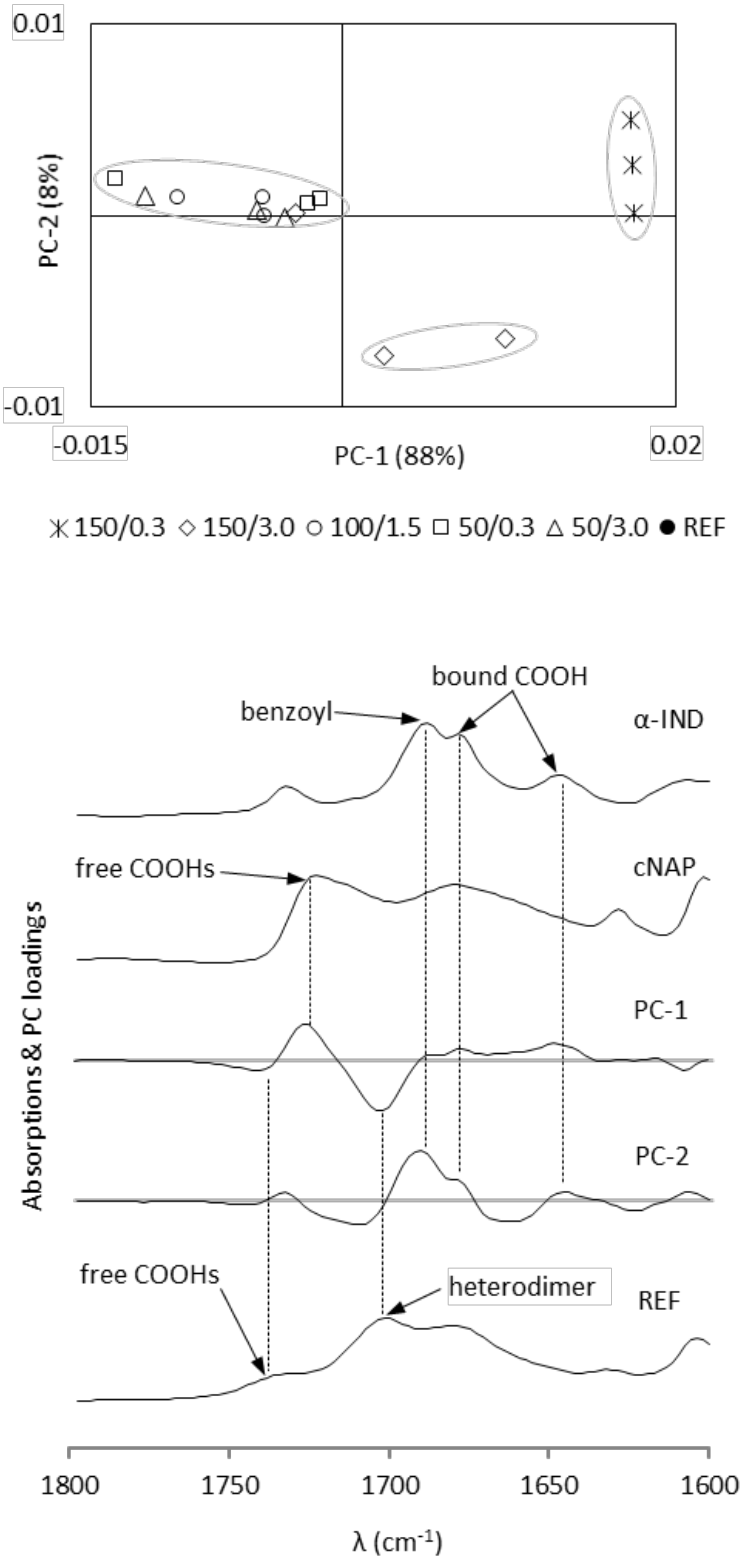

Fig. 7: PCA scores (top) and loadings plot (bottom) for the FTIR data set of the unstored spray-dried samples and REF.

In the negative part of the PC-1 loading, two bands at 1735 cm^{-1} (free COOHs) and 1703 cm^{-1} (heterodimer) are found, representing the co-amorphous phase [65]. As observed by XRPD analysis, PC-1 distinguishes between the samples according to their co-amorphicity (negative PC-1 values, applicable to the 100 °C and 50 °C samples) or crystallinity (positive PC-1 values, applicable to the 150 °C samples), respectively. In accordance with the XRPD data, one of the diffractograms of the 150/3.0 samples is located apart from the rest. As the shape of the PC-2 loading is almost identical to that of the α-IND spectrum, PC-2 indicates that two of the three fresh 150/0.3 samples with high PC-2 values contain comparably more alpha-IND.

The PCAs of the XRPD and the FTIR datasets led to comparable results. Samples with mainly halo patterns in the diffractograms also show pronounced FTIR bands for the co-amorphous system. In contrast, samples with distinct diffraction peaks in the diffractograms show smaller FTIR bands for the co-amorphous system.

5.1.2 Characterization of the stored samples

5.1.2.1 Modes of indomethacin and naproxen recrystallization

All spray-dried samples were stored for up to 28 d and analyzed by XRPD and FTIR in order to investigate their recrystallization behavior. In Fig. 8, the resulting PCA scores plot for the complete XRPD data set is shown. The different colours highlight the samples resulting from each combination of process conditions, while the different shapes represent the different storage time periods (circles = 0 d, triangles = 7 d, square = 14 d, diamond = 28 d). In Fig. 9, the respective PC-1 and PC-2 loadings plots are shown. In the positive part of PC-1, diffraction signals according to the α-IND and cNAP references are visible while in the positive part of PC-2 intensities of γ-IND and cNAP are found (dashed lines). In contrast, in the negative parts of the PC-1 and PC-2 loadings, no sharp X-ray peaks but halo like shapes are visible.

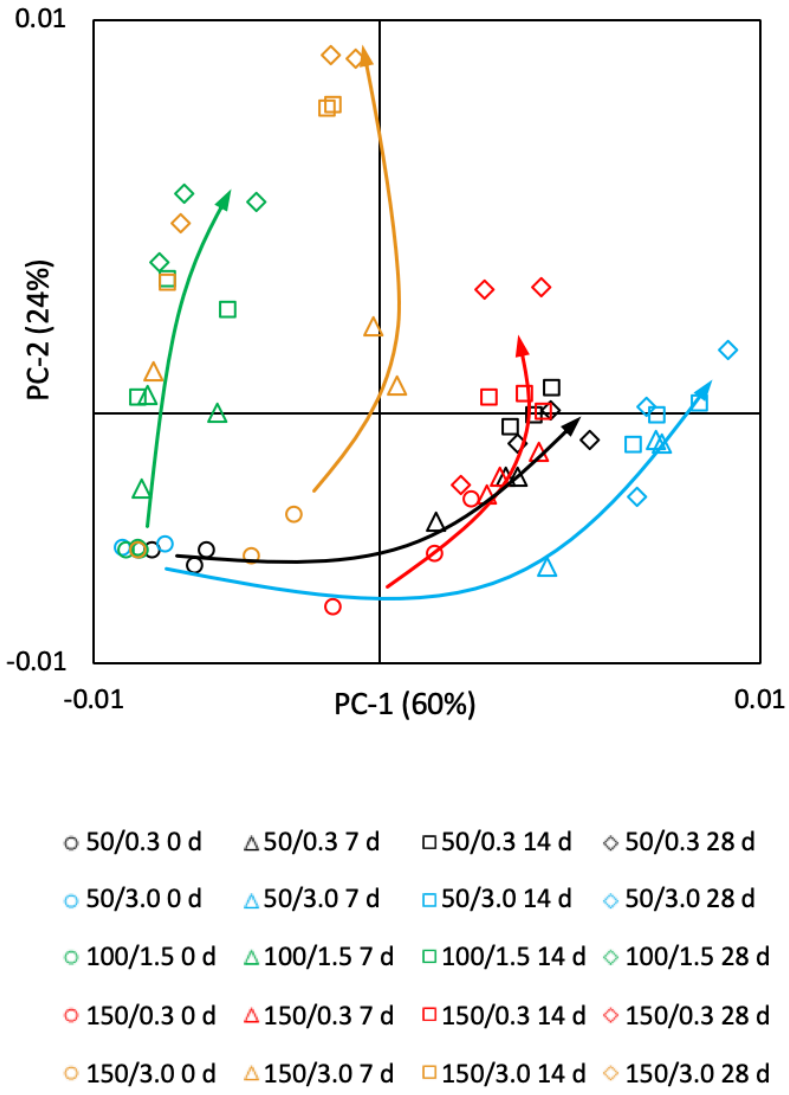

Fig. 8: PCA scores plot for the XRPD data set of the stored and unstored spray-dried samples. The colors represent the samples resulting from each combination of the process conditions, while the symbols represent the different storage time periods.

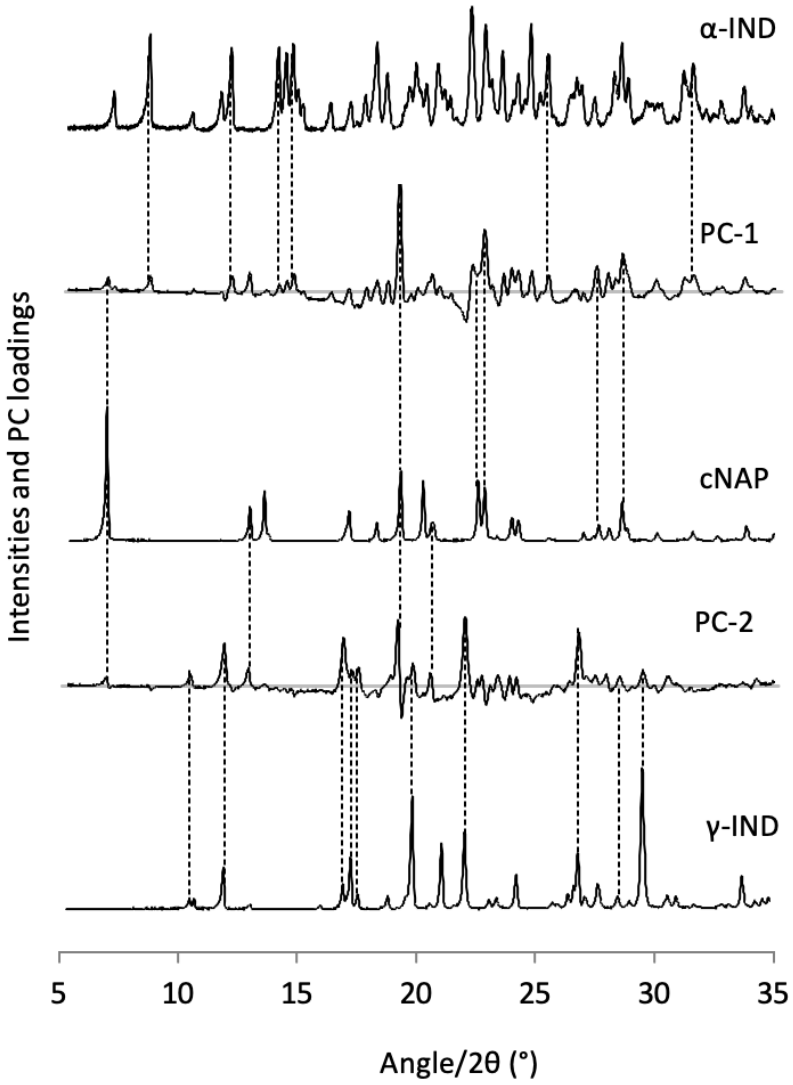

Fig. 9: PC-1 and PC-2 loadings plots for the XRPD data set as well as reference diffractograms of α-IND, γ-IND and cNAP.

The stored 150/0.3 samples cluster towards positive PC-1 scores and towards slightly positive PC-2 scores (Fig. 8). Therefore, recrystallization occurs predominantly under formation of cNAP and α-IND within these samples. For the 150/3.0 samples the situation is different: stored samples are located at PC-1 scores close to zero and at positive PC-2 scores. Thus, cNAP and γ-IND are present in these samples. This is similar to the 100/1.5 samples, which change their positions towards positive PC-2 scores, while the PC-1 scores are consistently negative. This indicates that recrystallization under formation of cNAP and γ-IND occurs, but slower and less distinct compared to the 150/3.0 samples. For the process conditions 50/0.3 and 50/3.0, the 7 d stored samples cluster already far away from the freshly prepared samples at high positive PC-1 scores and PC-2 scores close to zero. Therefore, these samples recrystallize similar to the 150/0.3 samples, but significantly faster, under formation of predominantly cNAP and α-IND. Obviously, the 150/0.3, 50/0.3 and 50/3.0 samples recrystallize under formation of cNAP and α-IND and follow a different recrystallization mode than the 100/1.5 and 150/3.0 samples, which recrystallize under formation of cNAP and γ-IND.

The diffraction signals that are found in the respective positive and negative parts of the PC-1 and PC-2 loadings as well as the stored samples that cluster in the corresponding areas are summarized in Table 2.

Table 2: Diffraction signals present in the PC loadings plots and corresponding stored samples that cluster in the respective parts of the scores plot. Weak signals in the loadings plot are shown in brackets.

	PC-1	Stored Samples	PC-2	Stored Samples
Positive	α-IND, cNAP	50/3.0, 50/0.3, 150/0.3	γ-IND, cNAP	150/3.0, 100/1.5, 150/0.3
Negative	Halo, (γ-IND)	100/1.5	Halo, (α-IND)	-

For comparison, PCA was also performed with the FTIR dataset of the stored samples. In Fig. 10, the PCA scores plot for the complete FTIR data set is shown. Again, the different colours highlight the samples resulting from each combination of process conditions, while the different shapes represent the different storage time periods.

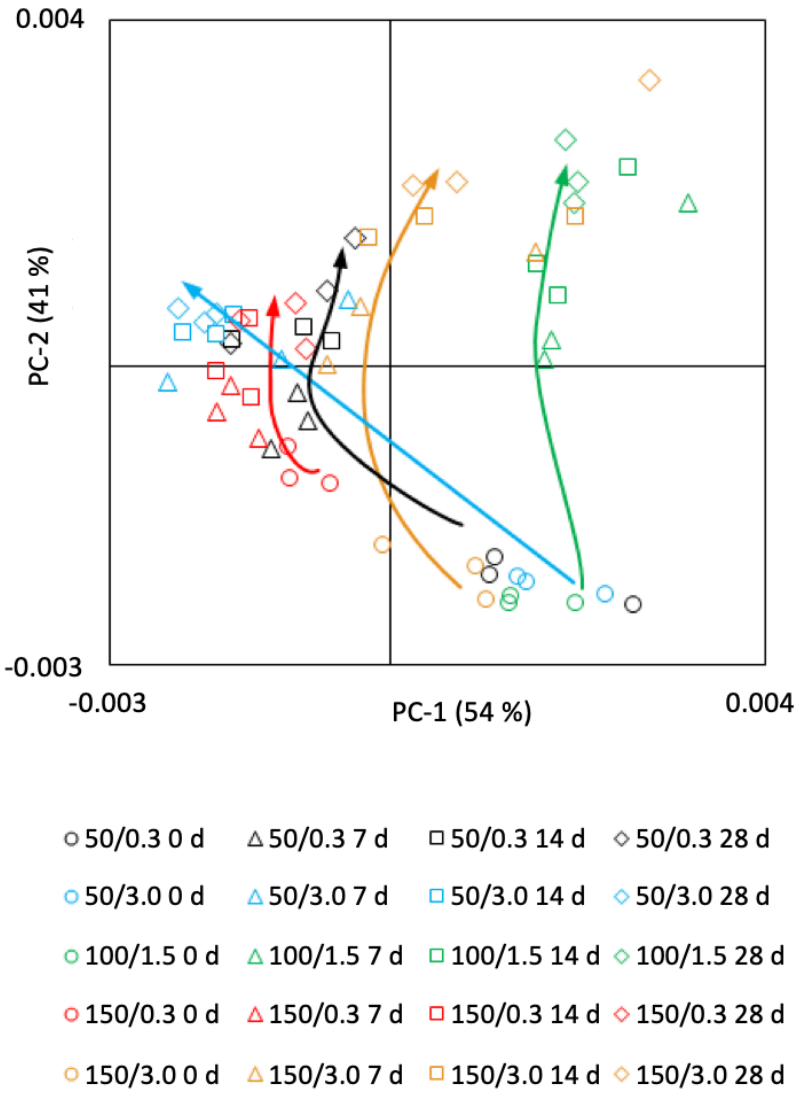

Fig. 10: PCA scores plot for the FTIR data set of the stored and unstored spray-dried samples. The colors represent the samples resulting from each combination of the process conditions, while the symbols represent the different storage time periods.

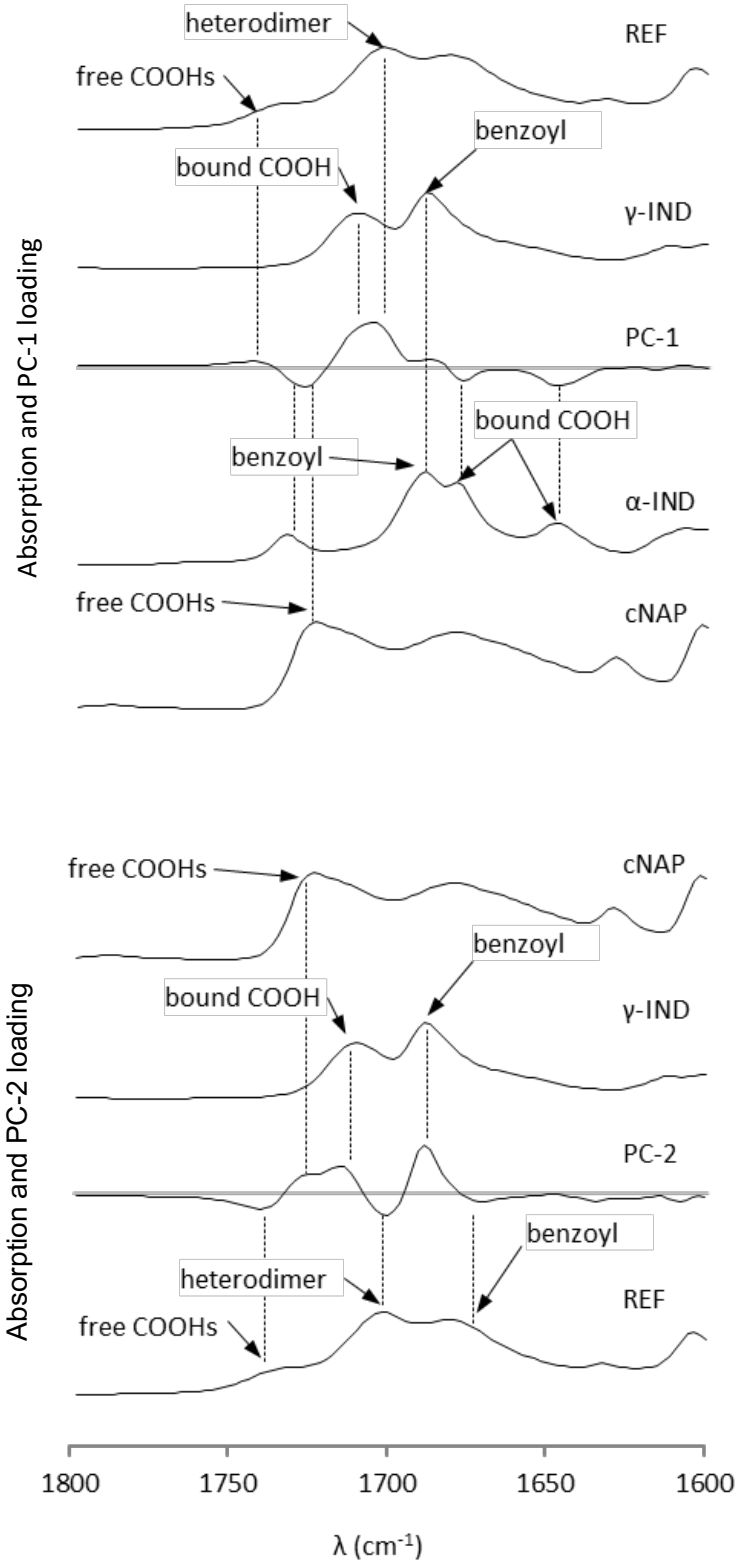

Fig. 11: PC-1 (top) and PC-2 (bottom) loadings plot for the FTIR data set as well as reference spectra of α-IND, γ-IND, cNAP and REF.

In Fig. 11, the respective PC-1 and PC-2 loadings plots are shown. In the negative part of PC-1, FTIR signals according to the α-IND and cNAP reference spectra are visible while in the positive part of PC-2 bands of γ-IND and cNAP are found (dashed lines). In contrast, in the positive part of PC-1 and the negative part of PC-2, predominantly FTIR signals REF are found. PC-1 separates the stored samples according to the polymorph of indomethacin that is formed (Fig. 10). Samples that cluster in the positive part of PC-1 (150/3.0 and 100/1.5) recrystallize predominantly under formation of γ-IND while samples that cluster in the negative part (150/0.3, 50/3.0 and 50/0.3) form predominantly α-IND during storage. Therefore, the FTIR dataset reveals the same result as the XRPD dataset regarding the two different recrystallization modes. PC-2 represents a measure of the remaining amorphousness of the samples as positive scores are correlated with the spectra of cNAP and γ-IND while negative scores are related to FTIR bands that are found in REF.

The FTIR signals that are found in the respective positive and negative parts of the PC-1 and PC-2 loadings as well as the stored samples that cluster in the corresponding areas are summarized in Table 3.

Table 3: FTIR signals present in the PC loadings plots of the stored samples and the corresponding stored samples that cluster in the respective parts of the scores plot.

	PC-1	Stored Samples	PC-2	Stored Samples
Positive	γ-IND, REF	100/1.5, 150/3.0	γ-IND, cNAP	100/1.5, 150/3.0, 50/0.3, 150/0.3, 50/3.0
Negative	α-IND, cNAP	50/3.0, 150/0.3, 50/0.3	REF	-

5.1.2.2 **Recrystallization**

- **Quantification of the co-amorphous phase**

To monitor the solid state phase composition of the spray-dried samples during storage, the RIR method [103] and a calibration set (7.1.5) were used. For the calibration samples with predefined molar fractions of α-IND, γ-IND, cNAP and co-amorphous NAP-IND, the intensity under the Bragg peaks (I_{Halo}, representing the co-amorphous portion) in relation to the allover intensity of the respective diffractogram (I_{Total}) was determined first (Equation 10). For this purpose, the background determination function in the Highscore Plus software (ver. 2.2, PANalytical, Almelo, The Netherlands) was used.

$$RIR_{Halo} = \frac{I_{Halo}}{I_{Total}} \qquad \text{Equation 10}$$

The respective true fractions of the co-amorphous phase in the calibration samples was correlated with RIR_{Halo} and good correlation coefficients were found (Fig. 13).

- **Quantification of the crystalline phases**

The intensity under the Bragg peaks was now subtracted from all diffractograms to obtain only the intensities that result from the Bragg peaks, which represent the crystalline portion of the samples. The respective true fractions of α-IND, γ-IND and cNAP in the calibration samples were then correlated with the corresponding non-overlapping peak areas of the respective compounds in the residual diffractograms according to Fig. 12. Good correlation coefficients were obtained for all three fractions (Fig. 13).

- **Recrystallization rates**

In Fig. 14, the mean α-IND, γ-IND, cNAP and amorphous fractions are plotted versus their storage time periods for each combination of the process conditions. Summation of the four independently calculated fractions results in a total of 93.9 % ± 6.5 % and shows that the RIR method delivers reliable results.

After 28 d of storage, the 100/1.5 samples turned out to be least crystalline and the 50/3.0 samples most crystalline. The other samples show intermediate physical stabilities with an amorphous fraction between 44 % and 50 %. Interestingly, the 150/0.3 samples show the lowest 28 days-recrystallization rate although theses samples are the most crystalline directly after preparation. The differences in the sample amorphicities directly after preparation may be explained by the thermal stress, which was applied to the product during the spray-drying process. After completion of the drying process, the dried product leaves the spraying tower at the outlet temperature. Due to the relatively low glass transition temperature of the system of about 25 °C, it was not possible to decrease the outlet temperatures below the Tg of the system [65], even if the inlet temperature was set to its respective minimum and the PFR was set to its maximum (Table 7 in 7.1.1). Thus, while entering the cyclone, the dried product was present in the supercooled melt state and stuck mostly to the cyclone wall before centrifugal forces were able to remove the product out of the gas stream [110,101]. Obviously, high inlet temperatures and low PFRs increase the thermal stress applied to the product before the process ends (Table 7 in 7.1.1). This thermal stress is maximal for the 150/0.3 samples and intermediate for the 150/3.0 samples and leads to an accelerated sample recrystallization,

which explains the increased crystallinities of the respective fresh 150/0.3 samples. In contrast, processing at the lower temperatures resulted in initially less crystalline products.

A maximally dry product is desired during preparation of amorphous solids because any kind of solvent affects the physical stability of these systems by decreasing the glass transition temperature and enhancing recrystallization [111]. Therefore, the performed experiments were not limited to process conditions with low thermal stress as these low thermal stress conditions would lead to considerable amounts of solvent residue in the samples [112]. Indeed, the 50 °C samples contain the highest acetone residues as confirmed by TGA (Table 4).

Table 4: Overview of the acetone residue in the fresh samples after spray-drying.

Sample name	150/0.3	150/3.0	100/1.5	50/0.3	50/3.0
Mean acetone residue (%)	0.26 ± 0.06	0.59 ± 0.03	0.89 ± 0.37	2.10 ± 0.14	2.36 ± 0.12

The fast recrystallization of the 50 °C samples may be explained by the presence of about 2 % of acetone in these samples (Table 4). In comparison, recrystallization proceeded slower with the center point samples, probably resulting from their lower content of acetone (Table 4). The 150/3.0 samples recrystallize faster than the 100/1.5 samples although the acetone residues are slightly lower. Therefore, the increased recrystallization rates of the 150/3.0 samples are likely to be caused by the higher thermal stress during the process in combination with the acetone residual. The thermal stress is even higher for the 150/0.3 samples, which leads to a lower initial sample amorphicity but also to lower acetone residues, which may explain the slower recrystallization rate compared to the 150/3.0 samples.

5.1.2.3 **Recrystallization modes**

The two different recrystallization modes that were found during PCA analysis of the XRPD and FTIR datasets are confirmed by RIR quantification: the 150/0.3, 50/0.3 and 50/3.0 samples recrystallize predominantly under formation of the α-polymorph of IND while the other samples form γ-IND during storage (Fig. 14). The observation that recrystallization of the α-IND polymorph occurs in the 150/0.3, 50/0.3 and 50/3.0 samples is in agreement with the literature, reporting that the α-IND polymorph preferably recrystallizes at higher temperatures [113,114] or when solvent is present [111].

As the NAP and IND recrystallization appears to be related, the mean molar $F_{\alpha+\gamma}$ fractions of the initially X-ray amorphous samples (100/1.5, 50/0.3 and 50/3.0) are plotted versus the mean molar F_{cNAP} fractions in Fig. 15. The coefficient of determination (R^2 = 0.9052) indicates a distinct relationship between the IND and NAP recrystallization and therefore supports the

theory of formation of drug-drug heterodimers in the co-amorphous phase and a simultaneous recrystallization of both drugs when the interactions in the heterodimer break upon storage [65].

5.1.3 **Conclusion**

In conclusion, the preparation of co-amorphous naproxen/indomethacin by spray-drying was successful depending of the applied process conditions despite the relatively low glass transition temperature of the co-amorphous system. The latter presented a challenge regarding the product retrieval because of the systems' sticking to the cyclone wall. It was shown that the process conditions inlet temperature and pump feed rate had a major influence on the initial sample crystallinity and the recrystallization behavior. The recrystallization rate and mode were dependent on the thermal stress that was applied to the samples during the spray-drying process and the remaining amount of solvent residue in the samples. Furthermore, for the initially amorphous samples it was found that recrystallization of the two compounds proceeds in a strongly related manner. Spray-drying therefore presents a useful alternative to prepare co-amorphous systems in case that other manufacturing methods such as melt-quenching or mechanical activation cannot provide satisfying results in terms of thermal degradation or incomplete amorphisation. Furthermore, the spray-drying process offers the opportunity for up-scaling to enable manufacturing of co-amorphous systems in more significant quantities.

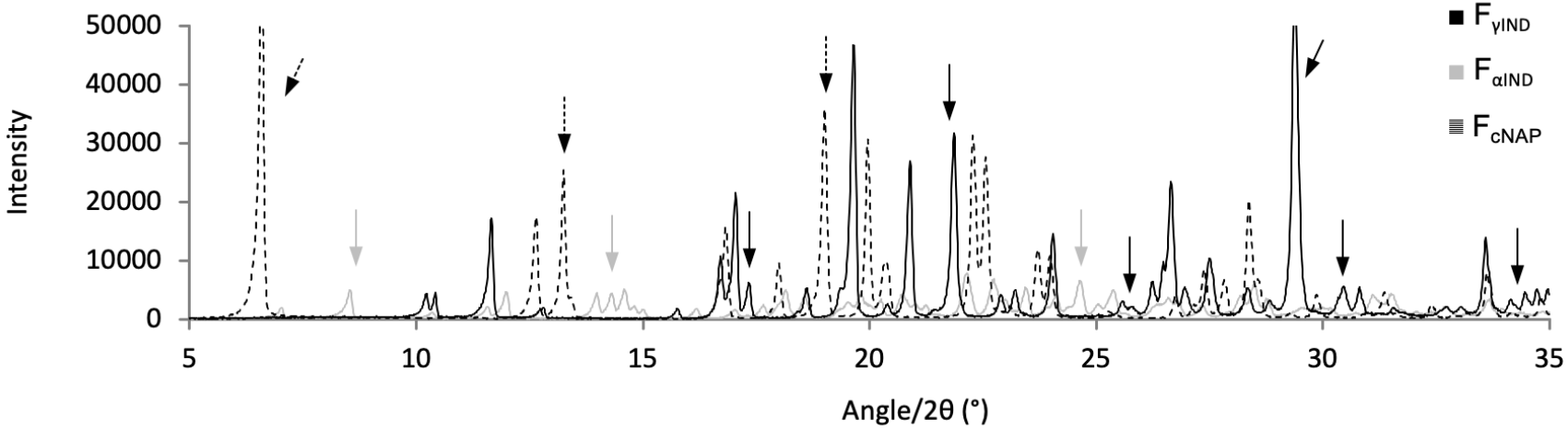

Fig. 12: Selected non-overlapping scatter angle areas of the diffractograms for construction of the RIR calibrations for, α-IND (grey), γ-IND (black) and cNAP (dashed).

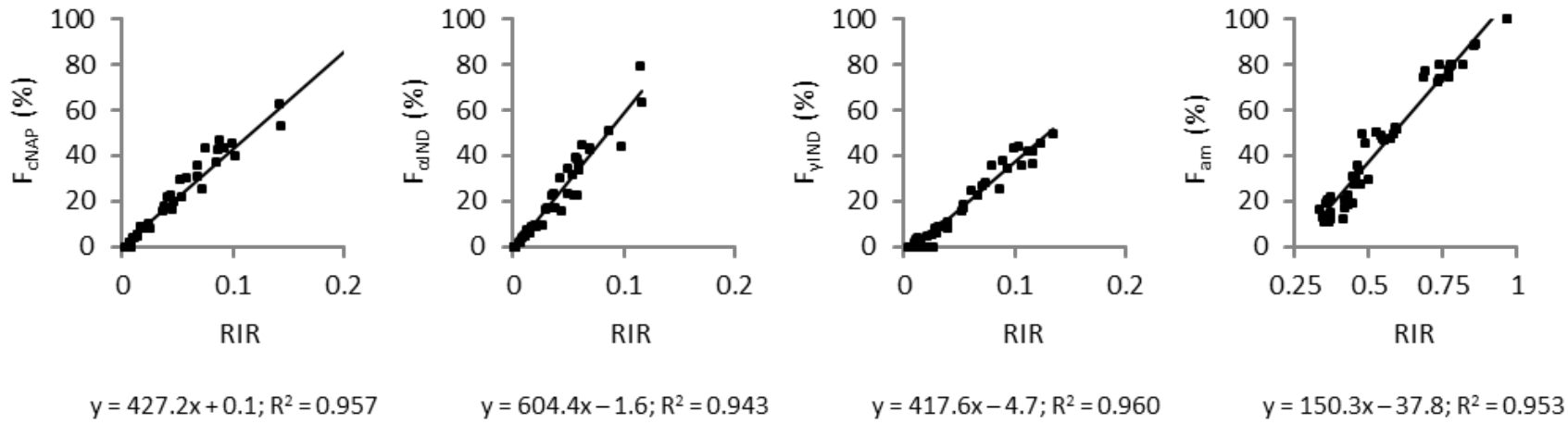

Fig. 13: Correlation of the true α-IND, γ-IND, cNAP and amorphous (F_{am}) fractions versus their corresponding relative intensity ratios (RIR) in the diffractograms.

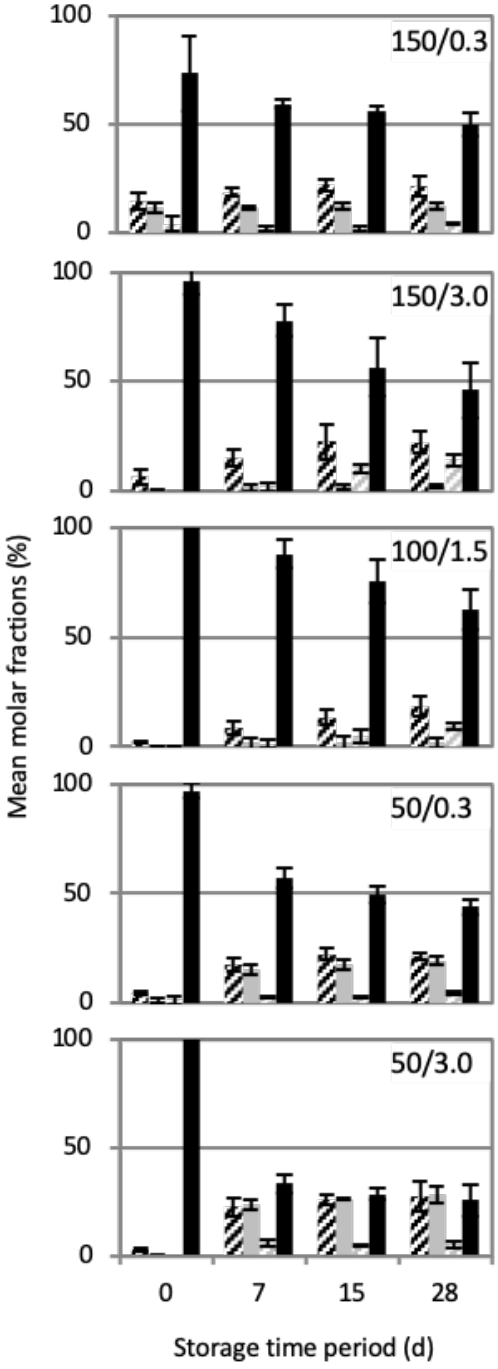

Fig. 14: Mean molar fractions ± SD (n = 3) of α-IND (grey), γ-IND (grey dashed), cNAP (black dashed) and the amorphous phase (black) for each combination of the process conditions.

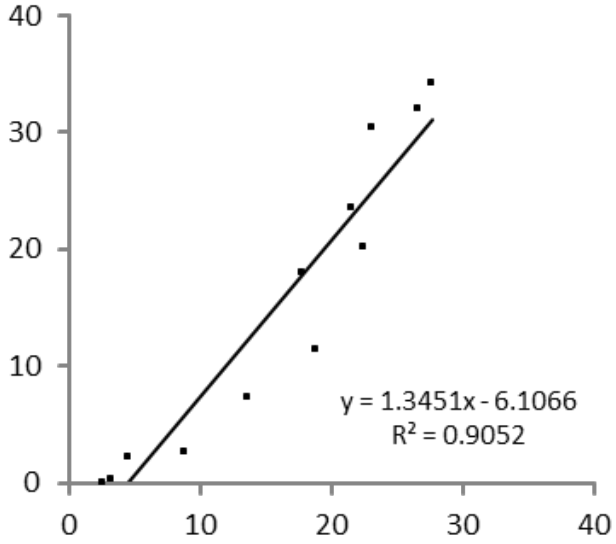

Fig. 15: Correlation of the sum of the mean α-IND plus mean γ-IND fractions ($F_{\alpha+\gamma}$) versus the mean cNAP fractions (F_{cNAP}) for initially fully amorphous samples.

5.2 **Dependence of the physical stability on the cooling rate and blend ratio**[2]

5.2.1 **Influence of the cooling rate on the physical stability**

To study the influence of the cooling rate on the physical stability of equimolar NAP/IND, three different cooling rates (FC, IC, SC) were investigated. Karl Fischer and DSC analysis were performed on the freshly prepared samples and revealed similar water contents and glass transition temperatures (Table 5), which were both not significantly different ($p > 0.05$).

Table 5: Mean water contents and glass transition temperatures ± SD (n = 3) of unstored FC, IC and SC samples

Samples	FC	IC	SC
Water content (%)	0.37 ± 0.16	0.78 ± 0.14	0.62 ± 0.28
Glass transition temperature (°C)	31.5 ± 1.3	26.7 ± 0.6	30.7 ± 4.7

The obtained XRPD data were evaluated by principal component analysis (PCA). In Fig. 16, the corresponding mean PC-1 scores ± SD (n = 3) are plotted versus the storage time periods of the differently prepared samples. For all storage time periods, the PC-1 scores of the FC

[2] Parts of this chapter have been published as shown under 8.2 in the appendix.

samples and the corresponding standard deviations are higher compared to the IC and SC samples, especially after 300 days of storage.

To interpret the PC-1 scores, the PC-1 loadings plot together with the reference diffractogram of γ-IND and cNAP is shown in Fig. 16. All peak signals in the positive part of the PC-1 loading are assignable to γ-IND or cNAP, while no peak signals but a halo shape is visible in the negative part of the PC-1 loading. Consequently, all samples recrystallized under formation of γ-IND and cNAP and the FC samples recrystallized faster than the SC and IC samples. In Fig. 17, one exemplary Savitzky-Golay smoothed diffractogram for each cooling method after 300 days of storage is shown for comparison. It is obvious, that the diffractogram of the IC samples includes less distinct diffraction peaks compared to the diffractograms of the SC and FC samples, which confirms the results of the PCA.

To verify the results obtained from the XRPD dataset, FTIR analysis was performed, and in Fig. 18, one exemplary spectrum of the differently cooled samples, stored for 300 days, is shown. The peaks at 1689 cm^{-1} (benzoyl function in γ-IND), 1714 cm^{-1} (bound COOH in γ-IND) and 1725 cm^{-1} (free COOHs in cNAP) are most pronounced with the FC samples and less distinct for the IC and SC samples. Therefore, the FTIR data confirms the results of the XRPD data: the FC samples are physically less stable than the IC and SC samples and recrystallization proceeds under formation of γ-IND and cNAP.

To quantify the total crystalline fraction F_{cryst} of the differently cooled samples during storage, the RIR method and a calibration function (□) were used. In Fig. 19, the mean total crystalline fractions F_{cryst} ± SD (n = 3) of the samples are plotted versus the storage time periods and shows that FC leads to samples that are 0.48 ± 0.28 crystalline after 300 d of storage, in contrast to 0.15 ± 0.03 (IC samples) and 0.20 ± 0.01 (SC samples).

These results are in good agreement with the PCA data presented in Fig. 16 and confirm that the temperature program plays a major role for the physical stability of co-amorphous NAP/IND. Surprisingly, FC leads to a significantly less stable product, which in addition recrystallized in a less reproducible manner. This recrystallization behavior might be caused by mechanical stress that is applied to the product during the fast temperature decrease of the samples from 170 °C to -196 °C within seconds [22]. Moreover, SC only slightly increases the recrystallization rate of co-amorphous NAP/IND compared to IC. This finding is surprising, as it has previously been reported that the preparation of amorphous materials by slow cooling leads to physically less stable materials, e.g. with plain amorphous indomethacin [115]. Therefore, the optimal cooling rate for the preparation of co-amorphous NAP/IND is neither maximal nor minimal but intermediate.

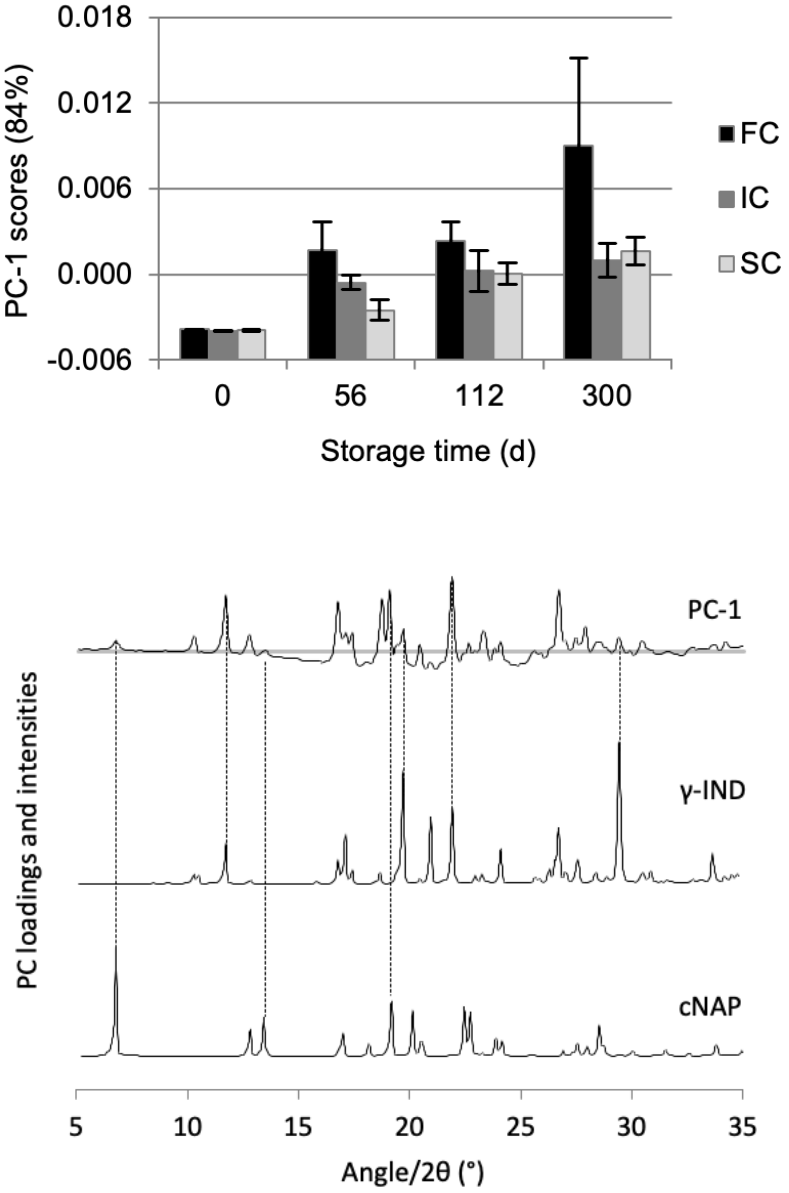

Fig. 16: Mean PC-1 scores ± SD (n = 3) of the differently cooled NAP/IND samples plotted versus the storage time (top). Corresponding PC-1 loadings plot as well as reference diffractograms of γ-IND and cNAP (bottom).

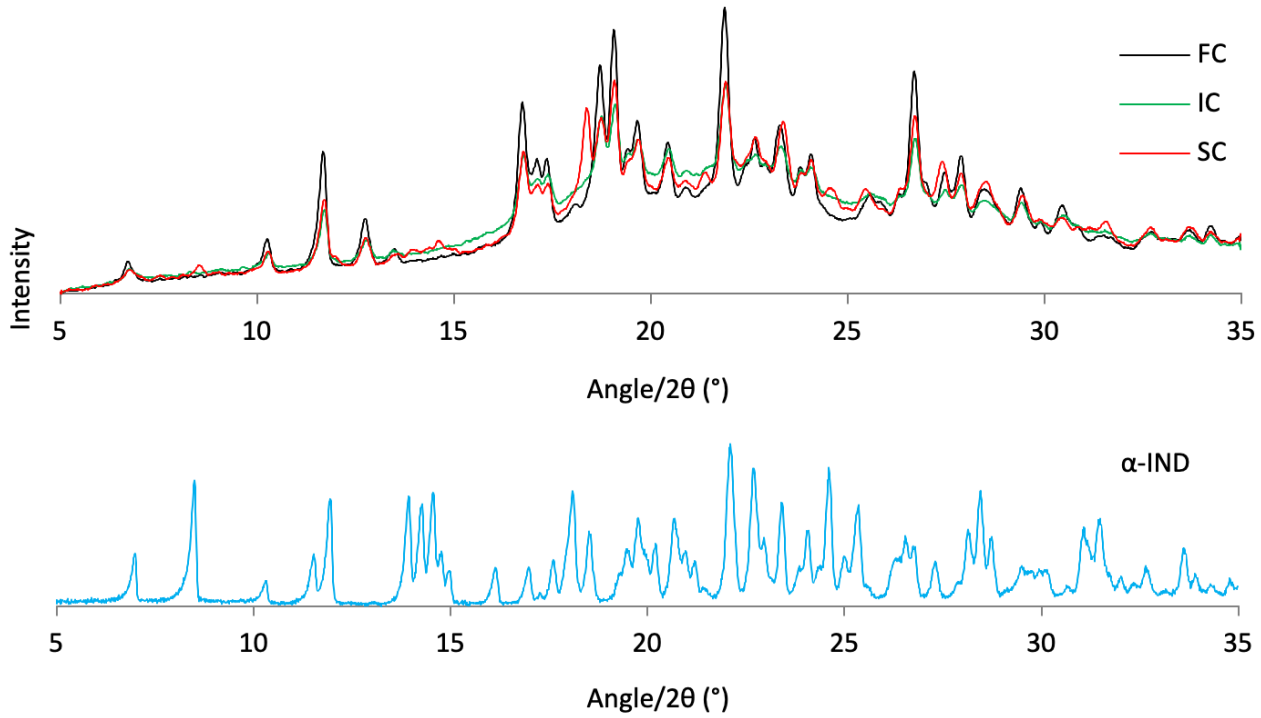

Fig. 17: Exemplary Savitzky-Golay smoothed diffractograms of the FC, IC and SC samples, stored for 300 d, and for α-IND

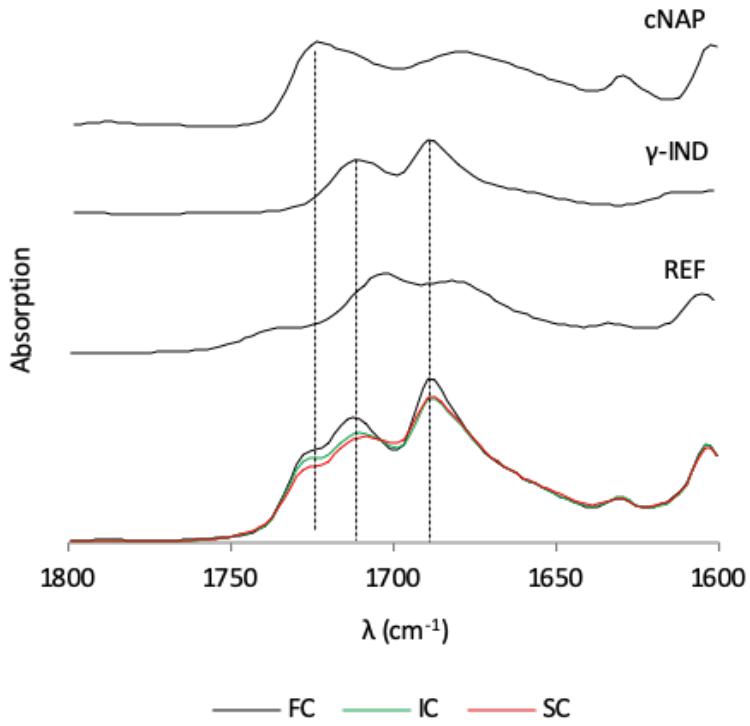

Fig. 18: Exemplary FTIR spectra of the FC, IC and SC samples, stored for 300 d, and reference spectra of cNAP, γ-IND and unstored equimolar co-amorphous NAP/IND (REF).

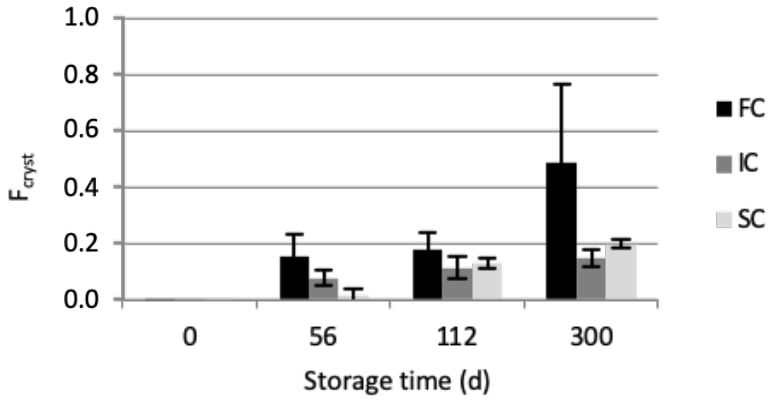

Fig. 19: Mean total crystalline fractions (F_{Cryst}) ± SD (n = 3) of the FC, IC and SC samples plotted versus the storage time.

5.2.2 **Influence of the blend ratio on the physical stability**

Because IC led to the physically most stable samples after 300 days of storage compared to SC and FC, IC was also performed in the second part of the study. Here it was the aim to investigate the influence of the phase composition on the resulting physical stability of the co-

amorphous system. Therefore, co-amorphous NAP/IND was prepared in ten different blend ratios by IC. Subsequently, the samples were stored and characterized by XRPD and FTIR to evaluate their physical stabilities.

5.2.3 **Unstored samples**

In Fig. 20, one exemplary diffractogram is shown for each of the unstored samples with increasing NMFs ranging from 0.1 to 0.7. All diffractograms comprise exclusively halo signals and thus, the samples are fully amorphous. In contrast, the 0.8 and 0.9 samples show distinct peak intensities for cNAP, revealing that these samples already recrystallized to a significant level. This is in accordance with observations made during sample preparation in both samples, i.e. a crystalline phase was formed at 170 °C after the samples were initially fully molten. In Fig. 21, one exemplary FTIR spectrum of each of the unstored samples with NMFs between 0.1 and 0.7 is shown. The bands around 1735 cm^{-1} (free COOH groups), 1701 - 1705 cm^{-1} (NAP/IND interaction) and 1678 - 1684 cm^{-1} (benzoyl function in IND) represent the different carbonyl functions present in co-amorphous NAP/IND [65]. The shift of the NAP/IND interaction band from 1705 to 1701 cm^{-1} with increasing NMF indicates that the location of the peak depends on the NMF in the co-amorphous phase. Furthermore, with increasing NMF, the IND benzoyl band at 1678 cm^{-1} [109] decreases and also slightly shifts to higher wavenumbers of 1684 cm^{-1}, which indicates that the benzoyl group is also involved in the interaction between NAP and IND. In contrast, the exemplary FTIR spectra of the 0.8 and 0.9 samples in Fig. 21 show a distinct decrease of the NAP/IND interaction band (1701-1705 cm^{-1}) and an increase at 1725 cm^{-1} (free COOHs in cNAP) and 1680 cm^{-1} (bound COOHs in cNAP), which both represent absorption bands present in cNAP [65]. Therefore, the XRPD and FTIR data are consistent: co-amorphous NAP/IND is formed with NMFs between 0.1 and 0.7, while the samples with NMFs of 0.8 and 0.9 recrystallized under formation of only cNAP.

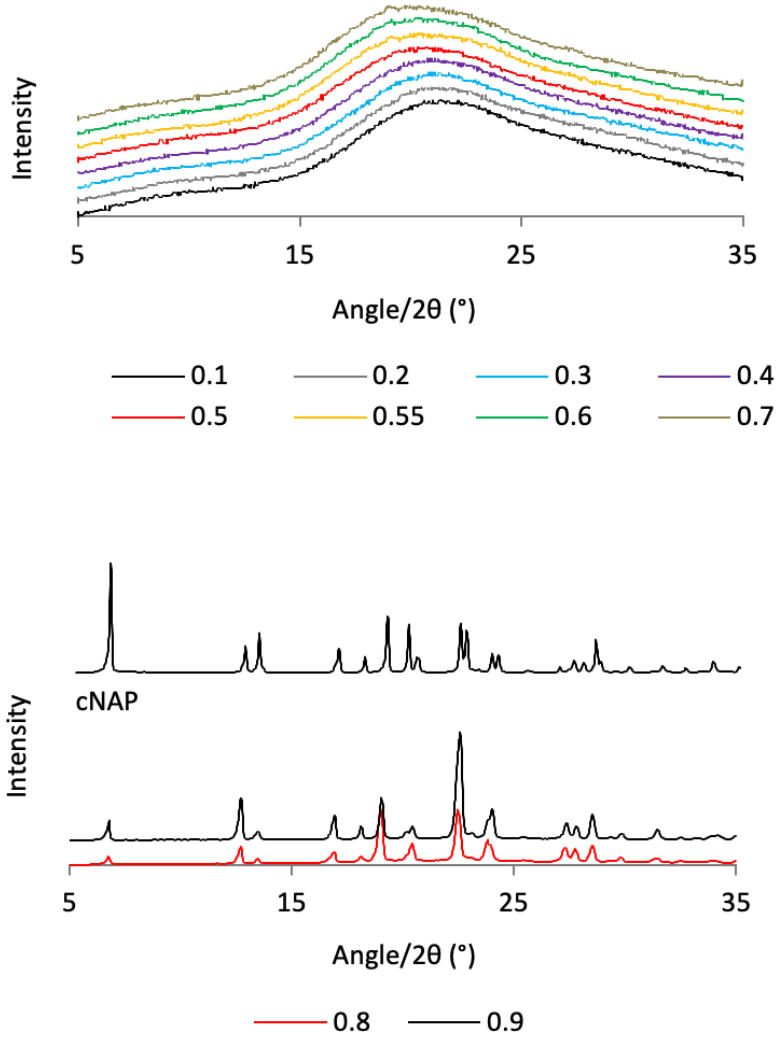

Fig. 20: Exemplary diffractogram of each of the unstored samples with NMFs between 0.10 and 0.70 (top). Exemplary diffractogram of the unstored samples with NMFs of 0.80 and 0.90 and reference diffractogram of cNAP (bottom).

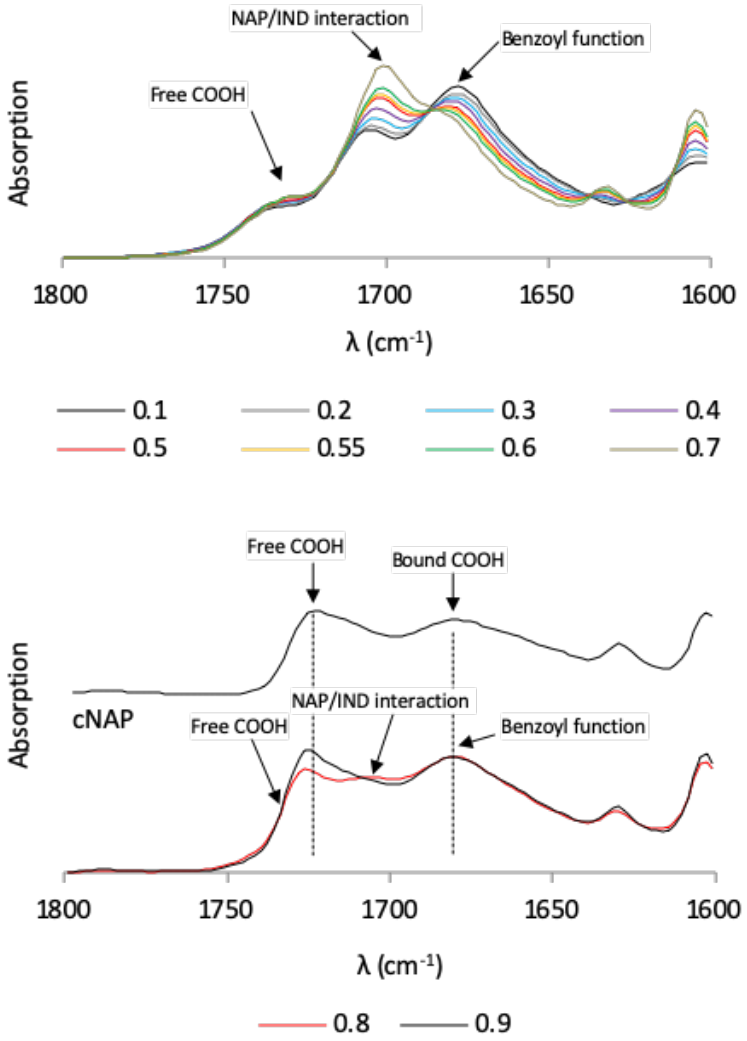

Fig. 21: Exemplary FTIR spectrum of each of the unstored samples with NMFs between 0.10 and 0.70 (top). Exemplary spectrum of the unstored samples with NMFs of 0.80 and 0.90 and reference diffractogram of cNAP (bottom).

DSC reveals only single-phase glass transition temperatures of the 0.1 - 0.7 samples (Fig. 22) comparable to those reported by Löbmann et al. [65], which indicates that single-phase co-amorphous systems were obtained.

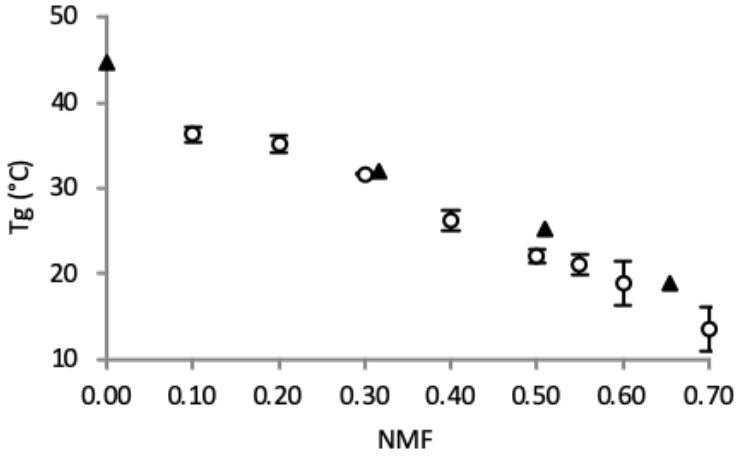

Fig. 22: Mean glass transition temperatures ± SD (n = 3) of the unstored initially fully amorphous samples (circles) plotted versus the naproxen molar fraction (NMF). For comparison, the mean glass transition temperatures reported by Löbmann et al. are shown (black triangles).

Moreover, the samples only contain low but comparable amounts of water (Table 6) and therefore, the influence of the water content on the physical stability of the samples is expected to be negligible.

Table 6: Mean water contents ± SD (n = 3) of the unstored samples with NMFs between 0.1 and 0.7.

NMF	Water content (%)
0.1	0.72 ± 0.17
0.2	0.91 ± 0.11
0.3	1.10 ± 0.13
0.4	1.10 ± 0.18
0.5	0.90 ± 0.17
0.55	0.85 ± 0.09
0.6	0.82 ± 0.03
0.7	0.77 ± 0.11

5.2.4 **Stored samples**

After 56 and 112 days of storage, all prepared samples were analyzed by XRPD and FTIR to assess their physical stability. All resulting diffractograms and spectra were evaluated by PCA. According to the resulting PCA scores plot for the XRPD dataset (Fig. 23), all stored samples with NMFs between 0.1 and 0.6 are mainly described by PC-1 while increasing PC-1 scores correlate with decreasing NMFs. In contrast, the 0.7 samples are mainly described by PC-2.

In the positive part of the PC-1 loadings plot (Fig. 23), exclusively diffraction signals according to the γ-IND reference diffractogram are found, while in the negative part predominantly halo signals are present. Therefore, PC-1 separates the samples according to their γ-IND crystallinity (high scores) and amorphicity (low scores). In the positive part of the PC-2 loadings plot predominantly diffraction intensities of cNAP are found, while a halo like shape is visible in the negative part. Therefore, the XRPD data reveals that all samples with NMFs between 0.1 and 0.6 recrystallize predominantly under formation of γ-IND, while the 0.7 samples recrystallize under formation of cNAP. It appears, that the most stable samples after 56 and 112 days of storage are those with an NMF of 0.6, which is in contrast to literature reports postulating that the equimolar system (NMF of 0.5) represents the physically most stable composition for co-amorphous NAP/IND [65] and for binary co-amorphous systems in general [89,56].

To confirm the results from the XRPD dataset, FTIR analysis was performed, and the obtained spectra were also evaluated by PCA. The resulting PCA scores plot (Fig. 24) divides the stored samples into three groups predominantly along the PC-1 axis. In the negative part of the PC-1 axis, the 0.9 and 0.8 samples can be found, while in the positive part all samples with NMFs from 0.40 to 0.10 are located. In contrast, the 112 days stored samples with NMFs of 0.7, 0.6, 0.55 and 0.5 cluster near the center of the scores plot. As the PC-1 loading (Fig. 25) shows γ-IND signals in the positive and cNAP signals in the negative part, the samples with NMFs of 0.8 and 0.9 recrystallize under formation of cNAP while those with NMFs of 0.4 – 0.1 recrystallize predominantly under formation of γ-IND, which confirms the results of the XRPD dataset. The PC-2 loadings plot (Fig. 25) shows cNAP and γ-IND FTIR signals in the positive and REF signals in the negative part. Therefore, PC-2 separates crystalline samples from co-amorphous samples and the stored 0.6 samples that cluster at PC-1 scores near the zero line and at low PC-2 scores are the least crystalline, as already shown by XRPD.

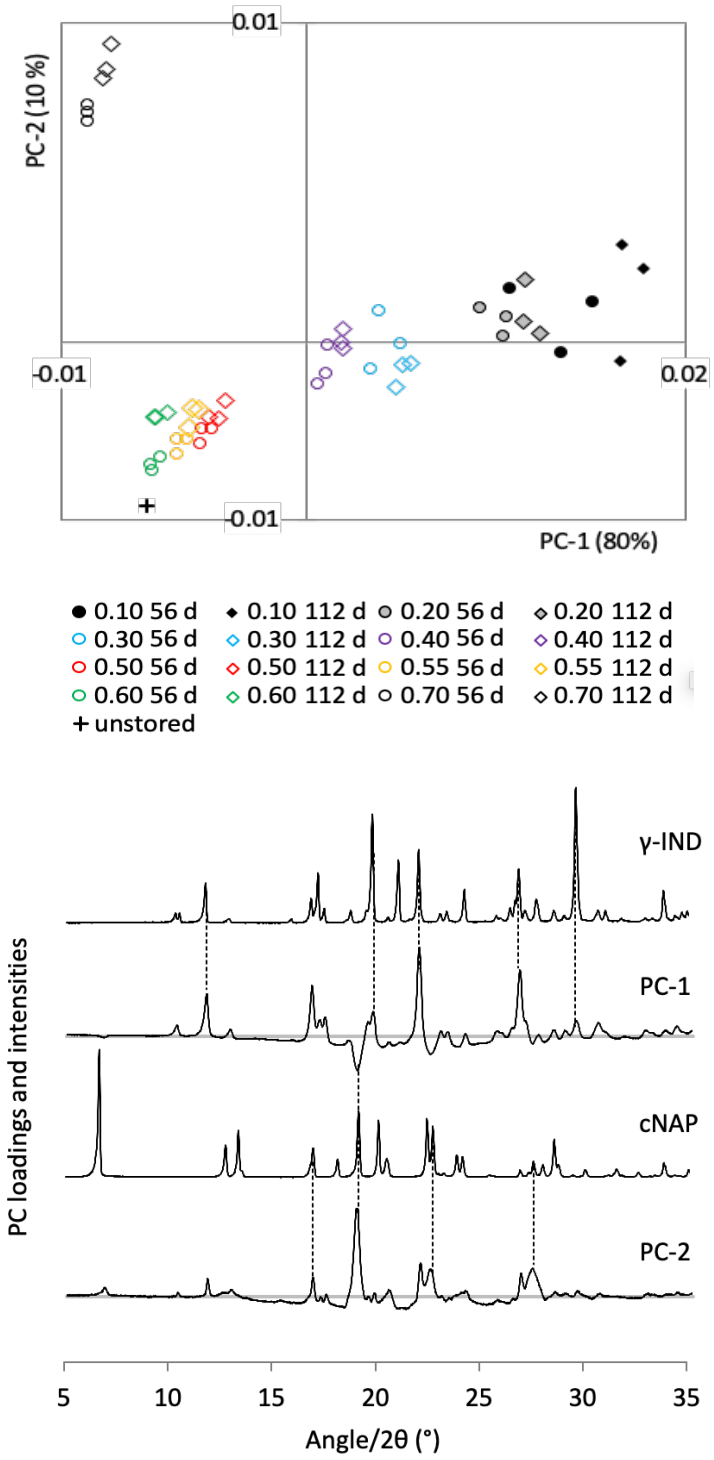

Fig. 23: PCA scores plot for the XRPD dataset of the stored NAP/IND samples with NMFs between 0.10 and 0.70 (top). Corresponding PC-1 and PC-2 loadings plots as well as reference diffractograms of γ-IND and cNAP (bottom).

The PCAs of the XRPD and FTIR dataset indicate that either cNAP or γ-IND is formed during storage depending on the NAP/IND blend ratio in the co-amorphous phase. To confirm these observations, the halo baseline-subtracted diffractograms of the samples with NMFs between 0.1 and 0.6 (Fig. 26) as well as those with NMFs between 0.7 and 0.9 (Fig. 27) are shown together with the reference diffractograms of γ-IND and cNAP. It is obvious, that the peaks of the first group can predominantly be assigned to γ-IND while the peaks of the second group are predominantly assignable to the reference diffractogram of cNAP. Therefore, the results of the PCAs are confirmed. Knowing which phase predominantly recrystallizes in the differently composed samples, the total γ-IND fraction $F_{\gamma\text{-IND}}$ and the total cNAP fraction F_{cNAP} in the stored samples may be calculated based on the total amorphous fraction F_{am} according to Equation 11 and Equation 12, respectively.

$$F_{\gamma\text{-IND}}=1-F_{am} \qquad \text{Equation 11}$$

$$F_{cNAP}=1-F_{am} \qquad \text{Equation 12}$$

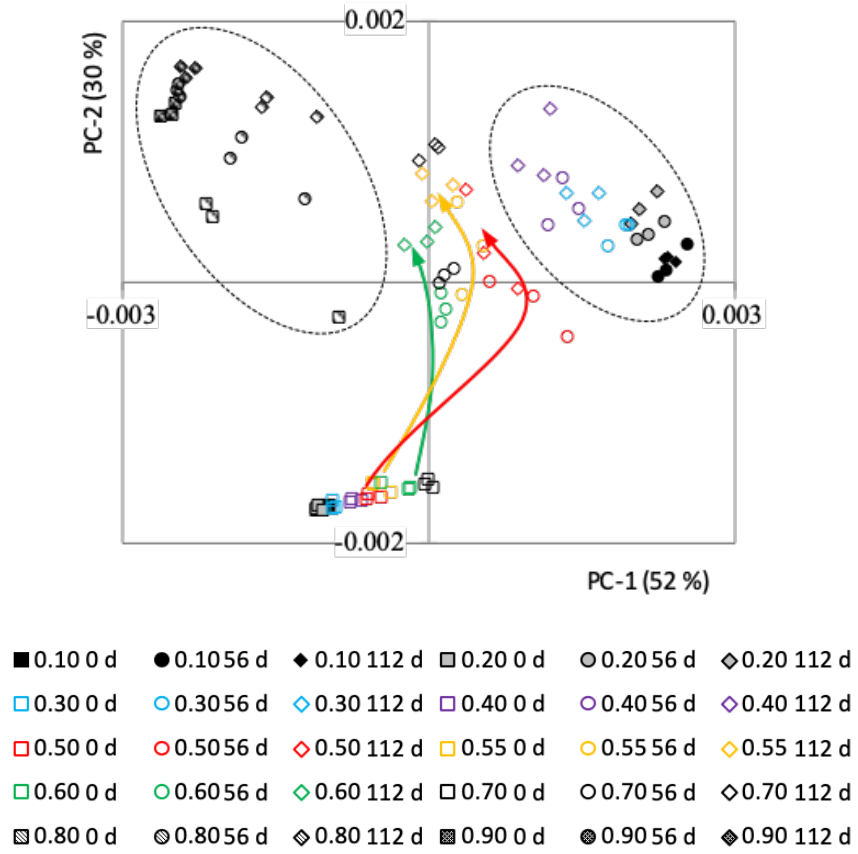

Fig. 24: PCA scores plot for the FTIR dataset of the stored samples with NMFs between 0.10 and 0.90.

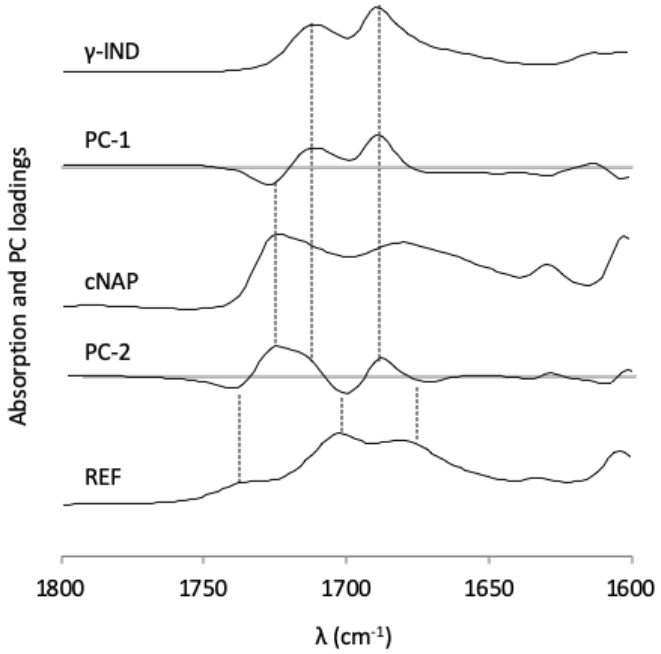

Fig. 25: Corresponding PC-1 and PC-2 loadings plots as well as reference spectra of γ-IND, cNAP and unstored equimolar co-amorphous NAP/IND (REF).

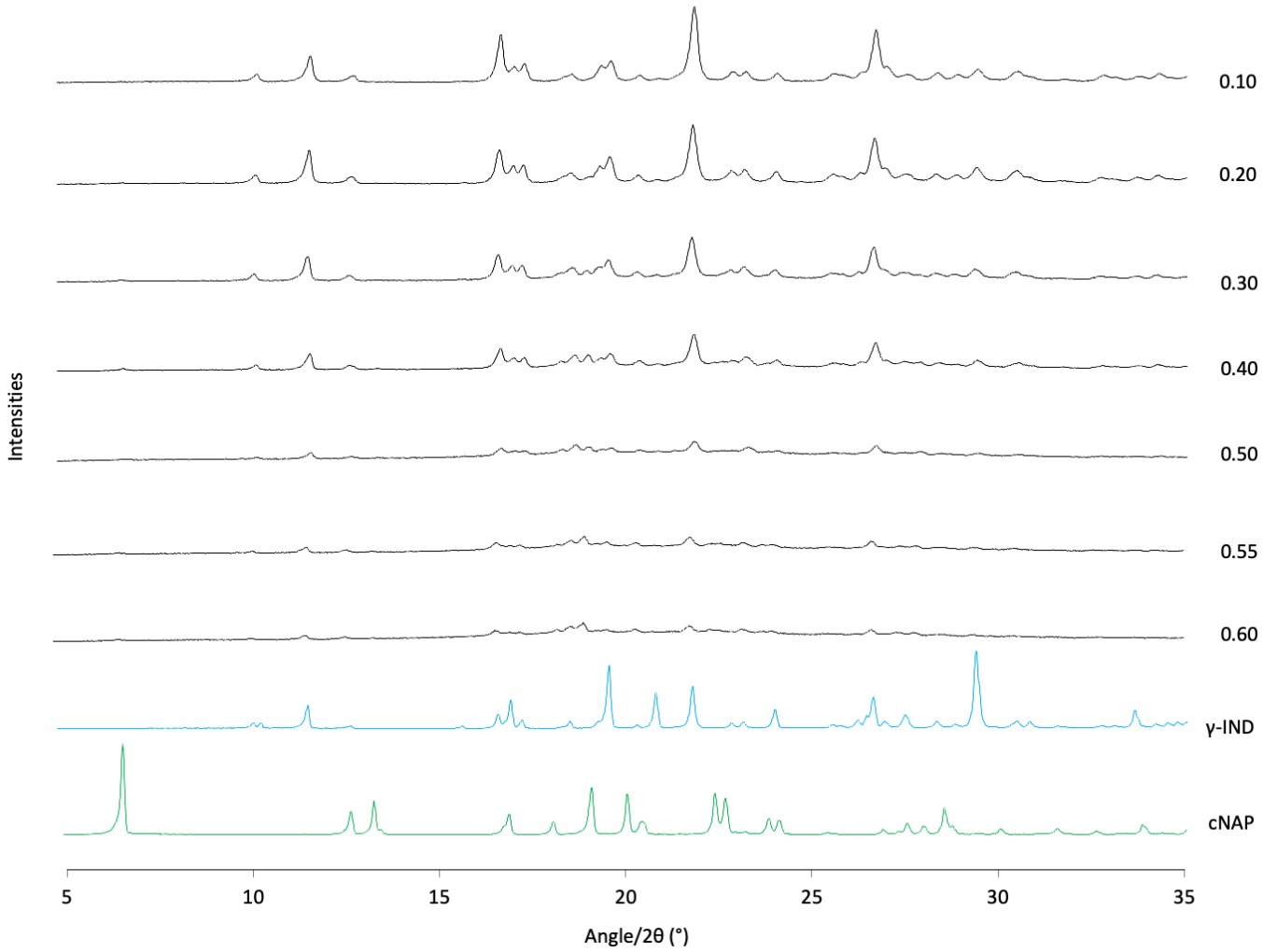

Fig. 26: Identically scaled baseline offset corrected and normalized X-ray powder diffractograms of 112 d stored samples with NMFs between 0.10 - 0.60 versus the reference diffractograms of cNAP and γ-IND.

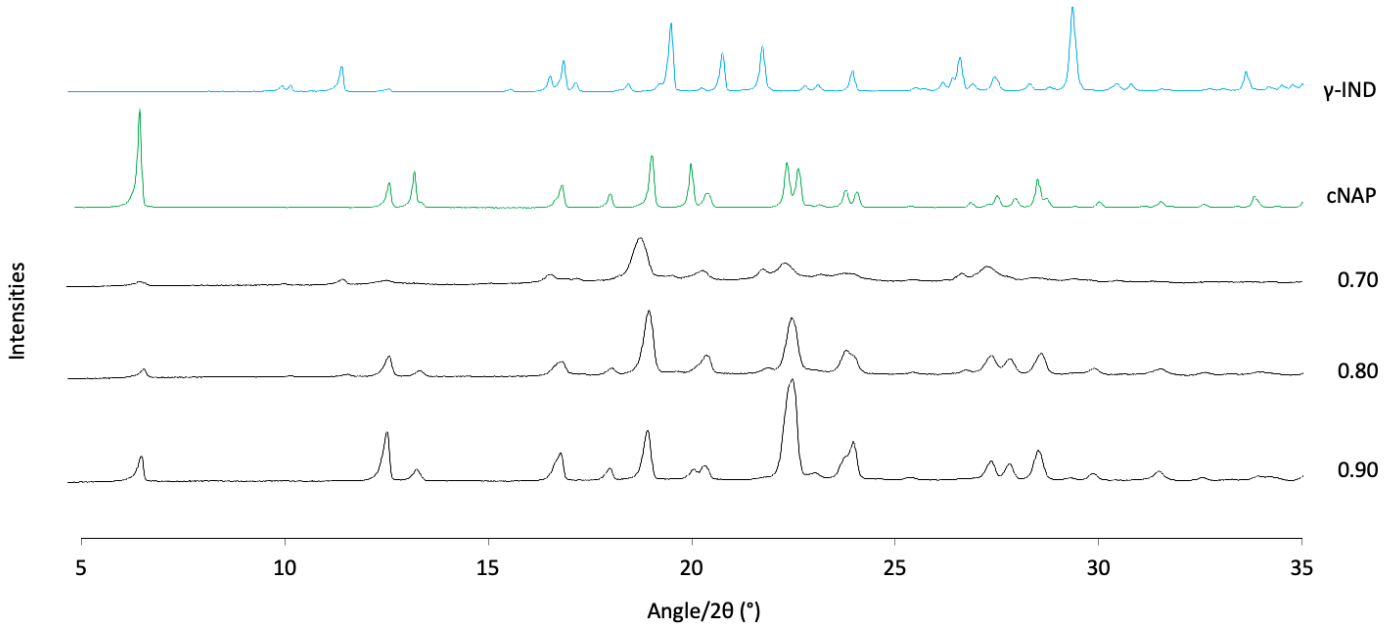

Fig. 27: Identically scaled baseline offset corrected and normalized X-ray powder diffractograms of 112 d stored samples with NMFs between 0.70 – 0.90 versus the reference diffractograms of cNAP and γ-IND.

In

Fig. 28, the calculated fractions $F_{\gamma\text{-IND}}$ and F_{cNAP} that are present in the stored samples are plotted versus their NMFs. The V-like shape of the data indicates that the 112 days-physical stability is strongly dependent on the NMF and that the optimal physical stability is found for the 0.6 (F_{am} = 0.94) followed by the samples with NMFs of 0.55 and 0.5 (F_{am} of about 0.89).

However, slight deviations from the 0.5 – 0.6 NMF range leads to significant sample recrystallization. Based on the calculated $F_{\gamma\text{-IND}}$ and F_{cNAP} fractions, the composition of the residual amorphous phase after storage in terms of the residual molar amorphous naproxen fraction ($NMF_{Residual}$), after recrystallization occurred, may be calculated by Equation 13.

$$NMF_{Residual} = \frac{NMF_{Initial} - F_{cNAP}}{F_{am}} \qquad \text{Equation 13}$$

Where $NMF_{residual}$ is the residual naproxen molar fraction based on the initial naproxen molar fraction ($NMF_{initial}$), the crystalline naproxen fraction (F_{cNAP}) and the amorphous fraction (F_{am}).

In Fig. 28, the residual NMFs after 56 and 112 days of storage are also plotted. Interestingly, after 112 days of storage, the co-amorphous phase of the samples with NMFs between 0.2 and 0.8 reaches residual NMFs near 0.6 (0.603 ± 0.047), indicating that almost all samples recrystallize until a NAP/IND ratio in the co-amorphous phase near the previously found optimal composition with an NMF of 0.6 is reached again.

To find an explanation for the increased physical stability of samples with NMFs between 0.5 and 0.6, the reported phase diagram of the γ-IND/cNAP system by Löbmann et al. [65] was evaluated and revealed that the eutectic point, reported at an NMF of 0.55 [65] is located in this area. However, the eutectic point was also determined in the present study by evaluation of the heats of fusion of the eutectic peaks of differently composed γ-IND/cNAP physical mixtures. The resulting graphs in Fig. 29 intersect at an NMF_P of 0.596 and thus reveal an eutectic point at an NMF of 0.6 rather than 0.55 [65] in the co-amorphous phase. Therefore, the best physical stability is found exactly at the eutectic composition of co-amorphous NAP/IND.

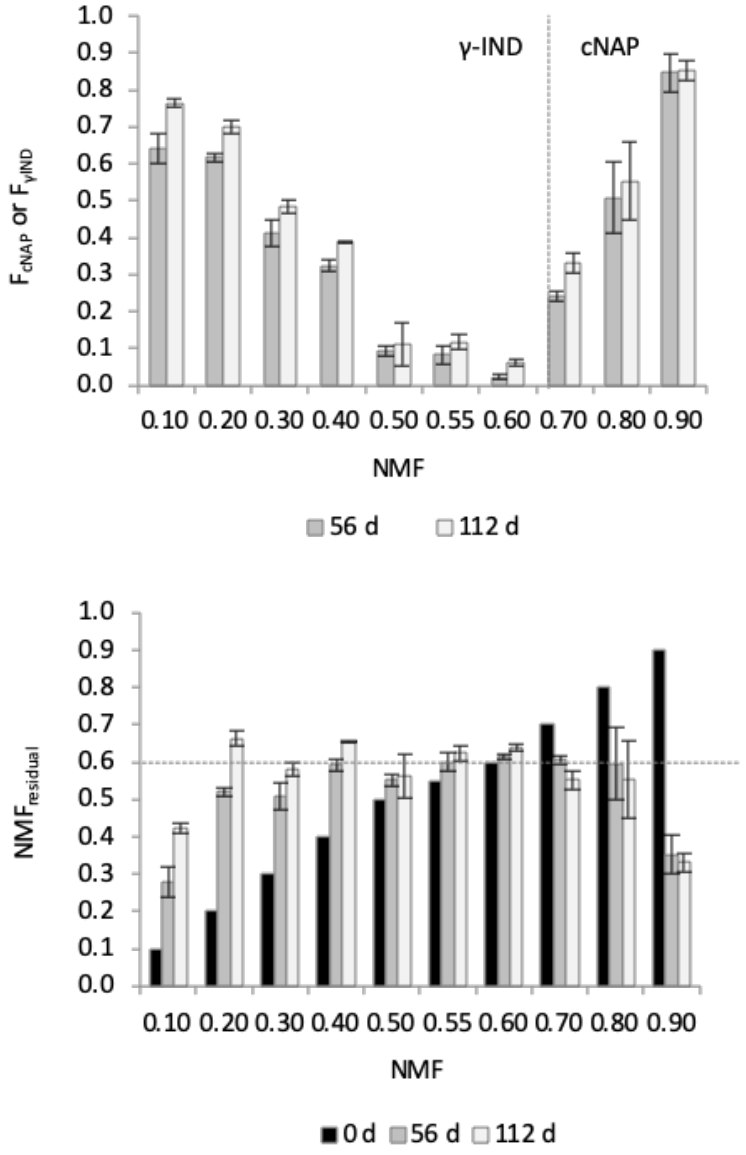

Fig. 28: Calculated mean molar fractions of γ-IND ($F_{γIND}$) or cNAP (F_{cNAP}) ± SD (n = 3) after 56 d and 112 d of storage (top) and mean residual naproxen molar fractions in the co-amorphous phase ($NMF_{residual}$) ± SD (n = 3) after 56 and 112 d (bottom) in dependence of the naproxen molar fraction (NMF) in the samples.

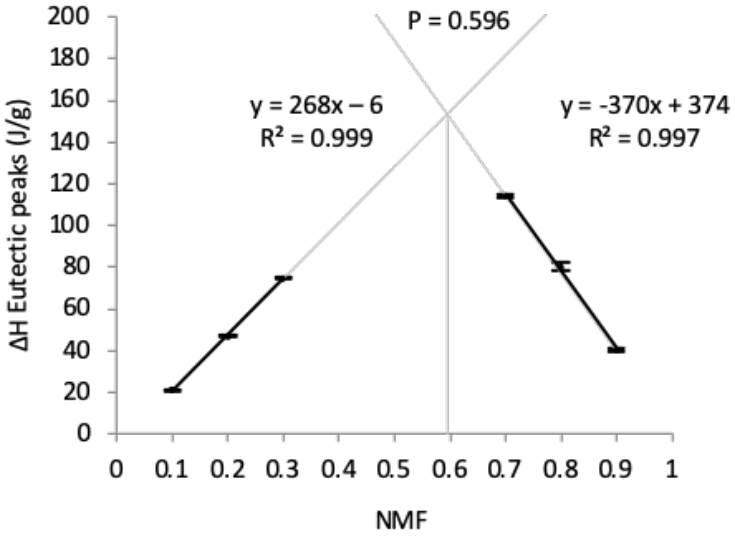

Fig. 29: Heats of fusion ± SD (n = 3) of the eutectic peaks in dependence of the naproxen molar fraction (NMF) in the respective cNAP/γ-IND physical mixtures.

It is reported that if two solids A and B form a eutectic system, the compounds are miscible in the molten state and immiscible in the solid state [116]. In the molten state, it is well known that the interactions between the compounds A and B are greater compared to the interactions between the like components [117,118] and for the eutectic composition it was reported that this interaction is very strong [119]. Therefore, it is expected that the interaction between NAP and IND might also be very strong at the eutectic composition in both the molten state and the resulting solidified co-amorphous state. From the findings reported in this study, it is thus suggested, that the most stable co-amorphous blend is likely to be found at the eutectic point of this mixture.

5.2.5 **Conclusion**

In conclusion, the obtained data revealed that intermediate cooling after melt-quenching and a naproxen molar fraction (NMF) in the co-amorphous phase of 0.6 results in the physically most stable co-amorphous NAP/IND samples. Furthermore, co-amorphous samples with NMFs different from 0.6 recrystallized predominantly under formation of either crystalline naproxen or γ-indomethacin until an NMF of again 0.6 in the residual co-amorphous phase was reached. Interestingly, the blend ratio of 0.6:0.4 represents the eutectic composition of the crystalline NAP/γ-IND system, which indicates that the eutectic point may play an important role for the stability of binary co-amorphous systems. In conclusion, the physical stability of co-amorphous NAP/IND can be significantly improved if suitable preparation parameters and the

optimal phase composition are chosen. These findings might also be applicable to other co-amorphous systems.

5.3 Improvement by addition of naproxen-sodium[3]

5.3.1 Unstored samples

To investigate if co-amorphous NAP-IND systems with NS instead of NAP may be obtained, different physical mixtures of NSNI and NSI (7.1.4) were prepared. The samples were transferred into a DSC, where the powders were pretreated by melting and subsequent cooling before thermal analysis was performed. All thermograms (Fig. 30) of both, the NSNI and the NSI samples reveal single Tgs, as was reported for the NI system [66,65], and thus indicate the formation of a single-amorphous phase. However, the Tg's reveal enthalpy recovery, which is visible at the area under the extrapolated heat curve of the region above the Tg. Without enthalpy recovery, the heat curve during the glass transition would not fall below the heat curve level after the Tg event [57]. This indicates that the samples lost energy due to relaxation, which is surprising as the samples have been prepared in-situ, i.e. the samples did not have much time to lose energy. The fast energy loss may indicate that the samples could be physically unstable upon storage.

In a next step, the same samples were molten ex situ before cooling to room temperature and XRPD analysis was performed. In Fig. 31 and Fig. 32, the resulting diffractograms of the NI, NSNI and the NSI samples are shown. The diffractograms of the 0.8 and 0.9 NI samples are not shown because distinct recrystallization occurred during preparation [66]. Moreover, complete melting was impossible with the 0.7 - 0.9 NSI samples and thus these samples were not investigated. For all systems, mainly amorphous samples could be prepared, indicated by the halo shapes of the majority of the diffractograms. With the NI and the NSNI systems, fully amorphous samples were obtained (Fig. 31), except for those with NAP molar fractions (NMFs) above 0.7.

In contrast, the NSI samples are fully amorphous only for NMFs up to 0.4, while peaks are visible in the diffractograms of the 0.5 and the 0.6 NSI samples (Fig. 32). For all NSNI (Fig. 31) and NSI (Fig. 32) samples, which show peaks in the diffractograms, melting of the respective powders was incomplete, as some crystalline fraction was still visible after the melting process.

[3] Parts of this chapter have been published as shown under 8.2 in the appendix.

The crystalline fraction can be identified as NS, because all peaks are assignable to its reference diffractogram (Fig. 32).

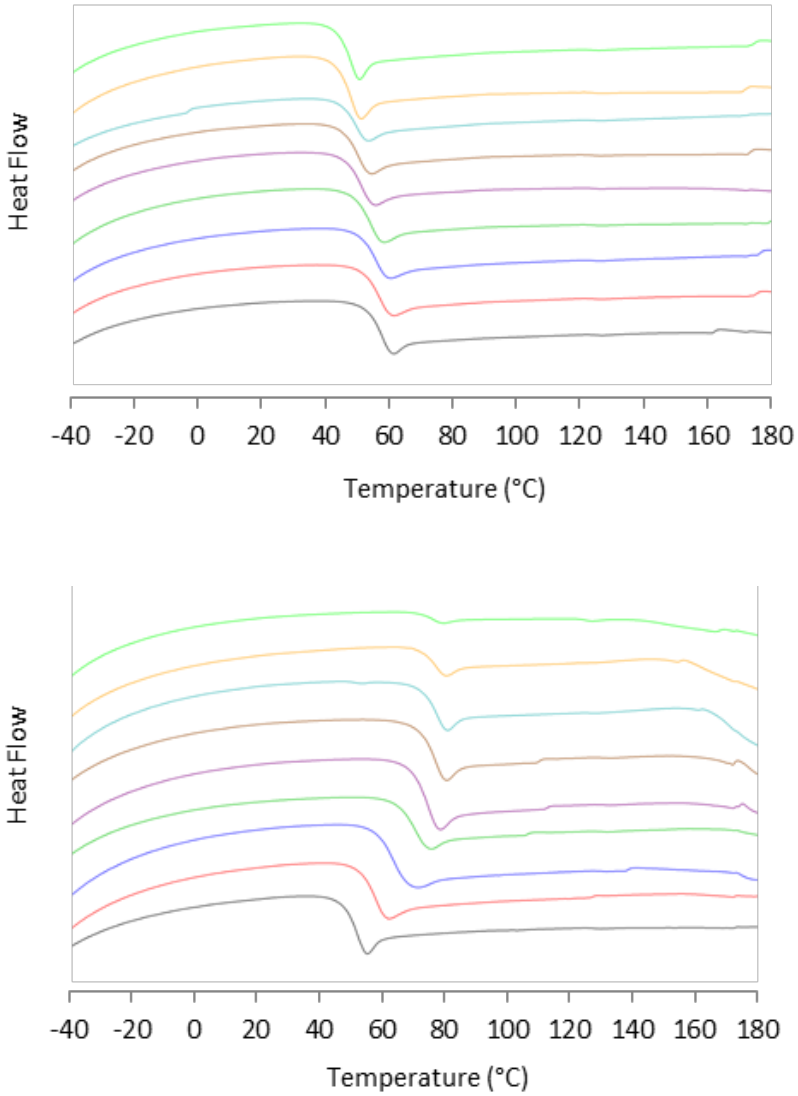

Fig. 30: Thermograms of the unstored NSNI (top) and NSI (bottom) samples with NMFs of 0.1 (black), 0.2 (red), 0.3 (blue), 0.4 (dark green), 0.5 (violet), 0.6 (brown), 0.7 (turquoise), 0.8 (orange) and 0.9 (light green).

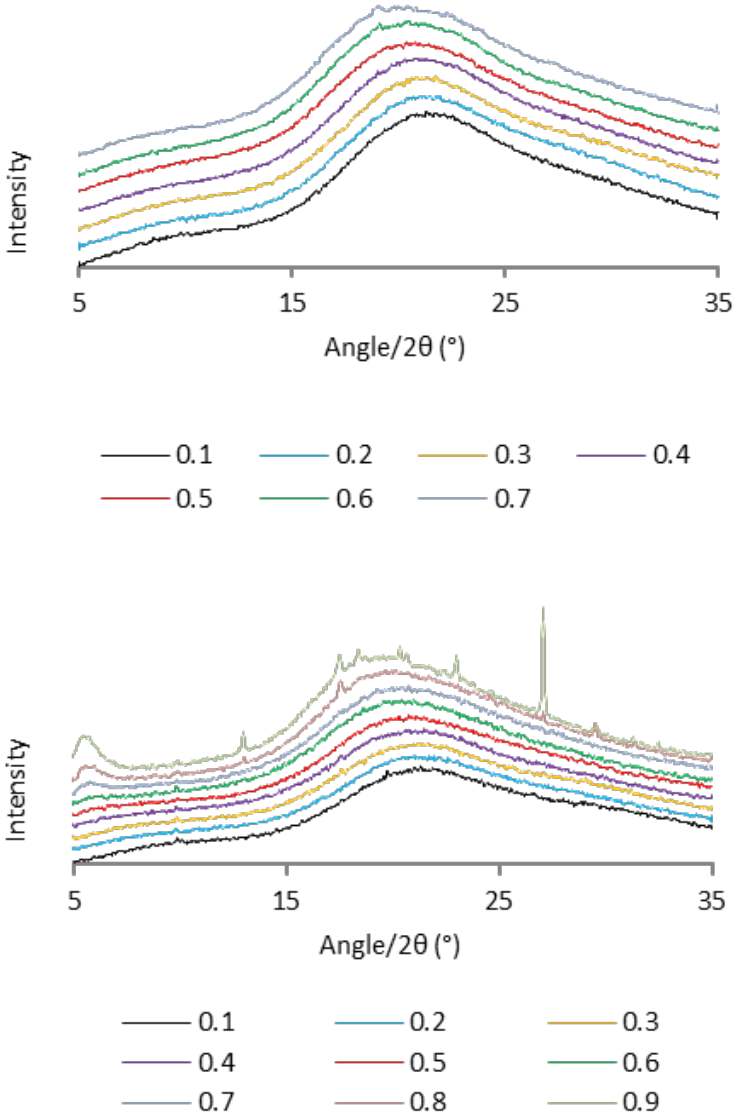

Fig. 31: Diffractograms of the unstored mainly amorphous NI (top) and NSNI (bottom) samples.

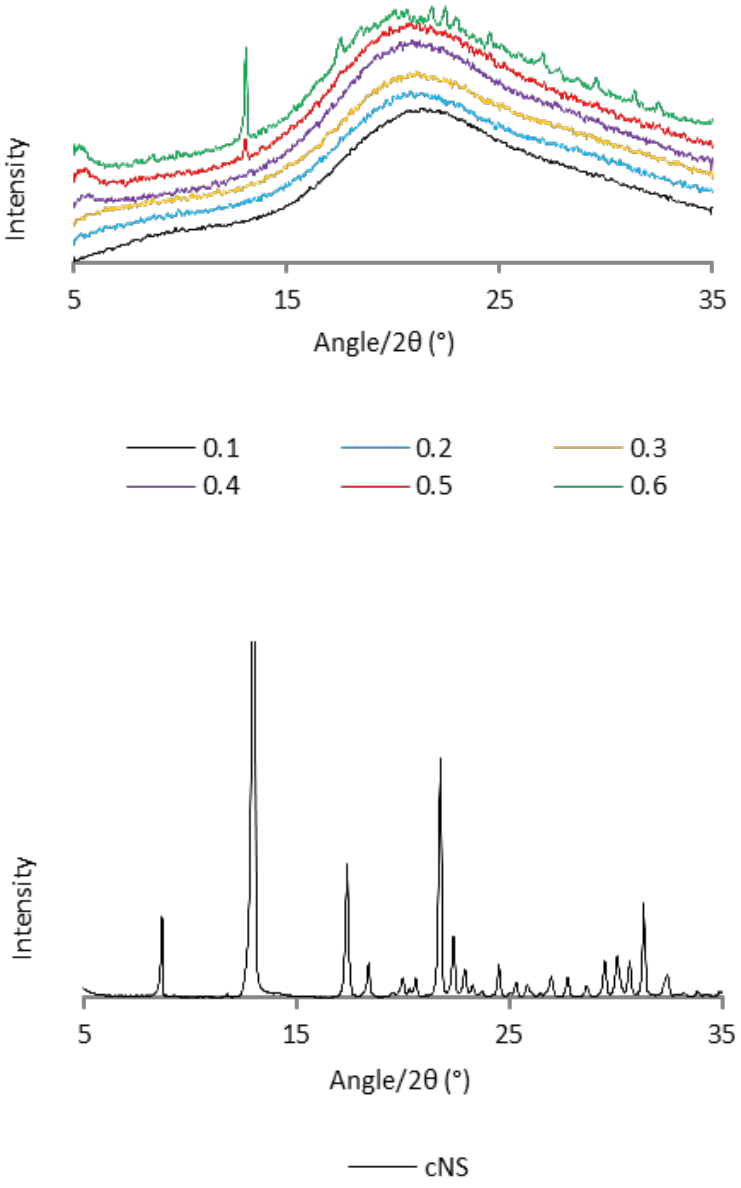

Fig. 32: Diffractograms of the unstored mainly amorphous NSI (top) samples as well as the reference diffractogram of cNS (bottom).

As only single glass transition temperatures and no peaks are present in the thermograms (Fig. 30) and diffractograms (Fig. 31 and Fig. 32) of the 0.1-0.7 NSNI and the 0.1-0.4 NSI samples, respectively, the formation of a single co-amorphous phase is suggested. As the preparation temperature of 180 °C only exceeded the melting temperatures of NAP (T_m = 158 °C) and γ-IND (T_m = 162 °C) but not that of cNS (T_m = 245 °C), it can be assumed that the ternary NSNI and the binary NSI systems form eutectic mixtures, because otherwise cNS peaks would appear in all diffractograms.

In Fig. 33, the Tgs of the NI (according to [65]), NSNI, and NSI samples are plotted versus their NMFs. As already reported [65], the Tgs of the NI samples decrease with an increase of the NMF, which results from the low Tg of amorphous NAP and leads to a reduced physical stability of the NI samples with high NMFs.

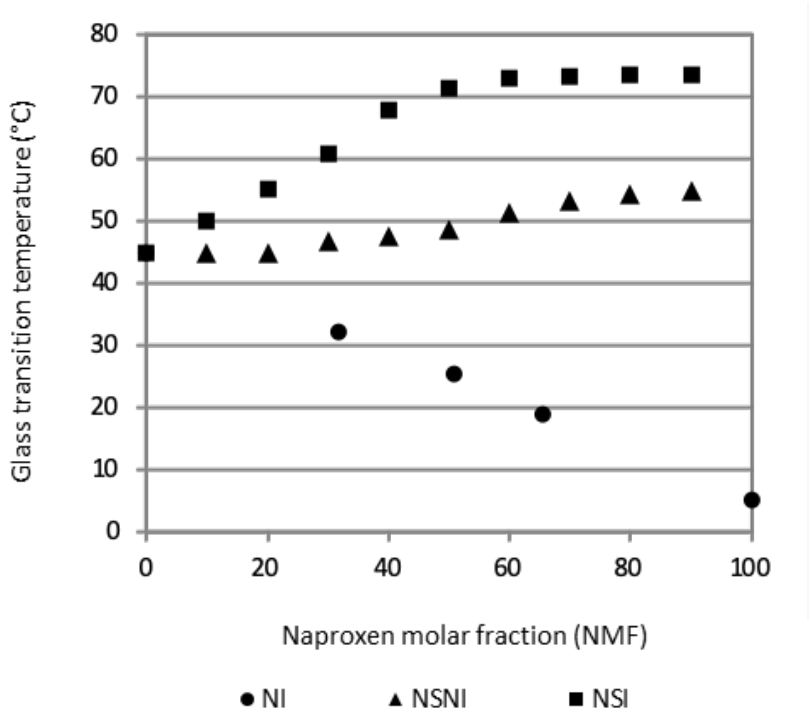

Fig. 33: Glass transition temperatures of the unstored NI (reported by Löbmann et al.), NSNI, and NSI samples (n = 1) plotted versus the naproxen molar fractions of the samples.

In contrast, the Tgs of the NSNI samples do not decrease with increasing NMFs, but slightly increase. This effect is even more pronounced with the NSI system, where the Tgs increase significantly, such that the Tg of the fully amorphous 0.4 NSI sample is almost 40 °C higher compared to the 0.4 NI sample. This observation supports the assumption that the NSNI and NSI powders are eutectic mixtures. Otherwise, cNS would not melt and the Tg increase could

not be observed. The Tg increase of the NSI samples reaches a plateau at about 70 °C for NMFs > 0.4 and all NSI samples with higher NMFs show XPRD peaks of cNS in the diffractograms (Fig. 32), which indicates that the maximum NS fraction that can be molten at 180 °C is limited to about 0.4. The melting temperature was not further increased during the experiments to prevent sample degradation. However, the Tg increase indicates that the NS containing NSNI and NSI samples are physically stabilized in comparison to NI. Consequently, the maximum NMF that can be reached in fully co-amorphous NAP-IND systems depends on the form of NAP (acid or sodium salt) and is limited because of the maximum possible melting temperature during sample preparation (NSNI and NSI) or the low physical stability of the resulting amorphous phase (NI, [66]).

To compare the fully amorphous NI, NSNI, and NSI samples with each other, FTIR analysis was performed. In Fig. 34, the FTIR spectra (1800 - 1000 cm^{-1}) of the respective NI (red), NSNI (blue), and NSI (green) systems with NMFs of 0.1 (A), 0.2 (B), 0.3 (C) and 0.4 (D) are shown together with the reference spectra of cNS, amorphous IND and equimolar NI for comparative purposes. The amorphous form of NS could not be prepared and the spectrum is therefore unavailable. However, the reference spectrum of the crystalline form of NS may be used for comparison as the spectra of the amorphous and the crystalline form of a drug generally differ only slightly [61]. The direct comparison of the three different samples in the four plots reveals that the most distinct differences are found in the spectral region between 1800 cm^{-1} and 1500 cm^{-1}. The band at 1680 cm^{-1}, which represents the benzoyl function of IND, decreases with increasing NS fraction although the IND fraction is the same within each of the four plots, which indicates a change in the molecular environment of the benzoyl function. The intensity of the band at 1703 cm^{-1}, which represents the COOH heterodimer interaction between NAP and IND in the NI system [65] decreases, which results from the ionization of the COOH group in NS [61]. Thus, no interaction between NAP and IND via the COOH functions can take place. However, the almost complete disappearance of the absorption band at 1703 cm^{-1} (0.4 NSI samples, D), which is located in the spectral region where COOH homodimers in amorphous IND also show FTIR bands (Fig. 34E), indicates that no COOH-homodimer interactions between IND molecules occur in the NSI system either. The band at 1734 cm^{-1} which represents free NAP and IND carboxyl functions that are present in the co-amorphous NI (Fig. 34E) as well as in the respective single-amorphous phases [65], almost fully disappears with increasing NS fraction.

Thus, the IND molecules are neither present as monomers nor as homodimers, which indicates a significant influence of NS resulting in a different kind of interaction mode of IND in the co-amorphous phase. The absorption in the spectral region between 1500 - 1600 cm^{-1} increases

with the NS fraction, which is the region where ionized carboxyl functions usually show absorption bands [120]. For NS, the bands at about 1480 and 1580 cm^{-1} are due to the symmetrical and asymmetrical COO- stretching, respectively [121]. Therefore, the general increase in absorption intensity between 1500 and 1600 cm^{-1} may indicate an interaction between NS and IND in the co-amorphous phase.

5.3.2 **Stored samples**

The three different investigated samples (NI, NSNI, and NSI) were stored for up to 270 d under dry conditions and analyzed by XRPD to evaluate their physical stability (Fig. 35 and Fig. 36). In Fig. 35, the diffractograms of the NI samples after 120 d of storage are shown [66]. Obviously, all samples show distinct recrystallization peaks of γ-IND or NAP, in accordance with the already reported low physical stability of the NI system [66,122,65]. In contrast, the diffractograms of the NSNI (Fig. 35) and NSI (Fig. 36) samples stored for 270 d reveal that no recrystallization occurred with all samples that were initially fully amorphous, which is the case with the 0.1–0.7 NSNI and the 0.1–0.4 NSI samples. Therefore, the observed increased Tgs of the fully amorphous NSNI and NSI samples compared to the NI samples (Fig. 33) also result in a distinct increase of the physical stability of these samples, which contradicts the assumption that the enthalpy of recovery, that was observed during the glass transition, would indicate a sample physical stability. Interestingly, the NSI samples that were partially crystalline at the beginning further recrystallized during storage while the NSNI samples did not. This indicates a stabilizing effect of NAP in the ternary co-amorphous NSNI system, which results in a higher allover NAP ratio that can be obtained as well as in a higher physical stability.

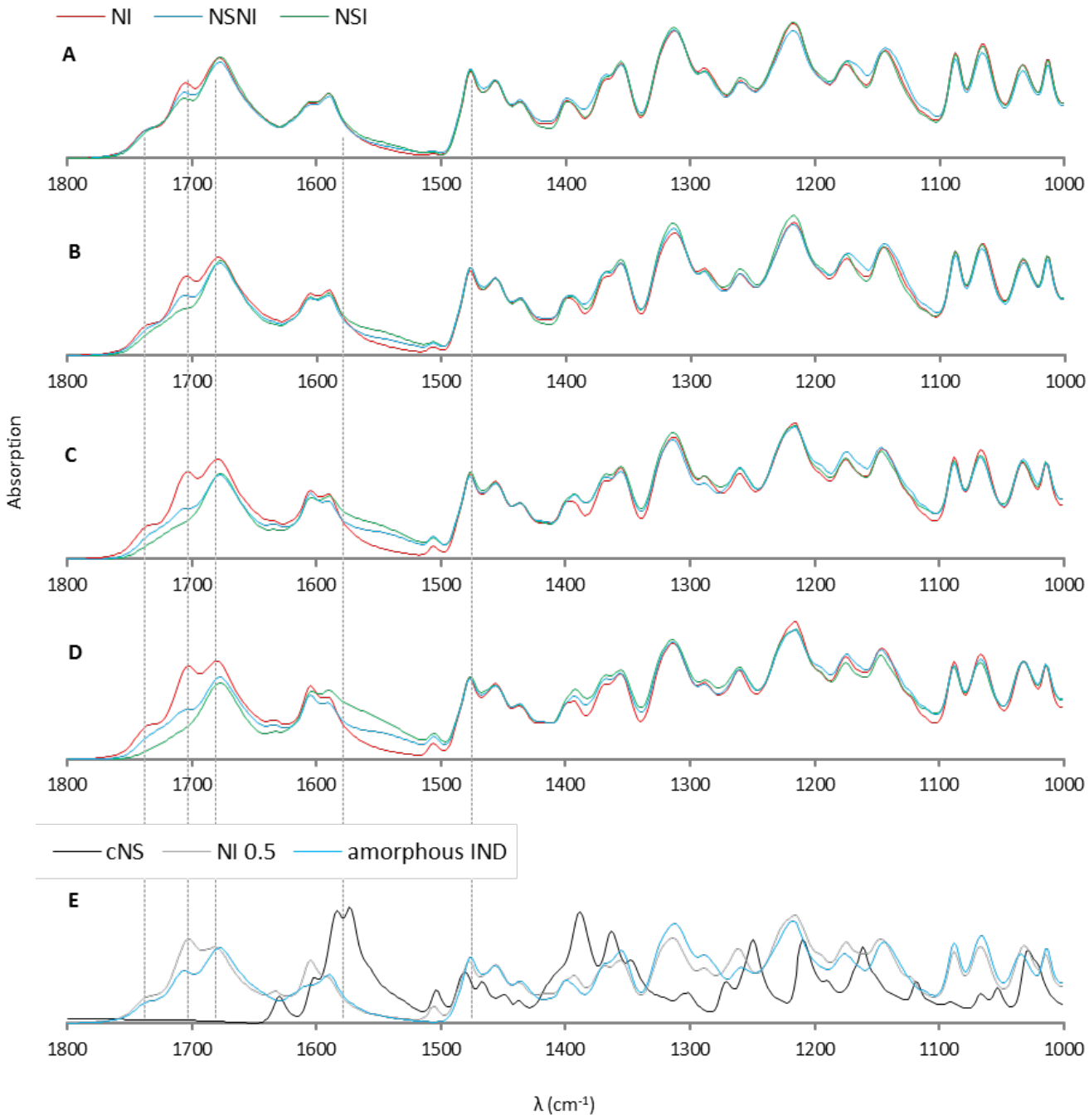

Fig. 34: FTIR spectra of the unstored NI (red), NSNI (blue), and NSI (green) samples with naproxen molar fractions of 0.1 (A), 0.2 (B), 0.3 (C), and 0.4 (D) as well as the reference spectrum of crystalline naproxen-sodium (cNS), unstored equimolar co-amorphous NI (NI 0.5), and amorphous IND (E).

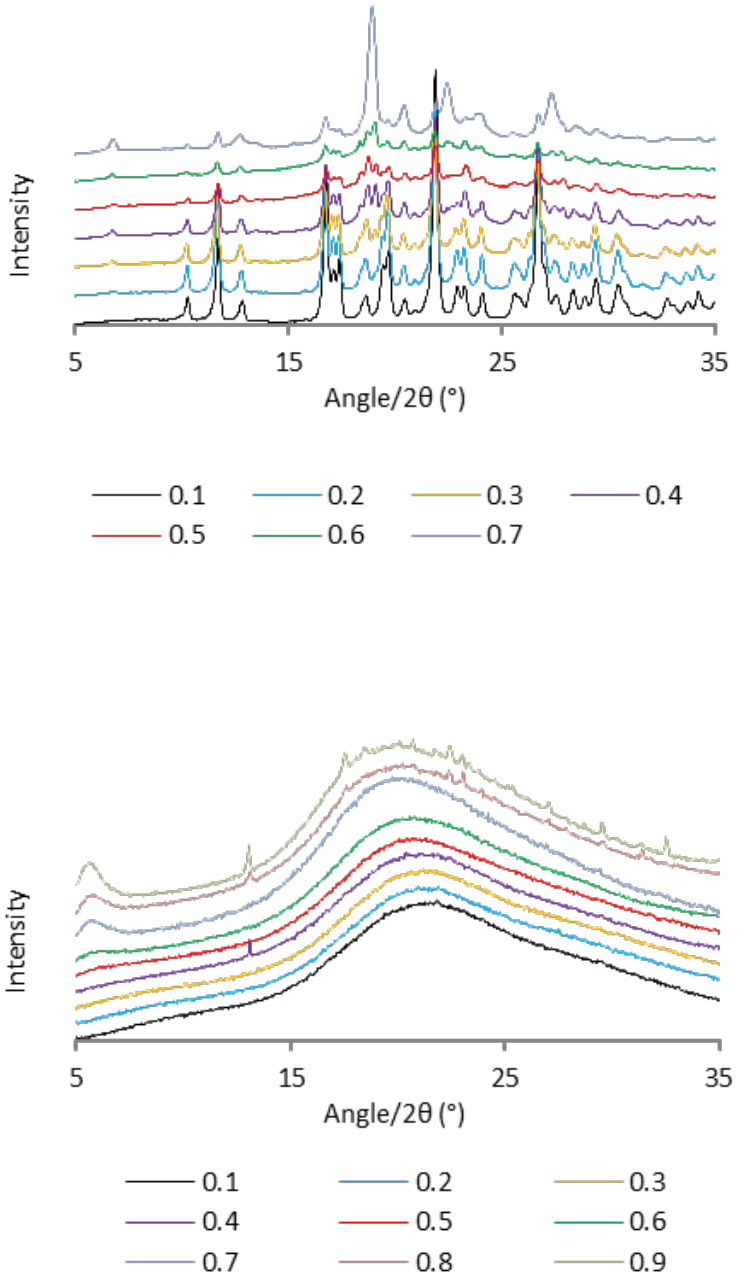

Fig. 35: Diffractograms of the initially mainly amorphous NI samples after 120 days (top) and NSNI samples after 270 days of storage (bottom).

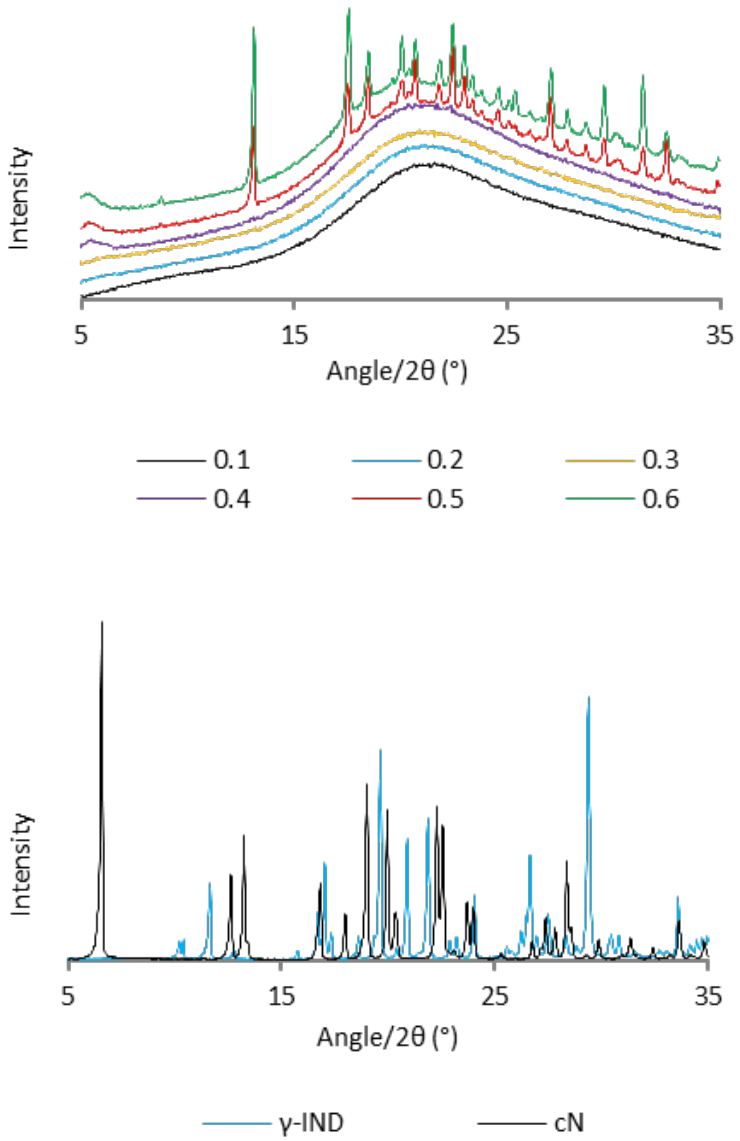

Fig. 36: Diffractograms of the initially mainly amorphous NSI samples after 270 days of storage (top) as well as the reference diffractograms of cNAP and γ-IND (bottom).

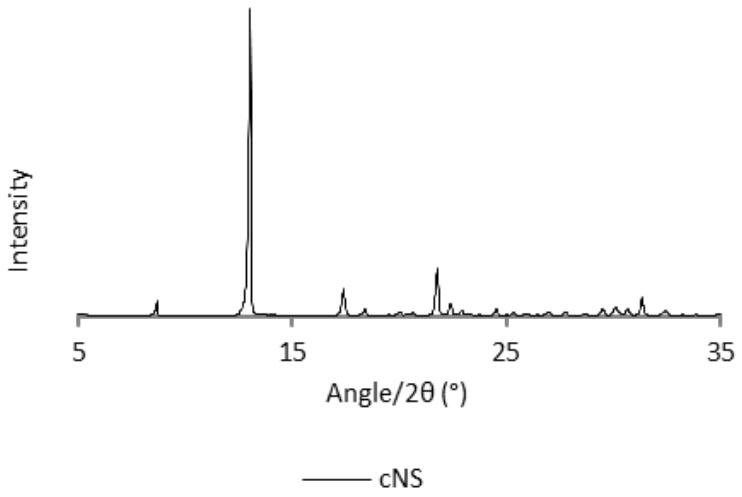

Fig. 37: Reference diffractogram of cNS.

5.3.3 **Intrinsic dissolution**

Löbmann et al. [65] demonstrated that equimolar co-amorphous NI shows improved intrinsic dissolution profiles with regard to the NAP and IND release compared to cNAP, γ-IND and amorphous IND. As the increased physical stability of the NSNI and NSI system has already been confirmed, it was investigated if the dissolution profile could also be improved if NS instead of NAP is used in the co-amorphous formulation. In Fig. 38, it is shown that the equimolar NSI sample releases more NAP and IND than the equimolar NI sample.

After 60 min, the NAP and IND concentration in the vessel with the NSI sample (0.203 ± 0.026 NAP and 0.226 ± 0.008 IND mmol / 750 ml, respectively) was twice higher compared to the vessel with the NI sample (0.116 ± 0.010 NAP and 0.112 ± 0.010 IND mmol / 750 ml, respectively).

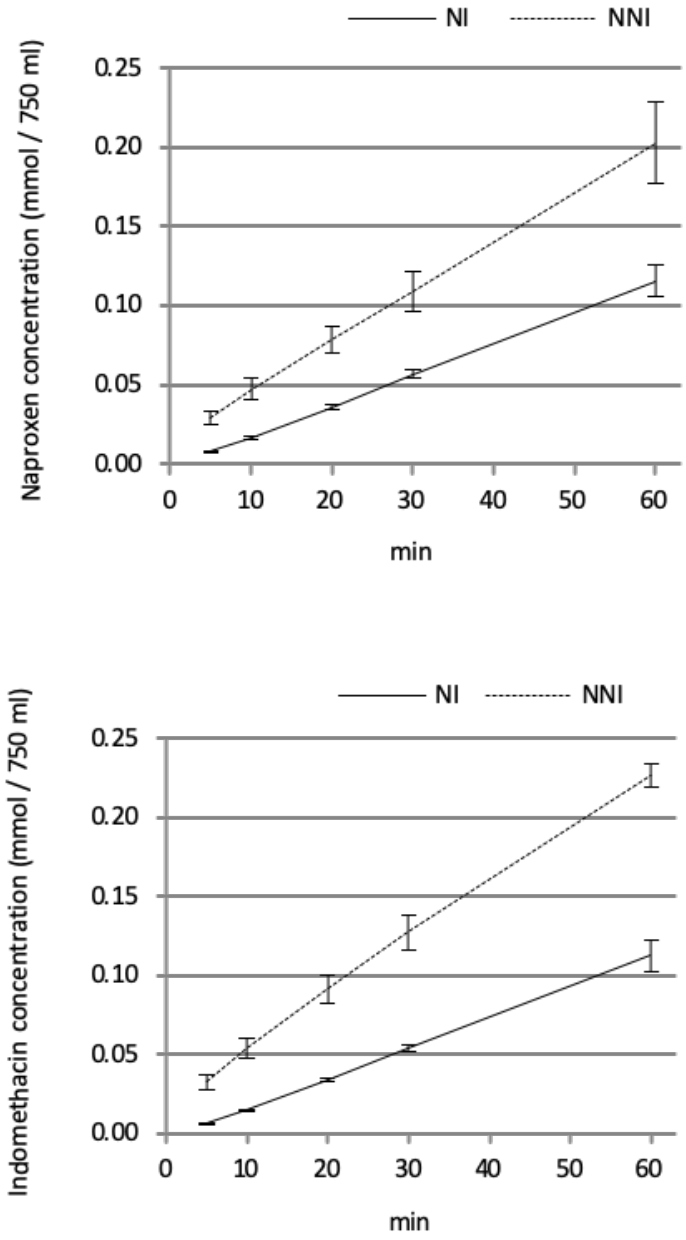

Fig. 38: Intrinsic dissolution profiles of the NI and NSI samples (means ± SD, n = 3) for NAP (top) and IND (bottom)

5.3.4 **Conclusion**

In conclusion, the data presented in this study reveals that it is possible to prepare fully amorphous binary co-amorphous systems of naproxen-sodium and indomethacin (NSI) as well as ternary co-amorphous systems of naproxen-sodium, naproxen and indomethacin (NSNI) with naproxen molar fractions of up to 0.4 (binary systems) or 0.7 (ternary systems), respectively. The resulting samples showed increased single glass transition temperatures that were up to about 40 °C higher compared to the naproxen/indomethacin (NI) samples. Consequently, significantly improved physical stabilities of the NSI and NSNI samples resulted.

During 270 d of storage, the initially amorphous NSI and NSNI samples did not recrystallize. Moreover, with the equimolar NSI samples, the intrinsic dissolution rate of naproxen and indomethacin could be increased by a factor of 2 compared to the NI samples. In conclusion, partial or full modification of the content of one component in binary co-amorphous systems with its salt form may provide a general approach for a further increase of the physicochemical properties of co-amorphous systems without altering the respective pharmacological profile.

5.4 Multivariate quantification of the phase composition[4]

5.4.1 Phase composition of co-amorphous naproxen/indomethacin

During the recrystallization of co-amorphous naproxen/indomethacin (aNAP/IND), the formation of crystalline naproxen (cNAP), γ-indomethacin (γ-IND) and α-indomethacin (α-IND) may occur, i.e. up to four solid state phases can be present at the same time. Thus, in the respective diffractograms, the intensity of the halo signal resulting from the co-amorphous portion decreases over time, while the peak intensities resulting from the crystalline components increase. To fully characterize the solid-state phase composition of aNAP/IND samples, the determination of the molar fractions (F) that are present as cNAP, γ-IND and α-IND is sufficient. Taking the total naproxen (F_{NAP}) and indomethacin fraction (F_{IND}) into account, that are known by weight, the amorphous NAP fraction (F_{amNAP}) and the amorphous IND fraction (F_{amIND}) that together form the total (co-)amorphous fraction F_{am} can be determined according to the equations in Fig. 39. Furthermore, the total molar crystalline IND fraction $F_{\alpha+\gamma}$ and the total molar crystalline fraction F_{cryst} may be predicted.

5.4.2 Molar crystalline naproxen fraction F_{cNAP}

Three PLS components (PLSCs) were found to describe 99 % of the cNAP variance in the calibration samples. In

Fig. 40, the reference diffractograms of cNAP, γ-IND, α-IND and the first three PLSC loadings plots are shown. PLSC-1 (85 %) distinguishes cNAP diffraction signals (positive part) from γ-IND and α-IND intensities (negative part), while PLSC-2 (12 %) distinguishes cNAP and γ-IND diffraction signals (positive part) from α-IND and halo intensities (negative part).

[4] Parts of this chapter have been published as shown under 8.2 in the appendix.

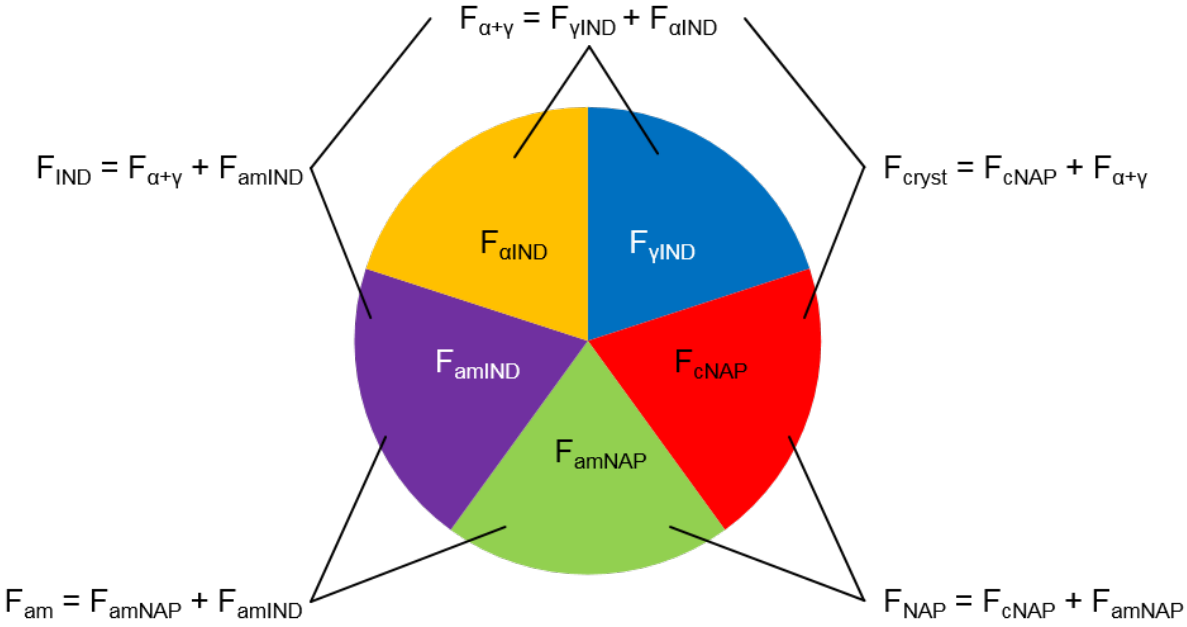

Fig. 39: Circular chart showing the phases that can be present during the recrystallization of co-amorphous naproxen/indomethacin. The different colors represent the molar fractions of cNAP (F_{cNAP}), γ-IND ($F_{\gamma IND}$), α-IND ($F_{\alpha IND}$), amorphous NAP (F_{amNAP}) and amorphous IND (F_{amIND}). F_{am} represents the total molar amorphous fraction, $F_{\alpha+\gamma}$ the total molar crystalline IND fraction, F_{cryst} the total molar crystalline fraction, F_{IND} the total molar IND fraction and F_{NAP} the total molar NAP fraction.

Thus, the positive parts of both PLSCs contribute significant information to describe the cNAP fraction of the samples and therefore samples with high cNAP fractions cluster in the positive part in the PLSC-1-vs-PLSC-2 scores plot, while samples with low or no cNAP fraction locate in quadrant two and three (Fig. 41). PLSC-3 (2 %) separates α-IND and some small cNAP signals (positive part) from halo intensities (negative part) and thus only contributes little information to describe the cNAP fraction in the samples.

Comparison of the PLS predicted molar fractions of cNAP versus the reference values reveals linearity between 0 and 100 %, a goodness of fit (R^2) of 0.986 and a root mean square error (RMSE) of 2.62 %. These values change only slightly to 0.981 and 3.11 %, respectively, during cross validation and confirm good model performance (Fig. 41).

5.4.3 **Molar γ-indomethacin fraction $F_{\gamma IND}$**

Two PLSCs were found to describe 98 % of the γ-IND variance in the calibration samples. According to Fig. 42, PLSC-1 (91 %) distinguishes γ-IND diffraction signals (positive part) from cNAP and some α-IND intensities (negative part) and PLSC-2 (6 %) distinguishes γ-IND and

cNAP diffraction signals (positive part) from α-IND and halo intensities (negative part). Thus, the positive parts of both PLSCs contain information to describe the γ-IND fraction of the samples and therefore, as it is also the case for the cNAP PLS model, samples with higher γ-IND content cluster in the first and fourth quadrant of the PLSC-1-vs-PLSC-2 scores plot, while samples with small or no γ-IND fraction cluster in the second and third quadrant (Fig. 43).

In Fig. 43, the predicted values of $F_{\gamma IND}$ are plotted versus the reference molar fractions. A linear correlation was found for γ-IND fractions between 0 and 78.1 %. Thus, the γ-IND PLS model is not applicable for samples with γ-IND fractions higher than 78.1 %. The R^2 of 0.976 and the RMSE of 2.98 % reveal a good model performance and only slightly change during the cross validation (R^2: 0.972; RMSE: 3.30 %).

5.4.4 **Molar α-indomethacin fraction $F_{\alpha IND}$**

Three PLS components were found to describe 97 % of the α-IND variance in the calibration samples. According to Fig. 44, PLSC-1 (66 %) distinguishes α-IND and halo diffraction signals (positive part) from γ-IND and cNAP intensities (negative part) and PLSC-2 (25 %) distinguishes α-IND and γ-IND diffraction signals (positive part) from halo intensities (negative part). Both positive parts of the PLSC-1 and PLSC-2 contain significant information to describe the α-IND fraction of the samples and therefore, samples with higher α-IND content cluster in the first and fourth quadrant of the PLSC-1-vs-PLSC-2 scores plot (Fig. 45). PLSC-3 (6 %) separates some small α-IND and cNAP diffraction signals (positive part) from γ-IND and halo intensities (negative part) and thus further specifies the α-IND fraction of the samples. In Fig. 45, the PLS predicted molar fractions of $F_{\alpha IND}$ are plotted versus their respective reference values. A linear correlation was found for α-IND fractions between 0 and 63.8 %. The α-IND PLS model is therefore not applicable for samples with α-IND fractions higher than 63.8 %. The R^2 of 0.968 and RMSE of 3.02 % change only slightly to 0.960 and 3.45 % respectively, during the cross validation, revealing a satisfactory model performance.

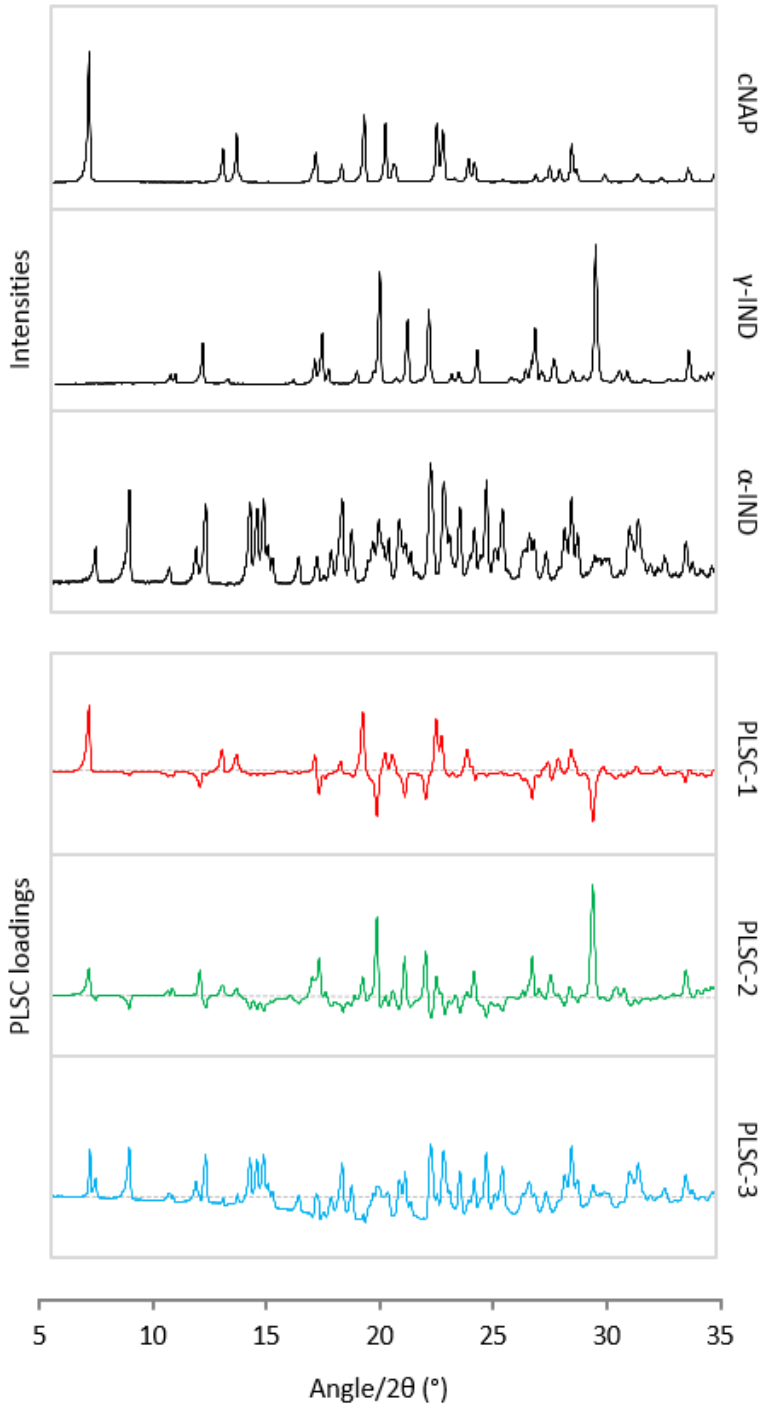

Fig. 40: Reference diffractograms of cNAP, γ-IND, α-IND and PLSC-1 (red), PLSC-2 (green) and PLSC-3 (blue) loadings plots for the F_{cNAP} PLS model

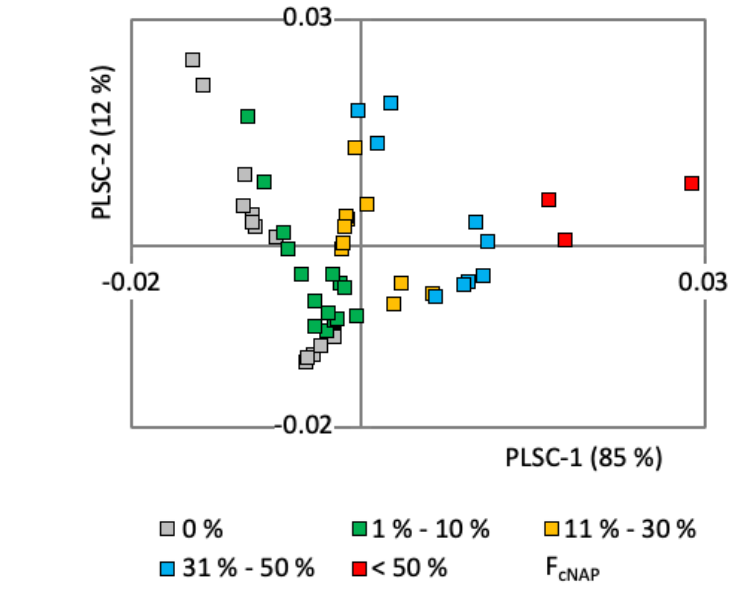

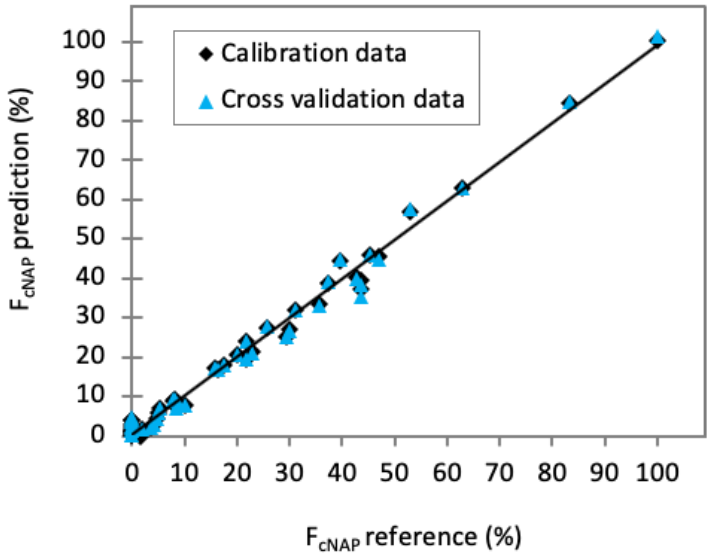

Calibration
Slope: 0.99; Offset: 0.25; RMSE: 2.62 %; R^2: 0.986
Validation
Slope: 0.98; Offset: 0.40; RMSE: 3.11 %; R^2: 0.981

Fig. 41: PLSC-1-vs-PLSC-2 scores plot, the different colors classify the calibration samples according to their cNAP fractions (top). Correlation of the PLS predicted cNAP fractions (bottom) during the calibration (black diamonds) and cross validation (blue triangles).

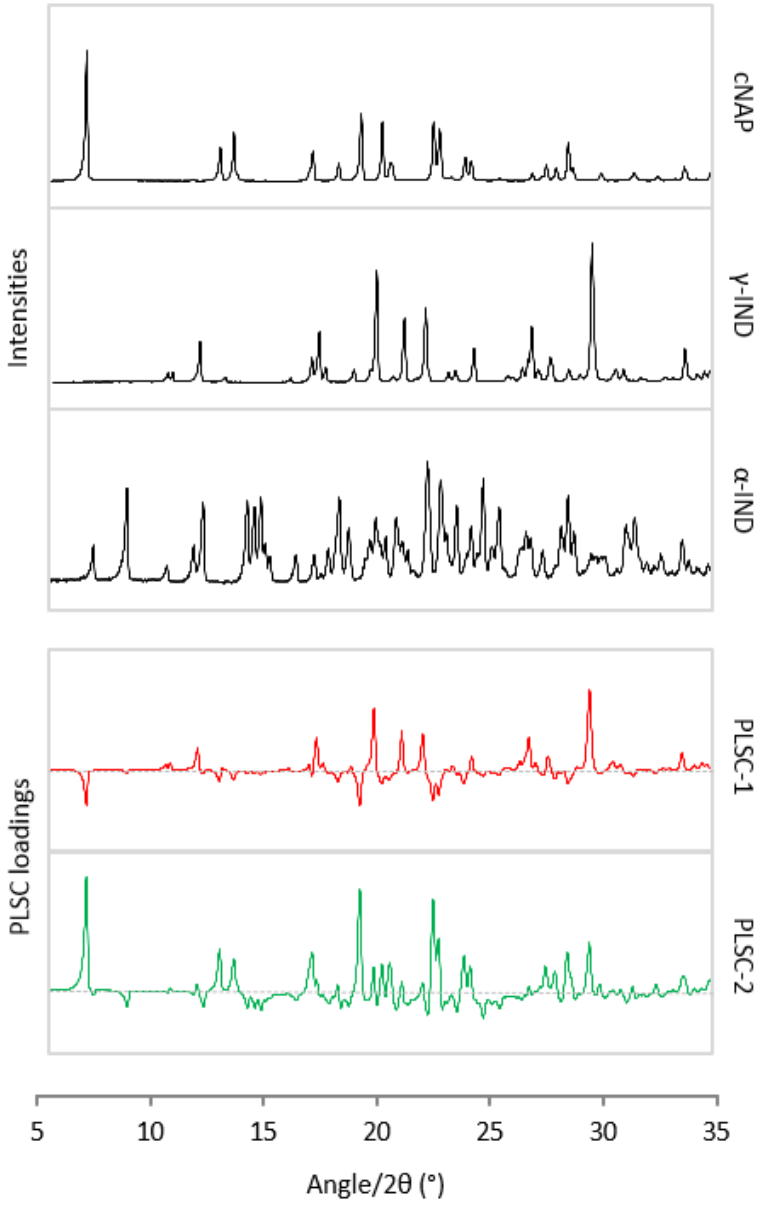

Fig. 42: Reference diffractograms of cNAP, γ-IND, α-IND and PLSC-1 (red) and PLSC-2 (green) loadings plots for the $F_{\gamma IND}$ PLS model

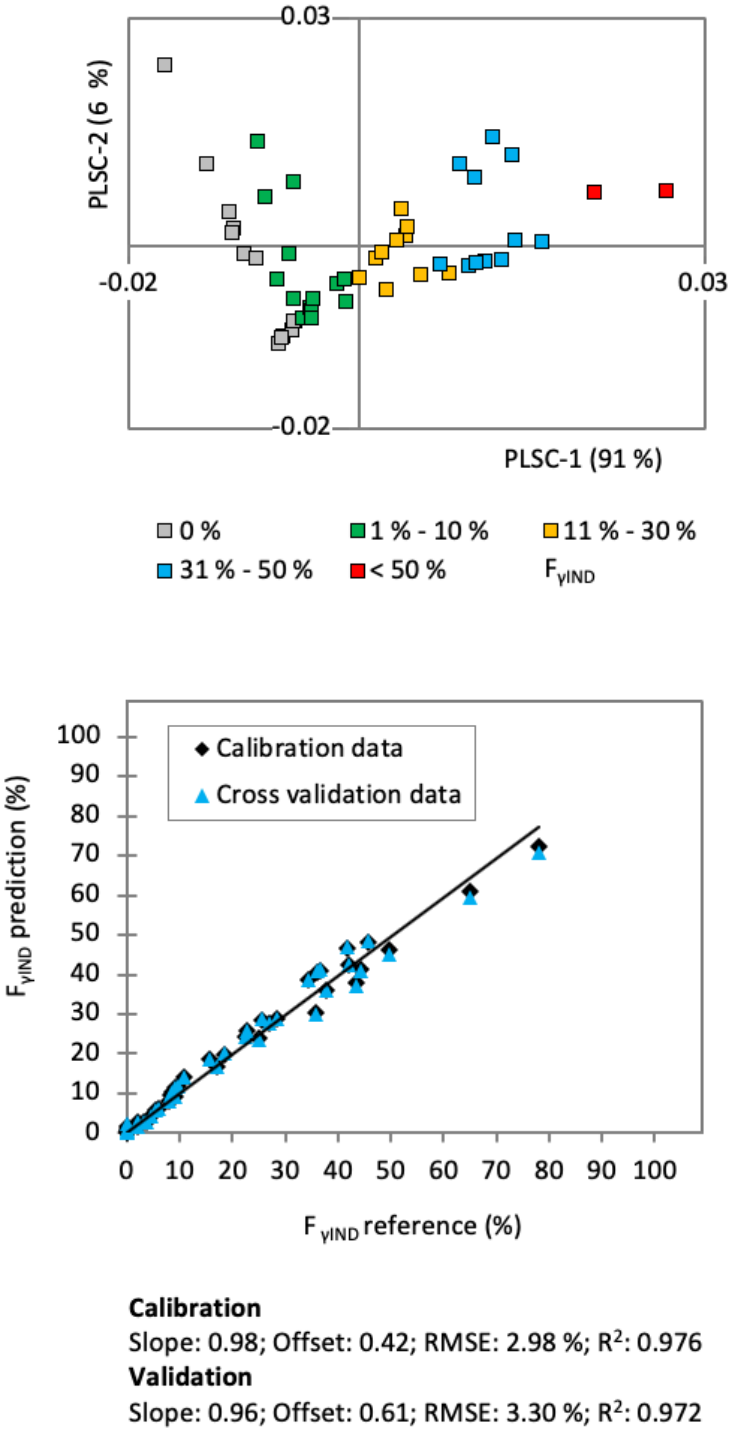

Fig. 43: PLSC-1-vs-PLSC-2 scores plot (top), the different colors classify the calibration samples according to their γ-IND fractions.

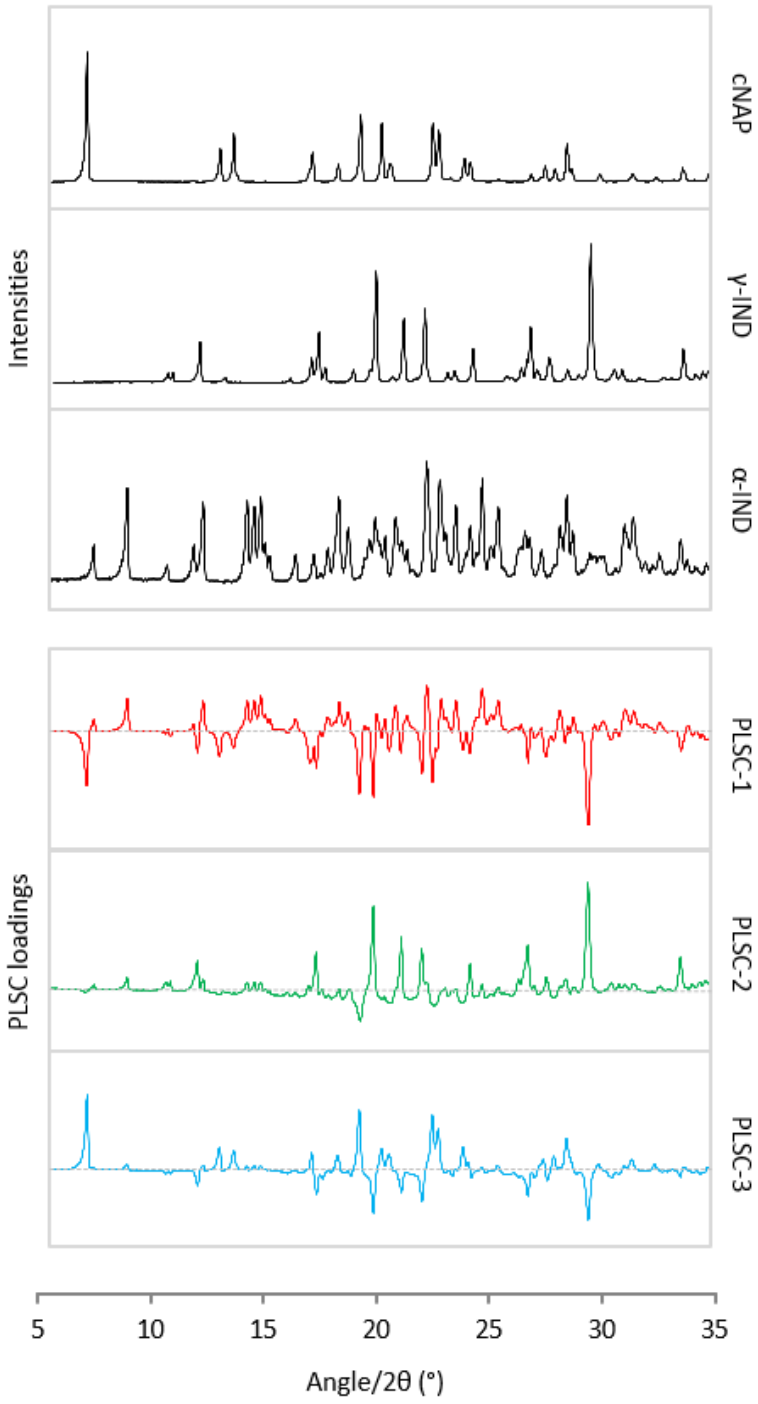

Fig. 44: Reference diffractograms of cNAP, γ-IND, α-IND and PLSC-1 (red), PLSC-2 (green) and PLSC-3 (blue) loadings plots for the $F_{\alpha\text{-IND}}$ PLS model

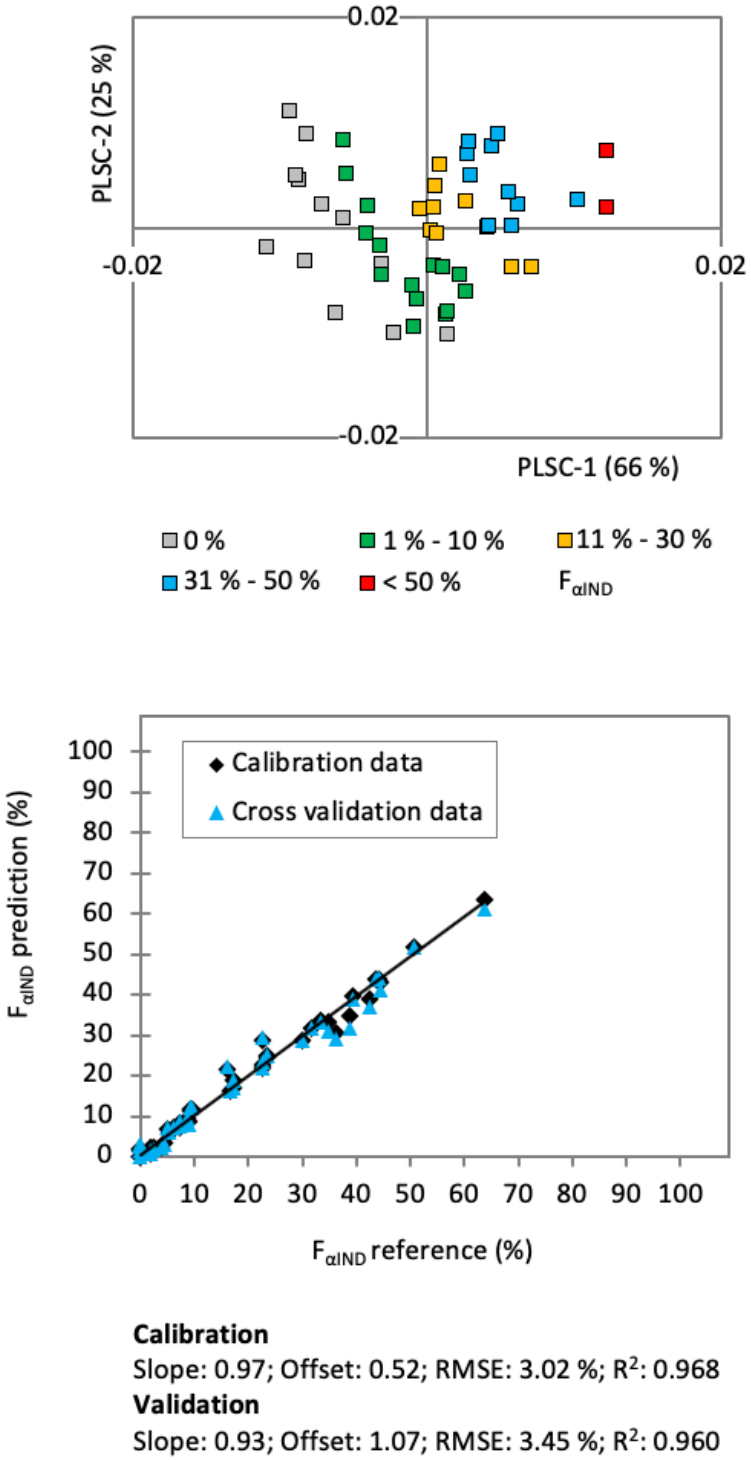

Fig. 45: PLSC-1-vs-PLSC-2 score plot (top), the different colors classify the calibration samples according to their α-IND fractions. Correlation of the PLS predicted α-IND fraction versus the reference values (bottom) during the calibration (black diamonds) and cross validation (blue triangles)

5.4.5 **Total molar amorphous fraction F_{am}**

With decreasing peak intensities of the crystalline components in the XRPD data, the shape of the processed diffractograms changes towards a halo, representing amorphous samples. Based on this fact, it was investigated if the total molar amorphous fraction F_{am} may be directly quantifiable by construction of a fourth PLS model.

Again, three PLSCs were found to describe 97 % of the variability of the total molar amorphous fraction in the calibration set. In Fig. 46, the loadings plots of the first three PLSCs are shown. PLSC-1 (65 %) distinguishes halo and α-IND diffraction signals (positive part) from γ-IND and cNAP intensities (negative part), while PLSC-2 (23 %) separates γ-IND and halo diffraction signals (positive part) from α-IND and cNAP intensities (negative part). Therefore, samples with high amorphous fractions cluster in the positive parts of both PLSCs in the PLSC-1-vs-PLSC-2 scores plot (Fig. 47). PLSC-3 (9 %) distinguishes some halo and cNAP signals (positive part) from α-IND signals (negative part) and thus further specifies the co-amorphous fraction in the samples.

Comparison of the PLS predicted amorphous fractions versus the true values (Fig. 47) reveals linearity between 10 and 100 %. For fully crystalline calibration samples that contain exclusively cNAP, γ-IND or α-IND the amorphous fractions were strongly overestimated to up to 20 % and therefore, PLS predicted F_{am} values near or below 20 % have to be considered carefully. The F_{am} PLS model is thus not applicable for fully crystalline samples. To exclude the presence of fully crystalline samples, the respective diffractograms should be checked for the presence of a halo signal. The R^2 (0.966) and RMSE (4.97 %) are slightly different compared to those of the other models. However, as XRPD as a measurement technique is best suited to describe the crystallinity of a sample, this is expected and the obtained model for the quantification of an amorphous phase can still be regarded as very good. The descriptors again change moderately during the cross validation (R^2: 0.959; RMSE: 5.57 %).

The PLS model for the prediction of the amorphous contents can by verified by comparing the obtained values of this model with remains of the sum of the crystalline models (indirect prediction). For comparison, the indirectly predicted values for F_{am} according to Equation 14 are plotted versus the reference fractions in Fig. 48.

$$F_{am}=100-(F_{cNAP}+F_{\gamma IND}+F_{\alpha IND}) \qquad \text{Equation 14}$$

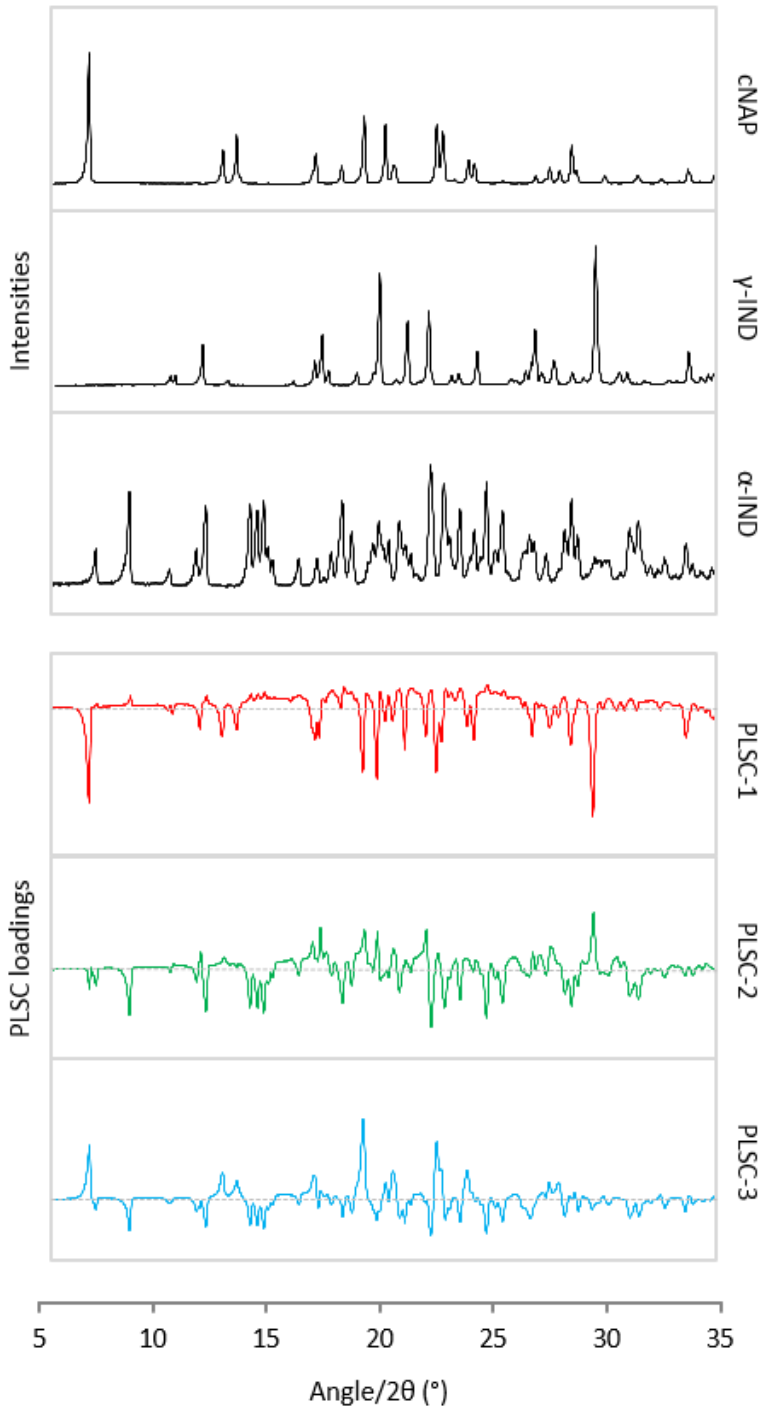

Fig. 46: Reference diffractograms of cNAP, γ-IND, α-IND and PLSC-1 (red), PLSC-2 (green) and PLSC-3 (blue) loadings plots for the F_{am} PLS model

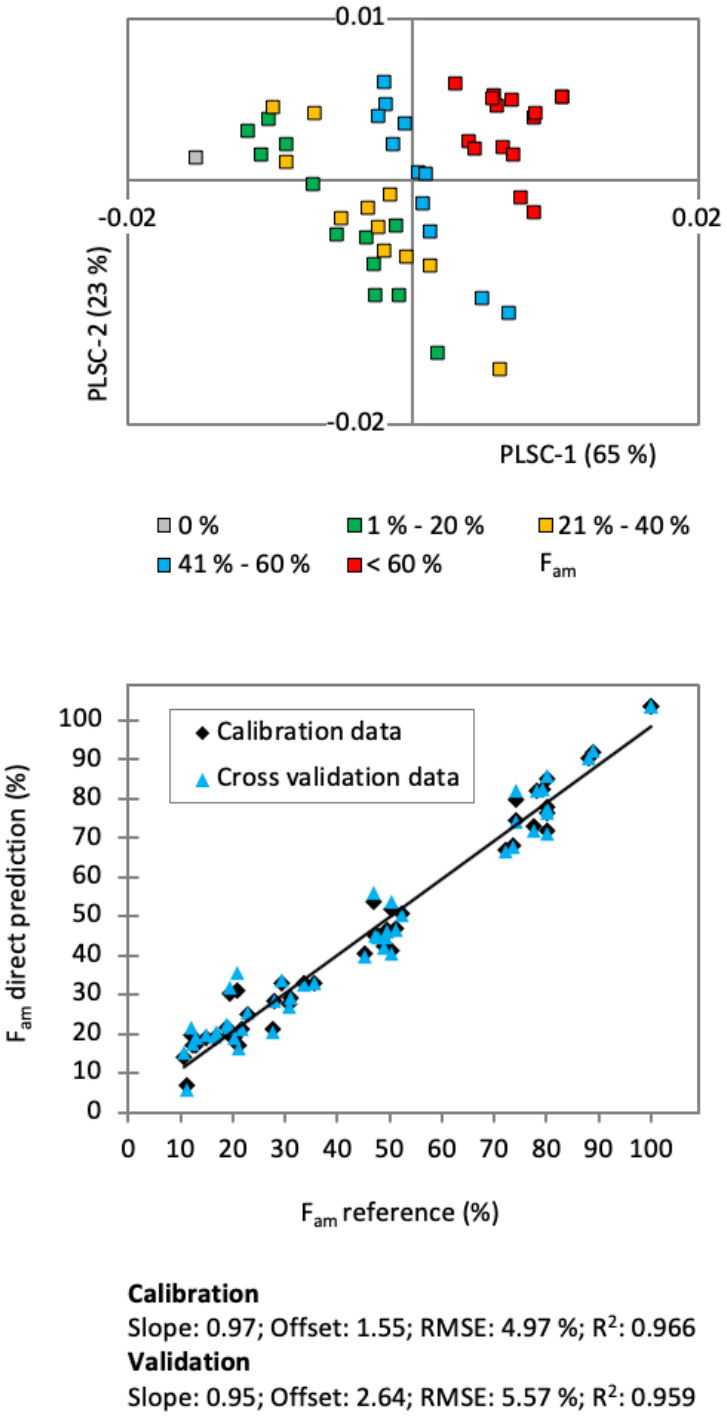

Fig. 47: PLSC-1-vs-PLSC-2 scores plot (top), the different colors classify the calibration samples according to their amorphous fractions. Correlation of the PLS predicted amorphous fraction versus the reference values (bottom) during the calibration (black diamonds) and cross validation (blue triangles).

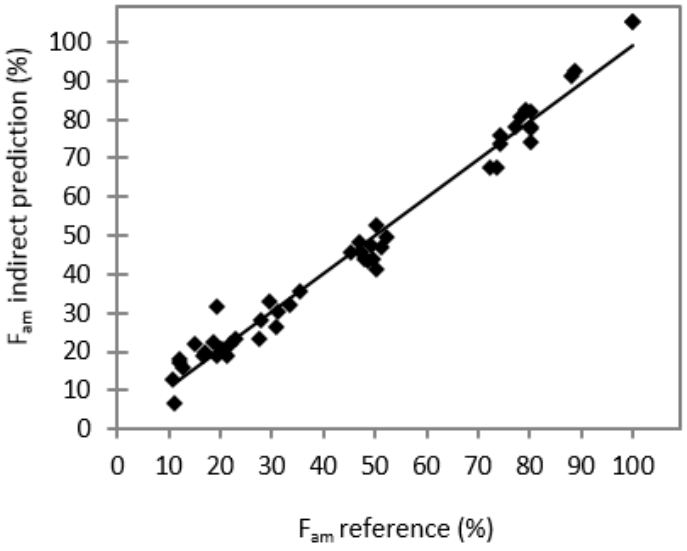

Fig. 48: Correlation of the indirectly predicted amorphous fraction versus the reference values.

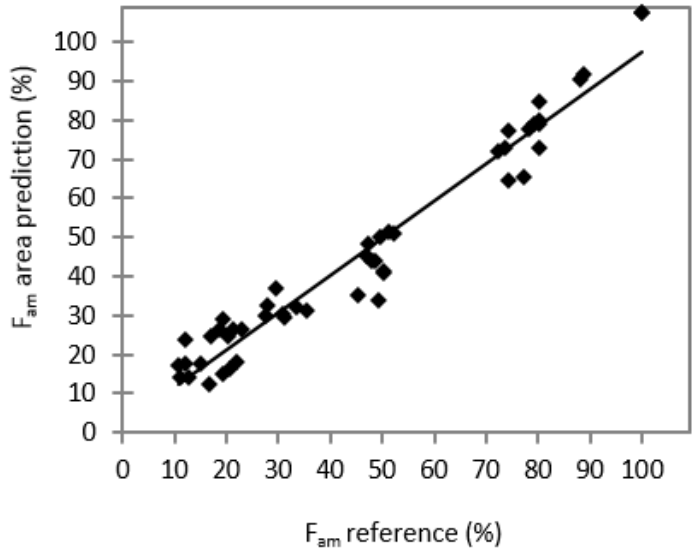

Fig. 49: Correlation of the predicted amorphous fractions based on the relative area under the Bragg peaks versus the reference values.

It can be seen that both methods deliver comparable results, although the indirect approach is slightly more accurate (R^2: 0.978; RMSE: 3.97 %), as could have been expected based on the principle of the measurement technique.

For comparison, F_{am} was also predicted based on the relative area ($A_{\%}$) under the Bragg peaks in the diffractograms. Correlation of the true F_{am} values of the calibration samples versus the predicted $A_{\%}$ values and linear regression resulted in a calibration function. The predicted values for F_{am} using the calibration function are plotted versus the reference fractions in Fig. 49. R^2 (0.953) and the RMSE (5.87 %) were slightly worse compared to the results of the other two approaches.

5.4.6 **Conclusion**

The presented results show that the X-ray powder diffractometry (XRPD) data-based multivariate quantification of up to four simultaneously present solid state phases involving three crystalline and one co-amorphous phase is possible by application of one partial least square (PLS) regression model for each of the four phases. The root mean square errors (RMSE) during the leave-one-out cross validations for the predictions of the crystalline components in the linear areas are found to be between 3.11 and 3.45 % and are thus comparable to results reported for the determination of one crystalline phase in binary mixtures with an amorphous phase [123] and for the quantification of the fractions in quaternary mixtures involving exclusively crystalline compounds [105]. Furthermore, PLS prediction of the co-amorphous fraction in the calibration samples was also possible with a slightly increased RMSE of 5.57 %. In a future study, based on the present PLS models, the recrystallization behavior of co-amorphous naproxen/indomethacin in dependence of the composition of the co-amorphous phase and the preparation method will be investigated.

6 Materials[5]

Crystalline naproxen (cNAP, M = 230.26 g/mol) and crystalline γ-indomethacin (γ-IND, M = 357.79 g/mol) were purchased from Fagron (Barsbüttel, Germany) and used as received.

[5] Parts of this chapter have been published as shown under 8.2 in the appendix.

Crystalline naproxen sodium (cNS, M = 252.24 g/mol) was kindly provided by Bayer (Leverkusen, Germany) and used as received.

The α-indomethacin (α-IND) polymorph was prepared by precipitation from an ethanolic solution by addition of water according to Atef et al. [100] before vacuum-drying (P_2O_5) and sieving (250 µm).

Acetone (99.8 %) was purchased from VWR (Radnor, USA).

7 Methods[6]

7.1 Sample preparation, processing and storage

7.1.1 Spray-dried samples

Spray-drying was performed with a Mini Spray Dryer B-290, equipped with the Inert Loop B-295, a high-performance cyclone (all three from Büchi, Flawil, Switzerland) and an external Ismatec Reglo Analog peristaltic pump (IDEX Health and Science, Glattbrugg, Germany). Nitrogen was used as atomizing gas [101]. For each spray-drying run, 5 g powder consisting of cNAP and γ-IND at an equimolar ratio were dissolved in 50 ml of acetone. During all runs, the parameters atomizing gas feed and aspirator rate were kept constant at their maximum levels of 100 %, respectively. The pump feed rate (PFR) and inlet temperature were varied both according to a 2^2 full factorial design including a center point, resulting in five combinations of process conditions. Three spray-drying runs were performed separately at each of these five process conditions (Table 7).

Table 7: Overview of the spray-drying process conditions.

Sample name	150/0.3	150/3.0	100/1.5	50/0.3	50/3.0
Inlet temperature (°C)	150	150	100	50	50
Pump feed rate (ml/min)	0.3	3.0	1.5	0.3	3.0
Mean outlet temperature (°C)	71.5 ± 1.5	68.0 ± 3.8	48.0 ± 7.8	33.5 ± 3.3	30.8 ± 0.3
Process duration (min)	150	15	30	150	15

[6] Parts of this chapter have been published as shown under 8.2 in the appendix.

The obtained product was gently mixed with mortar and pestle and subsequently stored for up to 28 d in a desiccator in open sample tubes under dry conditions over phosphorous pentoxide and 21 °C in an air-conditioned room. Analysis was performed after 0, 7, 14 and 28 d of storage.

7.1.2 **Differently cooled samples**

An amount of 1g of equimolar co-amorphous naproxen/indomethacin (NAP/IND) was prepared in triplicate by melting the equimolar physical mixture of cNAP and γ-IND at 170 °C for 10 min and applying three different cooling methods: Fast cooling (FC): Liquid nitrogen (N_2) was poured onto the melts, which were subsequently transferred into a P_2O_5 desiccator. After the N_2 was fully evaporated while displacing the present air through a hole to avoid moisture sorption, the hole was closed until the samples reached room temperature again. Intermediate cooling (IC): Within a P_2O_5 desiccator, the melts cooled down to room temperature. Slow cooling (SC): The samples were covered with aluminum foil, transferred into a HAAKE C25P thermostat (Thermo Fisher, Waltham, USA) and cooled down to room temperature within 180 min.

The differently prepared samples were homogenized, particle size-reduced and sieved (250 µm) in an air-conditioned room at 6 °C by mortar and pestle before they were stored in open sample tubes within desiccators (21 °C, P_2O_5). The differently cooled samples were stored for up to 300 days while sampling was performed after 0, 56, 112 and 300 days. The samples at different naproxen molar fractions were stored for up to 112 days and analyzed after 0, 56 and 112 days.

7.1.3 **Samples at different molar ratios**

1g of each of the respective physical mixtures was molten at 170 °C for 10 min and subsequently cooled down to room temperature inside a desiccator above P_2O_5 using the IC approach as described above. Ten different NAP/IND blends with the following naproxen molar fractions (NMFs) were prepared in triplicate: 0.1, 0.2, 0.3, 0.4, 0.5, 0.55, 0.6, 0.7, 0.8, 0.9.

The differently prepared samples were homogenized, particle size-reduced and sieved (250 µm) in an air-conditioned room at 6 °C by mortar and pestle before they were stored in open sample tubes within desiccators (21 °C, P_2O_5). The differently cooled samples were stored for up to 300 days while sampling was performed after 0, 56, 112 and 300 days. The samples at different naproxen molar fractions were stored for up to 112 days and analyzed after 0, 56 and 112 days.

7.1.4 **Samples that contain naproxen-sodium**

Different binary and ternary physical mixtures comprising cNAP, cNS and γ-IND were prepared according to Table 8.

Table 8: Molar compositions of the prepared samples

	Components	Molar composition								
NI	Naproxen (N)	0.1	0.2	0.3	0.4	0.5	0.6	0.7	0.8	0.9
	Indomethacin (I)	0.9	0.8	0.7	0.6	0.5	0.4	0.3	0.2	0.1
NSI	Naproxen-sodium (NS)	0.1	0.2	0.3	0.4	0.5	0.6	0.7	0.8	0.9
	Indomethacin (I)	0.9	0.8	0.7	0.6	0.5	0.4	0.3	0.2	0.1
NSNI	Naproxen-sodium (NS)	0.05	0.1	0.15	0.2	0.25	0.3	0.35	0.4	0.45
	Naproxen (N)	0.05	0.1	0.15	0.2	0.25	0.3	0.35	0.4	0.45
	Indomethacin (I)	0.9	0.8	0.7	0.6	0.5	0.4	0.3	0.2	0.1

The different physical mixtures were molten for 10 min using an oil bath at 180 °C and subsequently cooled down to room temperature over P_2O_5 in a desiccator at ambient conditions, because in chapter 5.2.1 it has been shown that this cooling method leads to the physically most stable NI samples. The data for the NI systems were obtained during the study in chapter 5.2.1 [66].

In an air-conditioned room (6 °C), homogenization and particle size-reduction was performed using mortar and pestle followed by sieving (250 µm) before the samples were stored in open sample tubes within closed desiccators (21 °C, P_2O_5) for up to 270 d.

7.1.5 **Preparation of the calibration set**

The calibration set has to cover various possible quantitative combinations of the four solid state phases. Binary, ternary and quaternary physical blends comprising cNAP, γ-IND, α-IND and aNAP/$IND_{1:1}$ were prepared. For each of the 52 calibration samples, a total mass of 300 mg with varying molar ratios according to Fig. 50 was directly weighed into ball-milling steel jars.

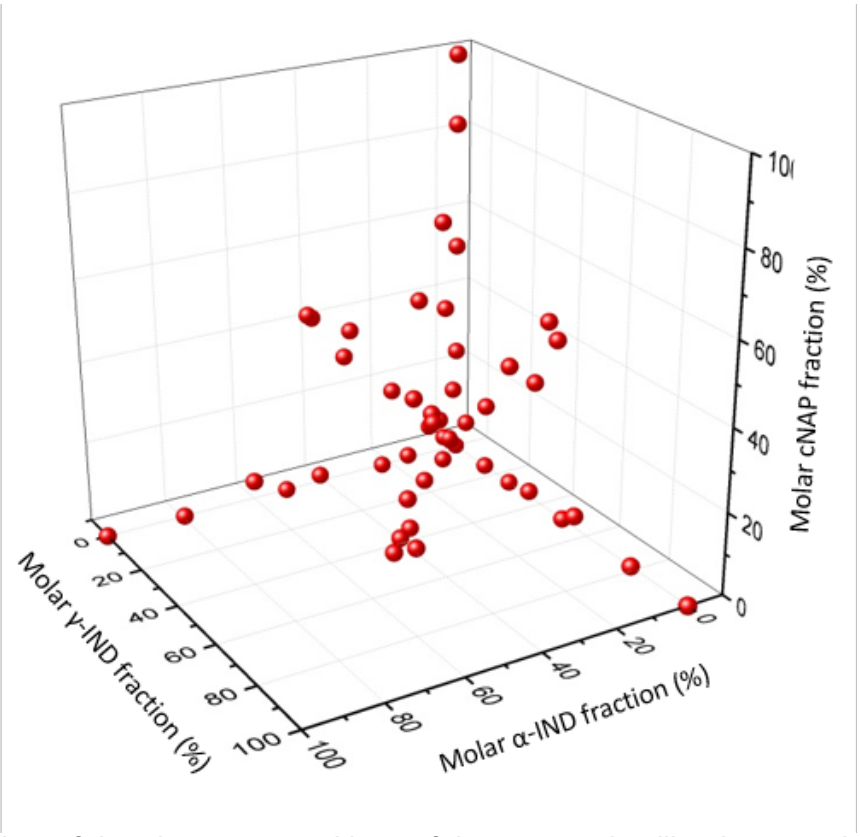

Fig. 50: Overview of the phase compositions of the prepared calibration samples containing binary, ternary and quaternary blends of cNAP, γ-IND, α-IND and aNAP/IND1:1.

Subsequently, three steel balls with 5 mm diameter were added to the powders before the filled jars were transferred into a freezer at -18°C for 10 min. This was necessary to ensure that the temperature of the solid was below the glass transition temperature of the co-amorphous portion of the samples, hereby avoiding problems such as suboptimal mixing and incomplete recovery of the powders due to the sticky character of aNAP/IND above its Tg.

Immediately thereafter, the cooled milling jars were attached to a Retsch MM 200 ball mill (Retsch GmbH, Haan, Germany) and blending was performed at 10 Hz for 1 min until a homogeneous powder was obtained. The powders were transferred into glass tubes. To ensure that no crystalline-to-amorphous or amorphous-to-crystalline transformations of the compounds occur during the blending process, 300 mg of each plain compound was treated in the same manner as the calibration samples. Comparison of the diffractograms of treated and untreated samples revealed no differences (data not shown).

7.2 Karl-Fischer analysis

Determination of the water content was carried out by coulometric Karl-Fischer analysis with 20-30 mg of each sample with a Mettler Toledo DL37 KF Coulometer (Mettler Toledo, Columbus, USA).

7.3 Thermogravimetric analysis

To determine the residual acetone content in the spray-dried samples, TGA was performed under isothermal conditions for 2 h at 100 °C with approximately 50 mg of each of the 15 freshly prepared samples using a Pyris 1 TGA (Perkin Elmer, Waltham, USA).

7.4 Differential scanning calorimetry

DSC analysis was performed using a DSC 1 (Mettler Toledo, Columbus, USA). An amount of 10-20 mg of each of the samples was weighed into aluminum pans which were subsequently closed with pierced lids. For analysis, samples were scanned within a temperature range of -50 to 180 °C at a heating rate of 10 °C / min. Data was analyzed using STARe Software (Mettler Toledo, Columbus, USA). For in situ preparation, the respective physical mixtures (5.3.1) were heated up to 180 °C and subsequently cooled down to – 50 °C at a cooling rate of 20 °C/min.

7.5 Fourier-transformed infrared spectroscopy

Infrared spectra were recorded over a range of 4000 – 400 cm^{-1} (128 scans, resolution 4 cm^{-1}) with a Tensor 37 spectrometer and the Opus software v.7 (Bruker Optik GmbH, Ettlingen, Germany) equipped with a MIRacle attenuated total reflectance device with diamond crystal plate (Piketech, Madison, USA). Before data analysis, baseline correction and normalization to unit area was performed for all spectra using The Unscrambler X software (ver. 10.3, Camo Software, Oslo, Norway). Either the spectral region between 1600 and 1800 cm^{-1} [65] or 1000 and 1800 cm^{-1} was chosen for analysis.

7.6 X-ray powder diffractometry

For XRPD analysis, samples were placed onto an aluminium sample holder and gently compressed with a glass plate to obtain a compact powder with a flat surface. XRPD analysis was performed using an X'Pert PRO X-ray diffractometer (PANalytical, Almelo, The Netherlands; Cu Kα anode; λ = 1.5406 Å; 45 kV; 40 mA). Samples were scanned in reflection mode between 5 and 35 °2θ with a scan speed of 0.045 °2θ /min and a step size of 0.0131 °2θ. All obtained diffractograms were baseline offset corrected and normalized to unit area [102] using The Unscrambler X software (ver. 10.3, Camo Software, Oslo, Norway).

In chapter 5.2.1 Savitzky-Golay smoothing was performed with the diffractograms (polynomial order: 1; 9 smoothing points) for better visualization. This was performed by The Unscrambler X software (ver. 10.3, Camo Software, Oslo, Norway).

For chapter 5.4 duplicate diffractograms were recorded. The diffractograms were corrected for systematic peak shifts along the °2θ axis before averaging was performed using Microsoft Excel. For the determination of the area under the Bragg peaks, the background determination function in the Highscore Plus software (ver. 2.2e, Panalytical, Almelo, The Netherlands) was used.

7.7 **Intrinsic Dissolution**

To compare the intrinsic dissolution rate of the NI and NSI samples, 200 mg of the respective equimolar co-amorphous powders were compressed (in triplicate) for 10 seconds at a pressure of 150 MPa using a hydraulic Specac IR press.

The equimolar compacted NI powders consisted of about 39.2 % and 60.8 % (m/m) NAP and IND respectively, which is slightly different to the equimolar NSI system, which contained about 41.3 and 58.7 % (m/m) NS and IND, respectively. Taking the densities of NAP (1.265 g/cm^3; [65]), IND (1.379 g/cm^3; [65]) and NS (1.35 g/cm^3; [104]) into account, the resulting (theoretical) volume fraction in the compacts that is occupied by NAP and IND can be calculated: NI: 41.2 % NAP and 58.8 % IND; NSI: 41.9 % NS and 58.1 % IND. Assuming a homogenous distribution of NAP and IND in the whole compact, the surface composition is almost identical in both systems and thus the respective dissolution data are directly comparable.

The obtained discs with a surface area of 1.2 cm^2 were attached to an intrinsic dissolution sample holder, which was subsequently transferred to a rotating paddle apparatus, that was filled with 750 ml of 0.1 M phosphate buffer (pH 7.4; 25 °C; 50 rpm). After 5, 10, 20, 30 and 60 minutes, sampling was performed for about 60 seconds from a fixed position above the rotating paddle using a hose pump until 5 ml of the respective solutions were collected. The collected volume was simultaneously exchanged by the same amount of 0.1 M phosphate buffer solution (pH 7.4; 25 °C). 5 µl phosphoric acid was added to 4 ml of the collected solution to reach a pH of 1 and to make sure that NAP and IND are present in their respective acid forms. Subsequently, the solution was diluted to 10 ml with acetonitrile. 20 µl of each of the resulting solutions were injected into a VWR Hitachi Chromaster (Radnor, USA). As elution solvent, 60 % acetonitrile + 40 % H_2O at a flow rate of 2 ml/min was used. The detection wavelengths were set to 232 nm (for NAP) and 202 nm (for IND), respectively. The resulting data was collected using Chromaster System Manager software (v.1.1, Hitachi, Radnor, USA).

7.8 Multivariate data analysis

7.8.1 Principal component analysis

Principal component analysis (PCA) was performed with the baseline offset corrected and area normalized FTIR spectra and X-ray powder diffractograms using the Unscrambler X software (ver. 10.3, Camo Software, Oslo, Norway).

7.8.2 Partial least squares regression

Multivariate PLS regression was chosen to quantify each of the molar fractions in the quaternary blends based on XRPD data in chapter XY. This projection method is able to extract the most relevant information of a given dataset by reduction of its dimensionality. An XRPD file usually presents a vector with N columns according to the number of scattering angles, while each column contains the respective XRPD signal intensity that was measured. Thus, a given dataset with p XRPD files results in an X-matrix of p x N variables. To apply PLS, a PLS model that is based on calibration samples has to be constructed. For each diffractogram of the calibration set, the responses (the molar fractions) have to be known. These responses will then form the Y-matrix. PLS now detects the most important components in the data matrix by maximizing the covariance between the X- and Y-matrix [105]. For the construction of a PLS model, it is important to choose the correct number of PLS components to be included in the model. A too small number of PLS components will lead to a poor model performance, while too many PLS components would result in overfitting [106]. To determine the optimal number of PLS components, the method provided by The Unscrambler X software was used, which is based on the minimization of the root mean square error of validation [106,107].

7.8.2.1 Cross validation of the PLS models

To determine the predictive quality of the PLS models, leave-one-out cross validation was performed for the PLS calibration set using The Unscrambler X software. Hereby, the 52-samples PLS calibration set was separated into a 51-samples training set and the test sample. The construction of the PLS models was performed based on the training dataset and subsequently the test sample was predicted based on these PLS models. This procedure was repeated 52 times until each sample was left out once [106]. Finally, all predictions were combined to calculate R^2 and the RMSE.

8 References

1. Lipinski, C. A. Drug-like properties and the causes of poor solubility and poor permeability, Journal of pharmacological and toxicological methods 1 (2000) 235–249.

2. Ku, M. Sherry.Dulin, W. A biopharmaceutical classification-based Right-First-Time formulation approach to reduce human pharmacokinetic variability and project cycle time from First-In-Human to clinical Proof-Of-Concept, Pharmaceutical Development and Technology 3 (2012) 285–302.

3. Kawabata, Y.; Wada, K.; Nakatani, M.; Yamada, S.Onoue, S. Formulation design for poorly water-soluble drugs based on biopharmaceutics classification system: Basic approaches and practical applications, International Journal of Pharmaceutics 1 (2011) 1–10.

4. Amidon, G. L.; Lennernäs, H.; Shah, V. P.Crison, J. R. A theoretical basis for a biopharmaceutic drug classification: the correlation of in vitro drug product dissolution and in vivo bioavailability, Pharmaceutical Research 3 (1995) 413–420.

5. Hörter, D.Dressman, J. B. Influence of physicochemical properties on dissolution of drugs in the gastrointestinal tract, Advanced drug delivery reviews 1 (2001) 75–87.

6. Löbenberg, R.Amidon, G. L. Modern bioavailability, bioequivalence and biopharmaceutics classification system. New scientific approaches to international regulatory standards, European Journal of Pharmaceutics and Biopharmaceutics 1 (2000) 3–12.

7. Mosharraf, M.Nyström, C. The effect of particle size and shape on the surface specific dissolution rate of microsized practically insoluble drugs, International Journal of Pharmaceutics 1-2 (1995) 35–47.

8. Müller, R. H.Peters, K. Nanosuspensions for the formulation of poorly soluble drugs: I. Preparation by a size-reduction technique, International Journal of Pharmaceutics 2 (1998) 229–237.

9. Shegokar, R.Müller, R. H. Nanocrystals: industrially feasible multifunctional formulation technology for poorly soluble actives, International Journal of Pharmaceutics 1 (2010) 129–139.

10. Schultheiss, N.Newman, A. Pharmaceutical cocrystals and their physicochemical properties, Crystal Growth and Design 6 (2009) 2950–2967.

11. Jung, M.; Kim, J.; Kim, M.; Alhalaweh, A.; Cho, W.; Hwang, S.Velaga, S. P. Bioavailability of indomethacin-saccharin cocrystals, Journal of Pharmacy and Pharmacology 11 (2010) 1560–1568.

12. McNamara, D. P.; Childs, S. L.; Giordano, J.; Iarriccio, A.; Cassidy, J.; Shet, M. S.; Mannion, R.; O'Donnell, E.Park, A. Use of a glutaric acid cocrystal to improve oral bioavailability of a low solubility API, Pharmaceutical Research 8 (2006) 1888–1897.

13. Rodríguez-Spong, B.; Price, C. P.; Jayasankar, A.; Matzger, A. J.Rodríguez-Hornedo, N. General principles of pharmaceutical solid polymorphism: a supramolecular perspective, Advanced drug delivery reviews 3 (2004) 241–274.

14. Blagden, N.; Matas, M. de; Gavan, P.York, P. Crystal engineering of active pharmaceutical ingredients to improve solubility and dissolution rates, Advanced Drug Delivery Reviews 7 (2007) 617–630.

15. Pudipeddi, M.Serajuddin, A. Trends in solubility of polymorphs, Journal of Pharmaceutical Sciences 5 (2005) 929–939.

16. Kramer, S. F.Flynn, G. L. Solubility of organic hydrochlorides, Journal of Pharmaceutical Sciences 12 (1972) 1896–1904.

17. Craig, Duncan Q. M; Royall, P. G.; Kett, V. L.Hopton, M. L. The relevance of the amorphous state to pharmaceutical dosage forms: glassy drugs and freeze dried systems, International Journal of Pharmaceutics 2 (1999) 179–207.

18. Hancock, B. C.Zografi, G. Characteristics and significance of the amorphous state in pharmaceutical systems, Journal of Pharmaceutical Sciences 1 (1997) 1–12.

19. Kawakami, K.Pikal, M. J. Calorimetric investigation of the structural relaxation of amorphous materials: Evaluating validity of the methodologies, Journal of Pharmaceutical Sciences 5 (2005) 948–965.

20. Yu, L. Amorphous pharmaceutical solids: preparation, characterization and stabilization, Advanced Drug Delivery Reviews 1 (2001) 27–42.

21. Hancock, B. C.Parks, M. What is the true solubility advantage for amorphous pharmaceuticals?, Pharmaceutical Research 4 (2000) 397–404.

22. Bhugra, C.; Shmeis, R.Pikal, M. J. Role of mechanical stress in crystallization and relaxation behavior of amorphous indomethacin, Journal of Pharmaceutical Sciences 10 (2008) 4446–4458.

23. Hancock, B. C.; Shamblin, S. L.Zografi, G. Molecular mobility of amorphous pharmaceutical solids below their glass transition temperatures, Pharmaceutical Research 6 (1995) 799–806.

24. Miyazaki, T.; Yoshioka, S.; Aso, Y.Kawanishi, T. Crystallization rate of amorphous nifedipine analogues unrelated to the glass transition temperature, International Journal of Pharmaceutics 1 (2007) 191–195.

25. Yoshioka, M.; Hancock, B. C.Zografi, G. Crystallization of indomethacin from the amorphous state below and above its glass transition temperature, Journal of Pharmaceutical Sciences 12 (1994) 1700–1705.

26. Kaushal, A. Mohan.Bansal, A. Kumar. Thermodynamic behavior of glassy state of structurally related compounds, European Journal of Pharmaceutics and Biopharmaceutics 3 (2008) 1067–1076.

27. Zhou, D.; Zhang, G. G.; Law, D.; Grant, David J. W.Schmitt, E. A. Physical stability of amorphous pharmaceuticals: Importance of configurational thermodynamic quantities and molecular mobility, Journal of Pharmaceutical Sciences 8 (2002) 1863–1872.

28. Hancock, B. C.; Shalaev, E. Y.Shamblin, S. L. Polyamorphism: a pharmaceutical science perspective, Journal of Pharmacy and Pharmacology 8 (2002) 1151–1152.

29. Ayenew, Z.; Paudel, A.van den Mooter, G. Can compression induce demixing in amorphous solid dispersions? A case study of naproxen–PVP K25, European Journal of Pharmaceutics and Biopharmaceutics 1 (2012) 207–213.

30. Chiou, W. Loung.Riegelman, S. Pharmaceutical applications of solid dispersion systems, Journal of Pharmaceutical Sciences 9 (1971) 1281–1302.

31. Janssens, S.van den Mooter, G. Review: physical chemistry of solid dispersions, Journal of Pharmacy and Pharmacology 12 (2009) 1571–1586.

32. Matsumoto, T.Zografi, G. Physical properties of solid molecular dispersions of indomethacin with poly (vinylpyrrolidone) and poly (vinylpyrrolidone-co-vinyl-acetate) in relation to indomethacin crystallization, Pharmaceutical Research 11 (1999) 1722–1728.

33. Serajuddin, Abu T. M. Salt formation to improve drug solubility, Advanced Drug Delivery Reviews 7 (2007) 603–616.

34. Srinarong, P.; Waard, H. de; Frijlink, H. W.Hinrichs, W. L. Improved dissolution behavior of lipophilic drugs by solid dispersions: the production process as starting point for formulation considerations, Expert Opinion on Drug Delivery 9 (2011) 1121–1140.

35. Shrivastava, A. R.; Ursekar, B.Kapadia, C. J. Design, optimization, preparation and evaluation of dispersion granules of valsartan and formulation into tablets, Current Drug Delivery 1 (2009) 28–37.

36. Kaur, R.; Grant, D. J.W.Eaves, T. Comparison of polyethylene glycol and polyoxyethylene stearate as excipients for solid dispersion systems of griseofulvin and tolbutamide II, Journal of Pharmaceutical Sciences 11 (1980) 1321–1326.

37. Sjökvist, E.Nyström, C. Physicochemical aspects of drug release. XI. Tableting properties of solid dispersions, using xylitol as carrier material, International Journal of Pharmaceutics 2 (1991) 139–153.

38. Andronis, V.; Yoshioka, M.Zografi, G. Effects of sorbed water on the crystallization of indomethacin from the amorphous state, Journal of Pharmaceutical Sciences 3 (1997) 346–351.

39. Ford, J. L.Rubinstein, M. H. Preparation, properties and ageing of tablets prepared from the chlorpropamide-urea solid dispersion, International Journal of Pharmaceutics 4 (1981) 311–322.

40. Akbuga, J.; Gürsoy, A.Yetimoĝlu, F. Preparation and properties of tablets prepared from furosemide-PVP solid dispersion systems, Drug Development and Industrial Pharmacy 15-17 (1988) 2091–2108.

41. Ford, J. L. The current status of solid dispersions, Pharmaceutica Acta Helvetiae 3 (1985) 69–88.

42. Dordunoo, S. K.; Ford, J. L.Rubinstein, M. H. Preformulation studies on solid dispersions containing triamterene or temazepam in polyethylene glycols or Gelucire 44/14 for liquid filling of hard gelatin capsules, Drug Development and Industrial Pharmacy 12 (1991) 1685–1713.

43. Rosoff, M.Serajuddin, Abu T. M. Solubilization of diazepam in bile salts and in sodium cholate-lecithin-water phases, International Journal of Pharmaceutics 2 (1980) 137–146.

44. Qian, K. K.Bogner, R. H. Application of mesoporous silicon dioxide and silicate in oral amorphous drug delivery systems, Journal of Pharmaceutical Sciences 2 (2012) 444–463.

45. Sing, K. S. Reporting physisorption data for gas/solid systems with special reference to the determination of surface area and porosity (Recommendations 1984), Pure and applied Chemistry 4 (1985) 603–619.

46. Bahl, D.Bogner, R. H. Amorphization of indomethacin by co-grinding with Neusilin US2: amorphization kinetics, physical stability and mechanism, Pharmaceutical Research 10 (2006) 2317–2325.

47. Bahl, D.Bogner, R. H. Amorphization alone does not account for the enhancement of solubility of drug co-ground with silicate: The case of indomethacin, AAPS PharmSciTech 1 (2008) 146–153.

48. Bahl, D.; Hudak, J.Bogner, R. H. Comparison of the ability of various pharmaceutical silicates to amorphize and enhance dissolution of indomethacin upon co-grinding, Pharmaceutical Development and Technology 3 (2008) 255–269.

49. NAKAI, Y.; Yamamoto, K.; Terada, K.ICHIKAWA, J. Interaction of medicinals and porous powder. I. Anomalous thermal behavior of porous glass mixtures, Chemical and pharmaceutical bulletin 11 (1984) 4566–4571.

50. KONNO, T.; KINUNO, K.KATAOKA, K. Physical and chemical changes of medicinals in mixtures with adsorbents in the solid state. I.: Effect of vapor pressure of the medicinals on changes in crystalline properties, Chemical and pharmaceutical bulletin 1 (1986) 301–307.

51. Limnell, T.; Santos, H. A.; Mäkilä, E.; Heikkilä, T.; Salonen, J.; Murzin, D. Yu; Kumar, N.; Laaksonen, T.; Peltonen, L.Hirvonen, J. Drug delivery formulations of ordered and nonordered mesoporous silica: comparison of three drug loading methods, Journal of Pharmaceutical Sciences 8 (2011) 3294–3306.

52. Qian, K. K.; Suib, S. L.Bogner, R. H. Spontaneous crystalline-to-amorphous phase transformation of organic or medicinal compounds in the presence of porous media, part 2: Amorphization capacity and mechanisms of interaction, Journal of Pharmaceutical Sciences 11 (2011) 4674–4686.

53. Knopp, M. Manne; Tajber, L.; Tian, Y.; Olesen, N. Erik; Jones, D. S.; Kozyra, A.; Löbmann, K.; Paluch, K.; Brennan, C. Marie.Holm, R. Comparative study of different methods for the prediction of drug–polymer solubility, Molecular Pharmaceutics 9 (2015) 3408–3419.

54. Laitinen, R.; Löbmann, K.; Strachan, C. J.; Grohganz, H.Rades, T. Emerging trends in the stabilization of amorphous drugs, International Journal of Pharmaceutics 1 (2013) 65–79.

55. [Der Titel "Löbmann, Jensen et al. 2014 – Stabilized amorphous solid dispersions" kann nicht dargestellt werden. Die Vorlage "Literaturverzeichnis - Beitrag im Sammelwerk - (Standardvorlage)" enthält keine Informationen.]

56. Chieng, N.; Aaltonen, J.; Saville, D.Rades, T. Physical characterization and stability of amorphous indomethacin and ranitidine hydrochloride binary systems prepared by mechanical activation, European Journal of Pharmaceutics and Biopharmaceutics 1 (2009) 47–54.

57. Shamblin, S. L.Zografi, G. Enthalpy Relaxation in Binary Amorphous Mixtures Containing Sucrose, Pharmaceutical Research 12 (1998) 1828–1834.

58. Baird, J. A.Taylor, L. S. Evaluation of amorphous solid dispersion properties using thermal analysis techniques, Advanced drug delivery reviews 5 (2012) 396–421.

59. Shamblin, S. L.; Tang, X.; Chang, L.; Hancock, B. C.Pikal, M. J. Characterization of the time scales of molecular motion in pharmaceutically important glasses, The Journal of Physical Chemistry B 20 (1999) 4113–4121.

60. Löbmann, K.; Grohganz, H.; Laitinen, R.; Strachan, C.Rades, T. Amino acids as co-amorphous stabilizers for poorly water soluble drugs – Part 1: Preparation, stability and dissolution enhancement, European Journal of Pharmaceutics and Biopharmaceutics 3 Part B (2013) 873–881.

61. Jensen, K.; Löbmann, K.; Rades, T.Grohganz, H. Improving Co-Amorphous Drug Formulations by the Addition of the Highly Water Soluble Amino Acid, Proline, Pharmaceutics 3 (2014) 416–435.

62. Jensen, K. Tarp; Larsen, F. Hofmann; Cornett, C.; Löbmann, K.; Grohganz, H.Rades, T. Formation mechanism of coamorphous drug–amino acid mixtures, Molecular Pharmaceutics 7 (2015) 2484–2492.

63. Löbmann, K.; Laitinen, R.; Strachan, C.; Rades, T.Grohganz, H. Amino acids as co-amorphous stabilizers for poorly water-soluble drugs – Part 2: Molecular interactions, European Journal of Pharmaceutics and Biopharmaceutics 3 Part B (2013) 882–888.

64. Jensen, K. Tarp; Blaabjerg, L. Ingerslev; Lenz, E.; Bohr, A.; Grohganz, H.; Kleinebudde, P.; Rades, T.Löbmann, K. Preparation and characterization of spray-dried co-amorphous drug–amino acid salts, Journal of Pharmacy and Pharmacology (2015) n/a.

65. Löbmann, K.; Laitinen, R.; Grohganz, H.; Gordon, K. C.; Strachan, C.Rades, T. Coamorphous drug systems: enhanced physical stability and dissolution rate of indomethacin and naproxen, Molecular Pharmaceutics 5 (2011) 1919–1928.

66. Beyer, A.; Grohganz, H.; Löbmann, K.; Rades, T.Leopold, C. S. Influence of the cooling rate and the blend ratio on the physical stability of co-amorphous naproxen/indomethacin, European Journal of Pharmaceutics and Biopharmaceutics (2016) 140–148.

67. Song, S.-W.; Hidajat, K.Kawi, S. Functionalized SBA-15 materials as carriers for controlled drug delivery: influence of surface properties on matrix− drug interactions, Langmuir 21 (2005) 9568–9575.

68. Martínez, L. María; Videa, M.; López-Silva, G. A.; Carlos, A.; Cruz-Angeles, J.González, N. Stabilization of amorphous paracetamol based systems using traditional and novel strategies, International Journal of Pharmaceutics 1 (2014) 294–305.

69. Johari, G. P.; Kim, S.Shanker, R. M. Dielectric study of equimolar acetaminophen–aspirin, acetaminophen–quinidine, and benzoic acid–progesterone molecular alloys in the glass and ultraviscous states and their relevance to solubility and stability, Journal of Pharmaceutical Sciences 3 (2010) 1358–1374.

70. Yamamura, S.; Gotoh, H.; Sakamoto, Y.Momose, Y. Physicochemical properties of amorphous salt of cimetidine and diflunisal system, International Journal of Pharmaceutics 2 (2002) 213–221.

71. Yamamura, S.; Gotoh, H.; Sakamoto, Y.Momose, Y. Physicochemical properties of amorphous precipitates of cimetidine–indomethacin binary system, European Journal of Pharmaceutics and Biopharmaceutics 3 (2000) 259–265.

72. Masuda, T.; Yoshihashi, Y.; Yonemochi, E.; Fujii, K.; Uekusa, H.Terada, K. Cocrystallization and amorphization induced by drug–excipient interaction improves the physical properties of acyclovir, International Journal of Pharmaceutics 1 (2012) 160–169.

73. Gao, Y.; Liao, J.; Qi, X.Zhang, J. Coamorphous repaglinide–saccharin with enhanced dissolution, International Journal of Pharmaceutics 1 (2013) 290–295.

74. Tantishaiyakul, V.; Suknuntha, K.Vao-Soongnern, V. Characterization of cimetidine–piroxicam coprecipitate interaction using experimental studies and molecular dynamic simulations, AAPS PharmSciTech 2 (2010) 952–958.

75. Dengale, S. J.; Hussen, S. Sajjad; Krishna, B. S.M.; Musmade, P. B.; Shenoy, G. Gautham.Bhat, K. Fabrication, solid state characterization and bioavailability assessment of stable binary amorphous phases of Ritonavir with Quercetin, European Journal of Pharmaceutics and Biopharmaceutics (2015) 329–338.

76. Löbmann, K.; Laitinen, R.; Grohganz, H.; Strachan, C.; Rades, T.Gordon, K. C. A theoretical and spectroscopic study of co-amorphous naproxen and indomethacin, International Journal of Pharmaceutics 1 (2013) 80–87.

77. Lu, Q.Zografi, G. Phase behavior of binary and ternary amorphous mixtures containing indomethacin, citric acid, and PVP, Pharmaceutical Research 8 (1998) 1202–1206.

78. Hoppu, P.; Jouppila, K.; Rantanen, J.; Schantz, S.Juppo, A. M. Characterisation of blends of paracetamol and citric acid, Journal of Pharmacy and Pharmacology 3 (2007) 373–381.

79. Schantz, S.; Hoppu, P.Am Juppo. A solid-state NMR study of phase structure, molecular interactions, and mobility in blends of citric acid and paracetamol, Journal of Pharmaceutical Sciences 5 (2009) 1862–1870.

80. Qian, S.; Heng, W.; Wei, Y.; Zhang, J.Gao, Y. Coamorphous lurasidone hydrochloride–saccharin with charge-assisted hydrogen bonding interaction shows improved physical stability and enhanced dissolution with pH-independent solubility behavior, Crystal Growth & Design 6 (2015) 2920–2928.

81. Brostow, W.; Chiu, R.; Kalogeras, I. M.Vassilikou-Dova, A. Prediction of glass transition temperatures: binary blends and copolymers, Materials Letters 17 (2008) 3152–3155.

82. Painter, P. C.; Graf, J. F.Coleman, M. M. Effect of hydrogen bonding on the enthalpy of mixing and the composition dependence of the glass transition temperature in polymer blends, Macromolecules 20 (1991) 5630–5638.

83. Lu, X.Weiss, R. A. Relationship between the glass transition temperature and the interaction parameter of miscible binary polymer blends, Macromolecules 12 (1992) 3242–3246.

84. Löbmann, K.; Strachan, C.; Grohganz, H.; Rades, T.; Korhonen, O.Laitinen, R. Co-amorphous simvastatin and glipizide combinations show improved physical stability without evidence of intermolecular interactions, European Journal of Pharmaceutics and Biopharmaceutics 1 (2012) 159–169.

85. Dengale, S. J.; Ranjan, O. Prakash; Hussen, S. Sajjad; Krishna, B. S. M.; Musmade, P. B.; Gautham Shenoy, G.Bhat, K. Preparation and characterization of co-amorphous Ritonavir–Indomethacin systems by solvent evaporation technique: Improved dissolution behavior and physical stability without evidence of intermolecular interactions, European Journal of Pharmaceutical Sciences (2014) 57–64.

86. Kawakami, K. Modification of physicochemical characteristics of active pharmaceutical ingredients and application of supersaturatable dosage forms for improving bioavailability of poorly absorbed drugs, Advanced drug delivery reviews 6 (2012) 480–495.

87. Alonzo, D. E.; Zhang, G. G.; Zhou, D.; Gao, Y.Taylor, L. S. Understanding the Behavior of Amorphous Pharmaceutical Systems during Dissolution, Pharmaceutical Research 4 (2010) 608–618.

88. Heikkinen, A. T.; DeClerck, L.; Löbmann, K.; Grohganz, H.; Rades, T.Laitinen, R. Dissolution properties of co-amorphous drug-amino acid formulations in buffer and biorelevant media, Die Pharmazie-An International Journal of Pharmaceutical Sciences 7 (2015) 452–457.

89. Allesø, M.; Chieng, N.; Rehder, S.; Rantanen, J.; Rades, T.Aaltonen, J. Enhanced dissolution rate and synchronized release of drugs in binary systems through formulation: Amorphous naproxen–cimetidine mixtures prepared by mechanical activation, Journal of Controlled Release 1 (2009) 45–53.

90. Shayanfar, A.Jouyban, A. Drug–drug coamorphous systems: Characterization and physicochemical properties of coamorphous atorvastatin with carvedilol and glibenclamide, Journal of Pharmaceutical Innovation 4 (2013) 218–228.

91. Suresh, K.; Mannava, M. ChaitanyaK.Nangia, A. A novel curcumin–artemisinin coamorphous solid: physical properties and pharmacokinetic profile, RSC Advances 102 (2014) 58357–58361.

92. Teja, A.; Musmade, P. B.; Khade, A. B.Dengale, S. J. Simultaneous improvement of solubility and permeability by fabricating binary glassy materials of Talinolol with Naringin: solid state

characterization, in-vivo in-situ evaluation, European Journal of Pharmaceutical Sciences (2015) 234–244.

93. Candolfi, A.; Maesschalck, R. de; Jouan-Rimbaud, D.; Hailey, P. A.Massart, D. L. The influence of data pre-processing in the pattern recognition of excipients near-infrared spectra, Journal of pharmaceutical and biomedical Analysis 1 (1999) 115–132.

94. Gendrin, C.; Roggo, Y.Collet, C. Pharmaceutical applications of vibrational chemical imaging and chemometrics: a review, Journal of pharmaceutical and biomedical Analysis 3 (2008) 533–553.

95. Rinnan, Å.; van den Berg, Frans.Engelsen, S. Balling. Review of the most common pre-processing techniques for near-infrared spectra, TrAC Trends in Analytical Chemistry 10 (2009) 1201–1222.

96. Lavine, B. K.Mirjankar, N. Clustering and classification of analytical data, Encyclopedia of analytical Chemistry (2000).

97. Pearson, K. LIII. On lines and planes of closest fit to systems of points in space, The London, Edinburgh, and Dublin Philosophical Magazine and Journal of Science 11 (1901) 559–572.

98. Kessler, W. Multivariate datenanalyse: für die pharma, bio-und Prozessanalytik. John Wiley & Sons (2007).

99. Eriksson, L.; Johansson, E.; Kettaneh-Wold, N.; Trygg, J.; Wikström, C.Wold, S. Multi-and Megavariate Data Analysis: method extensions and advanced applications. MKS Umetrics AB (2006).

100. Atef, E.; Chauhan, H.; Prasad, D.; Kumari, D.Pidgeon, C. Quantifying Solid-State Mixtures of Crystalline Indomethacin by Raman Spectroscopy Comparison with Thermal Analysis, ISRN Chromatography 1 (2012) 1–6.

101. Broadhead, J.; Edmond Rouan, S. K.Rhodes, C. T. The spray drying of pharmaceuticals, Drug Development and Industrial Pharmacy 11-12 (1992) 1169–1206.

102. Bansal, P.; Hall, M.; Realff, M. J.; Lee, J. H.Bommarius, A. S. Multivariate statistical analysis of X-ray data from cellulose: A new method to determine degree of crystallinity and predict hydrolysis rates, Bioresource Technology 12 (2010) 4461–4471.

103. Chung, F. H. Quantitative interpretation of X-ray diffraction patterns of mixtures. I. Matrix-flushing method for quantitative multicomponent analysis, Journal of Applied Crystallography 6 (1974) 519–525.

104. Kim, Y. Bae; Park, I. Yeong.Lah, W. Ryong. The crystal structure of naproxen sodium,(C14H13O3Na), a non-steroidal antiinflammatory agent, Archives of Pharmacal Research 2 (1990) 166–173.

105. Caliandro, R.; Di Profio, G.Nicolotti, O. Multivariate analysis of quaternary carbamazepine–saccharin mixtures by X-ray diffraction and infrared spectroscopy, Journal of Pharmaceutical and Biomedical Analysis 78-79 (2013) 269–279.

106. Wiklund, S.; Nilsson, D.; Eriksson, L.; Sjöström, M.; Wold, S.Faber, K. A randomization test for PLS component selection, Journal of Chemometrics 10-11 (2007) 427–439.

107. Martens, H. A.Dardenne, P. Validation and verification of regression in small data sets, Chemometrics and Intelligent Laboratory Systems 1–2 (1998) 99–121.

108. Savolainen, M.; Heinz, A.; Strachan, C.; Gordon, K. C.; Yliruusi, J.; Rades, T.Sandler, N. Screening for differences in the amorphous state of indomethacin using multivariate visualization, European Journal of Pharmaceutical Sciences 2 (2007) 113–123.

109. Taylor, L. S.Zografi, G. Spectroscopic characterization of interactions between PVP and indomethacin in amorphous molecular dispersions, Pharmaceutical Research 12 (1997) 1691–1698.

110. Ambike, A. A.; Mahadik, K. R.Paradkar, A. Spray-Dried Amorphous Solid Dispersions of Simvastatin, a Low Tg Drug: In Vitro and in Vivo Evaluations, Pharmaceutical Research 6 (2005) 990–998.

111. Andronis, V.Zografi, G. Crystal nucleation and growth of indomethacin polymorphs from the amorphous state, Journal of non-crystalline Solids 3 (2000) 236–248.

112. Maa, Y.-F.; Nguyen, P.-A.; Andya, J. D.; Dasovich, N.; Sweeney, T. D.; Shire, S. J.Hsu, C. C. Effect of spray drying and subsequent processing conditions on residual moisture content and physical/biochemical stability of protein inhalation powders, Pharmaceutical Research 5 (1998) 768–775.

113. Yoshioka, M.; Hancock, B. C.Zografi, G. Crystallization of indomethacin from the amorphous state below and above its glass transition temperature, Journal of Pharmaceutical Sciences 12 (1994) 1700–1705.

114. Crowley, K. J.Zografi, G. The effect of low concentrations of molecularly dispersed poly (vinylpyrrolidone) on indomethacin crystallization from the amorphous state, Pharmaceutical Research 9 (2003) 1417–1422.

115. Karmwar, P.; Boetker, J.; Graeser, K.; Strachan, C.; Rantanen, J.Rades, T. Investigations on the effect of different cooling rates on the stability of amorphous indomethacin, European Journal of Pharmaceutical Sciences 3 (2011) 341–350.

116. Goldberg, A. H.; Gibaldi, M.Kanig, J. L. Increasing dissolution rates and gastrointestinal absorption of drugs via solid solutions and eutectic mixtures I. Theoretical considerations and discussion of the literature, Journal of Pharmaceutical Sciences 8 (1965) 1145–1148.

117. Moore, M. D.Wildfong, P. L. Aqueous solubility enhancement through engineering of binary solid composites: pharmaceutical applications, Journal of Pharmaceutical Innovation 1 (2009) 36–49.

118. Rastogi, R. P.Bassi, P. S. Mechanism of eutectic crystallization, The Journal of Physical Chemistry 9 (1964) 2398–2406.

119. Singh, N.; Singh, N. B.; Rai, U. S.Singh, O. P. Structure of eutectic melts; binary organic systems, Thermochimica Acta 1 (1985) 291–293.

120. Pearson, J. F.Slifkin, M. A. The infrared spectra of amino acids and dipeptides, Spectrochimica Acta Part A: Molecular Spectroscopy 12 (1972) 2403–2417.

121. Bhise, K. S.; Dhumal, R. S.; Paradkar, A. R.Kadam, S. S. Effect of drying methods on swelling, erosion and drug release from chitosan–naproxen sodium complexes, AAPS PharmSciTech 1 (2008) 1–12.

122. Beyer, A.; Radi, L.; Grohganz, H.; Löbmann, K.; Rades, T.Leopold, C. S. Preparation and recrystallization behavior of spray-dried co-amorphous naproxen–indomethacin, European Journal of Pharmaceutics and Biopharmaceutics (2016) 72–81.

123. Rumondor, A. C.F.Taylor, L. S. Application of Partial Least-Squares (PLS) modeling in quantifying drug crystallinity in amorphous solid dispersions, International Journal of Pharmaceutics 1-2 (2010) 155–160.

Appendix

8.1 **Hazardous materials**

Substance	Supplier	Danger symbol	Hazard statements	Precautionary statements
Naproxen	Fagron		H301	P301, P310
Indomethacin	Fagron		H300	P264-P301, P310
Naproxen-Sodium	Bayer AG		H302-H360	P313
Phosphorus pentoxide			H314	P280-P303, P361, P353-P304, P340, P310-P305, P351, P338

8.2 **Publications**

In the context of this work, the following journal articles with the respective author contributions have been published:

Beyer, A.; Grohganz, H.; Löbmann, K.; Rades, T; Leopold, C. S. Multivariate Quantification of the Solid State Phase Composition of Co-Amorphous Naproxen-Indomethacin, Molecules 10 (2015) 19571–19587. The first author contributed to 95 % to the journal article (project plan, experiments, data analysis, publication; Reference chapters: 7, 5.4).

Beyer, A.; Radi, L.; Grohganz, H.; Löbmann, K.; Rades, T; Leopold, C. S. Preparation and recrystallization behavior of spray-dried co-amorphous naproxen–indomethacin, European Journal of Pharmaceutics and Biopharmaceutics (2016) 72–81. The first author contributed to 80 % to the journal article (project plan, experiments, data analysis, publication; Reference chapters: 7, 5.1).

Beyer, A.; Grohganz, H.; Löbmann, K.; Rades, T; Leopold, C. S. Influence of the cooling rate and the blend ratio on the physical stability of co-amorphous naproxen/indomethacin, European Journal of Pharmaceutics and Biopharmaceutics (2016) 140–148. The first author contributed to 95 % to the journal article (project plan, experiments, data analysis, publication; Reference chapters: 7,5.2).

Beyer, A.; Grohganz, H.; Löbmann, K.; Rades, T.Leopold, C. S. Improvement of the physicochemical properties of Co-amorphous naproxen-indomethacin by naproxen-sodium, International Journal of Pharmaceutics 1 (2017) 88–94.The first author contributed to 95 % to the journal article (project plan, experiments, data analysis, publication; Reference chapters: 7, 5.3).

8.3 **Conference contributions**

In the context of this work, the following conference contributions have been made:

American Association of Pharmaceutical Scientists: Annual Meeting and Exposition
2013: Influence of tableting and storage on the physical stability of a co-amorphous system (Poster presentation)
2014: Preparation of co-amorphous naproxen-indomethacin by cooling the melt using different cooling methods (Poster presentation)
2015: Multivariate quantification of the solid-state phase composition of co-amorphous mixtures (Poster presentation)
Arbeitsgemeinschaft für Pharmazeutische Verfahrenstechnik: World Meeting on Pharmaceutics, Biopharmaceutics and Pharmaceutical Technology
2014: Aging and Molecular Rearrangement in Co-amorphous Indomethacin and Naproxen (Poster presentation)

Pharmaceutical Solid-State Research Cluster: Annual Meeting
2014: Preparation and physical stability of spray-dried co-amorphous Naproxen-Indomethacin (Oral presentation)
2015: Influence of the blend ratio on the physical stability of co-amorphous Naproxen-Indomethacin (Oral presentation)

9 Acknowledgements

I would especially like to thank Prof. Dr. Leopold for leaving me this interesting research topic and for the chance to being a member of her research group. I deeply appreciated the provided scope and freedom to do research and that she always had an open door to discuss scientific approaches and to give guidance.

Furthermore, I am deeply grateful to Prof. Dr. Dr. h.c. Thomas Rades, Dr. Korbinian Löbmann and Dr. Holger Grohganz from the University of Copenhagen for being co-supervisors of my work. I really enjoyed the inspiring discussions with them and their effort for the joint research projects.

Moreover, I thank Prof. Dr. Hans-Ulrich Moritz for evaluating my thesis.

Also, I would like to thank Isabelle Nevoigt form the Institute of Inorganic and Applied Chemistry at the University of Hamburg for her kind help with the X-ray measurements. Petra Borbe and Kai Braunschweig are thanked for their kind assistance with regard to Karl-Fischer and HPLC analysis.

10 Declaration of oath / Eidesstaatliche Versicherung

Hiermit erkläre ich an Eides statt, dass ich die vorliegende Dissertationsschrift selbst verfasst und keine als die angegebenen Quellen und Hilfsmittel benutzt habe. Ich versichere zudem, keinen weiteren Promotionsversuch an einer anderen Einrichtung unternommen zu haben.

Hamburg, den _____

Andreas Beyer